

**Department of Chemical Engineering
Fuels and Energy Technology Institute**

Development of New Fibrous Nanocatalysts for Methane Reforming

Zhitao Wang

**This thesis is presented for the Degree of
Doctor of Philosophy
of
Curtin University**

July 2015

Declaration

To the best of my knowledge and belief this thesis contains no material previously published by any other person except where due acknowledgement has been made.

This thesis contains no material which has been accepted for the award of any other degree or diploma in any university.

Signature:.....

Date:.....

Abstract

The performance of methane reforming heavily depends on catalyst properties. Several types of catalysts have been developed for the catalytic reforming. Nevertheless, each type of catalyst suffers from their own limitations in methane reforming. Fibrous catalysts are a new type of catalysts that combine the advantages of metal gauze/mesh/foam catalysts and traditional supported catalysts. This study aims to investigate the advantages of fibrous catalysts in methane reforming, focusing on the changes in reforming activities with catalyst structure, which is controlled by preparation method and preparation conditions.

A templating synthesis method was used to fabricate NiO/CeO₂ fibrous catalysts using eggshell membrane as a template. This study investigated carbon formation over the catalyst during the dry reforming of methane. The strong catalyst-support interaction formed at high calcination temperatures increased CH₄ conversion and improved coke resistance. The fibrous structure was retained at high calcination temperatures owing to the thermal stability. In addition, fibrous structure enabled the operation at high flow rates without producing substantial pressure drops. Less carbon was formed over the catalyst at high gas flow rates. The preparation parameters were studied. An immersion time of 3 hours formed the most robust structure, and the catalyst calcined at 950 °C produced the highest and most stable methane conversions during the steam reforming of methane.

Electrospinning is another facile method to fabricate fibrous catalysts. It offers great flexibility in tailoring catalyst structure and composition. In this study, the electrospun Ni/Al₂O₃ fibrous catalysts produced high syngas yields during the partial oxidation of methane at the highest recorded gas hourly space velocity owing to fast mass transfer and nanosized catalysts. A further study of the catalyst in dry reforming show the high structural stability of the catalysts because the fibrous structure has a higher resistance to sintering compared with conventional supported catalysts. In summary, fibrous catalysts have thermally stable structure; provide fast mass transfer and nanosized catalyst, resulting in high and stable catalytic performances during methane reforming.

Acknowledgements

I would like to first give my deepest gratitude to my supervisors Professor Chun-Zhu Li and Dr. Dehua Dong. For me, they are the role model of genuine scientists. It is my honor to be their student gaining knowledge and experience from them. Thanks to them for giving me constant support and invaluable guidance. Without each of them, my thesis could not have been completed.

I also would like to express my sincere thanks to all the FETI members: Angelina Rossiter, Tasneem Dawood, John Bromly, Cyril Kelly, Xin Shao, Tingting Li, Shuai Wang, Yao Song, Liping Wu, Lei Zhang, Mortaza Gholizadeh, Yi Cheng, Dr. Yi Wang, Dr. Xun Hu, Dr. Richard Gunawan, Dr. Shu Zhang, Dr. Li Dong, Dr. Kun Zhang, Dr. Kongfa Chen, Dr. Na Ai, Jin Zhang, Chengcheng Wang, for the friendship and their personal and cooperative help and in my PhD study.

I would also like to gratefully acknowledge the financial support for this thesis from the following sources:

- Curtin University of Technology through the Curtin Research Fellowship scheme.
- Australian Research Council Discovery Project (DP120103317).
- The government of Western Australia via the Centre for Research into Energy for Sustainable Transport (CREST).

I also thank Curtin University of Technology for awarding me a Curtin International Postgraduate Research Scholarship.

Finally, I would like to thank my beloved family for their love and encouragement. It is my family who constantly support me and give me motivation on my way following my dream. Without them, it would have been impossible for me to complete my PhD study overseas.

Table of contents

| | |
|---|------------|
| <i>Declaration</i> | <i>I</i> |
| <i>Abstract</i> | <i>II</i> |
| <i>Acknowledgements</i> | <i>III</i> |
| <i>Table of contents</i> | <i>IV</i> |
| <i>List of Tables</i> | <i>X</i> |
| <i>List of Figures</i> | <i>X</i> |
| <i>Chapter 1 Introduction</i> | |
| 1.1 Natural gas and natural gas conversion | 2 |
| 1.1.1 Direct natural gas conversion | 4 |
| 1.1.2 Indirect natural gas conversion | 5 |
| 1.1.2.1 Steam reforming of methane | 5 |
| 1.1.2.2 Dry reforming | 6 |
| 1.1.2.3 Methane partial oxidation..... | 7 |
| 1.2 Catalytic reforming and catalyst structure | 8 |
| 1.2.1 Catalytic reforming | 8 |
| 1.2.2 Catalyst structure..... | 9 |
| 1.2.2.1 Metal gauze/mesh catalysts | 9 |

| | |
|---|-----------|
| 1.2.2.2 Metal foam | 10 |
| 1.2.2.3 Monolith-supported catalyst..... | 11 |
| 1.2.2.4 Powder-supported catalysts | 12 |
| 1.2.2.4.1 Impregnation | 13 |
| 1.2.2.4.2 Precipitation..... | 13 |
| 1.2.2.4.3 Sol-gel | 14 |
| 1.2.2.4.4 Effects of calcination temperature and catalyst content | 16 |
| 1.2.2.4.5 Limitations of powder-supported catalysts in methane reforming..... | 18 |
| 1.3 Significance of this study | 19 |
| 1.4 Scope of thesis..... | 21 |
| 1.5 References | 23 |
| <i>Chapter 2 Experimental methods</i> | |
| 2.1 Catalyst preparation | 37 |
| 2.1.1 Eggshell membrane-templating..... | 37 |
| 2.1.2 Electrospinning..... | 40 |
| 2.2 Catalyst evaluating system | 43 |
| 2.3 Quantification of carbon formed in catalyst..... | 47 |
| 2.4 References | 49 |

Chapter 3 A study on carbon formation over fibrous NiO/CeO₂ nanocatalysts during dry reforming of methane

| | |
|---|-----------|
| 3.1 Introduction | 52 |
| 3.2 Experimental | 53 |
| 3.2.1 Catalyst preparation..... | 53 |
| 3.2.2 Catalyst characterization | 54 |
| 3.2.3 Temperature programmed reduction (TPR) | 54 |
| 3.2.4 Dry reforming test | 54 |
| 3.3 Results and discussion | 55 |
| 3.3.1 The effect of NiO content and crystallization temperature | 55 |
| 3.3.2 The effect of gas flow rate..... | 61 |
| 3.4 Conclusion | 64 |
| 3.5 References | 66 |

Chapter 4 Hierarchically structured NiO/CeO₂ nanocatalysts templated by eggshell membranes for methane steam reforming

| | |
|---------------------------------------|-----------|
| 4.1 Introduction | 70 |
| 4.2 Experimental | 71 |
| 4.2.1 Catalyst preparation..... | 71 |
| 4.2.2 Catalyst characterization | 72 |

| | |
|---|-----------|
| 4.2.3 Steam reforming test | 72 |
| 4.3 Results and discussion | 73 |
| 4.3.1 Hierarchically structured NiO/CeO ₂ nanocatalyst | 73 |
| 4.3.2 The effect of immersion time | 75 |
| 4.3.3 The formation of nanoporous structure | 77 |
| 4.3.4 The effect of catalyst calcination temperature | 78 |
| 4.3.5 The effect of operating temperature and steam/CH ₄ ratio..... | 83 |
| 4.4 Conclusions | 85 |
| 4.5 References | 86 |
| <i>Chapter 5 Nanofibrous Ni/Al₂O₃ catalysts for high yield of syngas production</i> | |
| 5.1 Introduction..... | 90 |
| 5.2 Experimental | 91 |
| 5.2.1 Catalyst preparation..... | 91 |
| 5.2.2 Catalyst characterisation | 92 |
| 5.2.3 Methane reforming test | 93 |
| 5.3 Results and discussions | 94 |
| 5.3.1 Catalyst characterisation | 94 |
| 5.3.1.1 X-ray diffraction (XRD)..... | 94 |

| | |
|---|------------|
| 5.3.1.2 SEM/TEM | 97 |
| 5.3.1.3 Temperature programmed reduction | 100 |
| 5.3.2 Catalytic methane partial oxidation..... | 102 |
| 5.3.2.1 Effect of NiO content | 102 |
| 5.3.2.2 Syngas yield comparison..... | 104 |
| 5.3.2.3 Catalyst structural stability | 107 |
| 5.4 Conclusions | 108 |
| 5.5 References | 110 |
| <i>Chapter 6 Effects of calcination temperature of electrospun fibrous Ni/Al₂O₃ catalysts on the dry reforming of methane</i> | |
| 6.1 Introduction..... | 115 |
| 6.2 Experimental | 116 |
| 6.2.1 Catalyst preparation..... | 116 |
| 6.2.2 Catalyst characterisation | 117 |
| 6.2.3 Catalytic reforming test..... | 117 |
| 6.3 Results and discussions | 118 |
| 6.3.1 Catalyst crystallinity..... | 118 |
| 6.3.2 Catalyst reducibility | 119 |
| 6.3.3 Catalyst microstructure | 120 |

| | |
|---|----------------|
| 6.3.4 Catalytic performances..... | 123 |
| 6.4 Conclusions | 125 |
| 6.5 References | 126 |
| <i>Chapter 7 Conclusions and recommendations</i> | |
| 7.1 Conclusions | 130 |
| 7.2 Recommendations | 132 |
| <i>Appendix I Permission of Reproduction from the Copyright Owner</i> | <i>134</i> |

List of Tables

Chapter 1

| | |
|---|----|
| Table 1-1. The composition of natural gas..... | 2 |
| Table 1-2. The comparison of the catalyst preparation methods | 16 |

Chapter 5

| | |
|--|-----|
| Table 5-1. Peak areas from the TPR profiles | 102 |
| Table 5-2. Comparison of syngas yield by the nanofibrous catalyst and conventional supported catalysts. | 105 |

List of Figures

Chapter 1

| | |
|--|----|
| Figure 1-1. Routes for the transformation of methane into value-added products. | 3 |
| Figure 1-2. The preparation of monolith-supported catalysts via wash coat. | 11 |
| Figure 1-3. Gas diffusion over powder-supported catalysts. | 18 |

Chapter 2

| | |
|---|----|
| Figure 2-1. Schematic representation of the one-step template synthesis of fibrous NiO/CeO ₂ catalysts for the CPOM at microsecond contact times. | 38 |
| Figure 2-2. A schematic diagram of the templating synthesis process. | 39 |

| | |
|--|-----------|
| Figure 2-3. A schematic diagram of a basic electrospinning setup..... | 41 |
| Figure 2-4. NABOND-NEU electrospinning setup. | 42 |
| Figure 2-5. A schematic diagram of the catalyst testing system..... | 44 |
| Figure 2-6. A schematic diagram of the arrangement of catalyst flakes in reactor. .. | 45 |
| Figure 2-7. Counter-current flow in the reactor for steam methane mixing. | 46 |
| Figure 2-8. The schematic diagram of the carbon burning reactor. | 48 |

Chapter 3

| | |
|---|-----------|
| Figure 3-1. XRD patterns of the NiO/CeO ₂ catalysts with the NiO contents of (a) 12.9 wt%; (b) 27.7 wt% and (c) 47.8 wt% at a crystallization temperature of 1000 °C and (d) 47.8 wt% at a crystallization temperature of 1100 °C. | 56 |
| Figure 3-2. SEM images of the NiO/CeO ₂ catalysts with the NiO contents of (a) 12.9 wt%; (b) 27.7 wt% and (c) 47.8 wt% at the crystallization temperature of 1000 °C and (d) 47.8 wt% at the crystallization temperature of 1100 °C. The scale bar is 1 μm. | 57 |
| Figure 3-3. TPR profiles of the NiO/CeO ₂ catalysts with the NiO contents of (a) 12.9 wt%; (b) 27.7 wt% and (c) 47.8 wt% at a crystallization temperature of 1000 °C and (d) 47.8 wt% at a crystallization temperature of 1100 °C... | 59 |
| Figure 3-4. CH ₄ conversion decay during dry reforming for 10 h over the NiO/CeO ₂ catalysts with different NiO contents at different crystallization temperatures. | 60 |
| Figure 3-5. The effect of NiO content and crystallization temperature of the NiO/CeO ₂ catalysts on carbon formation rate..... | 61 |

| | |
|--|-----------|
| Figure 3-6. The effect of gas flow rate on carbon formation rate over the 47.8 wt% NiO/CeO ₂ catalyst..... | 62 |
| Figure 3-7. SEM images of the 47.8 wt% NiO/CeO ₂ catalysts after dry reforming at different GHSVs: a, 2.7×10 ⁵ h ⁻¹ ; b, 2.1×10 ⁶ h ⁻¹ ; c, 4.1×10 ⁶ h ⁻¹ and d, 1.1×10 ⁷ h ⁻¹ . The scale bar is 1 μm..... | 63 |
| Figure 3-8. SEM image of Ni particle at the tip of carbon nanofiber after dry reforming. The scale bar is 200 nm..... | 63 |
| Figure 3-9. Reaction rate change with time on stream during dry reforming over the 47.8 wt% NiO/CeO ₂ catalyst for 10 h at different GHSVs..... | 64 |

Chapter 4

| | |
|---|-----------|
| Figure 4-1. SEM images of template and the hierarchical structure of templated nanocatalyst: ESM template (a), ESM-templated NiO/CeO ₂ nanocatalyst (b) and nanoporous catalyst fibre (c). | 74 |
| Figure 4-2. Comparison of NiO/CeO ₂ nanocatalysts prepared with different immersion times: a, 1 h; b, 3 h; c, 5 h; d, 9h. Scale bar is 1 μm. | 76 |
| Figure 4-3. TGA profiles of the ESM-metal composites prepared at different immersion times. | 76 |
| Figure 4-4. SEM images of the cross sections of the ceramic fibres calcined at different temperatures: a, 500; b, 700; c, 800 and d, 900 °C. Scale bar is 200 nm..... | 78 |
| Figure 4-5. SEM images of the catalysts calcined at different temperatures: a, 900 °C; b, 950 °C; c, 1000 °C and d, 1050 °C. Scale bar is 200 nm. | 79 |
| Figure 4-6. XRD patterns of the catalysts calcined at different temperatures. | 79 |

| | |
|--|-----------|
| Figure 4-7. TPR profiles (a) and the corresponding H ₂ consumption (b) of the catalysts calcined at different temperatures. | 81 |
| Figure 4-8. CH ₄ conversion in steam reforming at 800 °C within 300 min over the catalysts calcined at different temperatures. | 82 |
| Figure 4-9. SEM images of the tested catalysts calcined at different temperatures: a, 900 °C; b, 950 °C; c, 1000 °C and d, 1050 °C. Scale bar is 2 μm. | 83 |
| Figure 4-10. CH ₄ conversion and H ₂ /CO ratio as functions of operating temperature and steam/CH ₄ ratio during steam reforming over the catalyst calcined at 950 °C. | 84 |

Chapter 5

| | |
|--|-----------|
| Figure 5-1. Comparison of mass transfers over the catalysts with different microstructures. | 90 |
| Figure 5-2. XRD patterns of the catalysts before (A) and after (B) reduction with different Ni contents: a, a'-7.4 wt%; b, b'-13.7 wt%; c, c'-19.2 wt%; d, d'-24.1 wt%; e, e'-28.4 wt%; f, f'-32.3 wt%. | 95 |
| Figure 5-3. STEM-EDS elemental mapping of 19.2 wt% (a), 24.1 wt% (b), 28.4 wt% (c) and 32.3 wt% (d) Ni/Al ₂ O ₃ catalyst before reduction. | 96 |
| Figure 5-4. SEM images of an as-prepared Ni/ Al ₂ O ₃ catalyst calcined at 1000 °C (a) and a cross section of the catalyst flakes (b). | 97 |
| Figure 5-5. SEM images of the reduced catalysts with different Ni contents: a-7.4 wt%, b-13.7 wt%, c-19.2 wt% d-24.1 wt%, e-28.4 wt%, f-32.3 wt%. Scale bars are 200 nm. | 98 |
| Figure 5-6. STEM images of 24.1wt% (a), 28.4 wt% (b) and 32.3 wt% (c) Ni/Al ₂ O ₃ catalyst after reduction. Scale bars are 100 nm. | 99 |

| | |
|--|------------|
| Figure 5-7. STEM-EDS elemental mapping of 24.1 wt% (a), 28.4 wt% (b) and 32.3 wt% (c) Ni/Al ₂ O ₃ catalyst after reduction..... | 100 |
| Figure 5-8. TPR profiles of the catalysts with different Ni contents. | 101 |
| Figure 5-9. Effect of catalyst content on methane conversion at a GHSV of 8×10 ⁶ LKg ⁻¹ h ⁻¹ (a) and the effect of GHSV on methane conversion at the Ni contents of 19.2 wt% and 24.1 wt% at 850 °C (b). | 103 |
| Figure 5-10. Selectivity of syngas produced by 24.1 wt% Ni/Al ₂ O ₃ catalyst..... | 106 |
| Figure 5-11. CH ₄ conversion and syngas selectivity produced by the 13.7wt% Ni/Al ₂ O ₃ catalyst at different operation temperatures. | 106 |
| Figure 5-12. Stability test of 24.1 wt% Ni/Al ₂ O ₃ catalyst during methane partial oxidation over 10 hours at a GHSV of 4×10 ⁶ LKg ⁻¹ h ⁻¹ | 107 |
| Figure 5-13. SEM image of the 24.1 wt% Ni/Al ₂ O ₃ catalyst after methane partial oxidation for 10 hours. | 108 |
| Figure 5-14. TEM image (a, b) and EDS elemental mapping (c) of the 24.1 wt% Ni/Al ₂ O ₃ catalyst after methane partial oxidation for 10 hours. | 108 |

Chapter 6

| | |
|--|------------|
| Figure 6-1. XRD patterns of the Ni/Al ₂ O ₃ catalysts before (A) and after (B) reduction at 750 °C for 1 hour at different calcination temperatures: a, a'- 700 °C; b, b'- 800 °C; c, c'- 900 °C; d, d'- 1000 °C. | 118 |
| Figure 6-2. TPR profiles of the catalysts calcined at different calcination temperatures. | 120 |
| Figure 6-3. A SEM image of the NiAl ₂ O ₄ /Al ₂ O ₃ ceramic fibres calcined at 900 °C. The scale bar is 2 μm. | 121 |

Figure 6-4. SEM images of the catalysts at different calcination/reduction temperatures: a, 700 °C/750 °C; b, 800 °C/750 °C; c, 900 °C/750 °C; d, 1000 °C/750°C; a', 700 °C/850°C; b', 800 °C/850°C; c', 900 °C/850 °C; d', 1000 °C/850 °C; a'', 700 °C/920 °C; b'', 800 °C/920 °C; c'', 900 °C/920°C; d'', 1000 °C/920°C. Scale bars are 200 nm. **122**

Figure 6-5. Catalytic performances of the dry reforming of methane at 500 °C over the catalysts at different calcination temperature/reduction temperatures: a, 700 °C/750 °C; b, 800 °C/800 °C; c, 900 °C/850 °C; d, 1000 °C/920 °C; e, 1000 °C/750 °C. **124**

Figure 6-6. SEM images of the catalyst calcined at 1000 °C and reduced at 920 °C before (a) and after (b) reaction. **124**

Chapter 1

Introduction

1.1 Natural gas and natural gas conversion

Being known initially as the by-product of crude oil production, natural gas is playing an indispensable role in the worldwide energy supply matrix. The International Energy Agency outlook 2014 reported that natural gas accounted for nearly a quart of the world energy consumption [1]. The worldwide energy demand for natural gas is expected to keep increasing, and natural gas will overtake coal to be the second most important energy source by 2040.

Natural gas is a mixture of mainly hydrocarbon gases, with methane amounting up to 90% as the predominant component [2, 3]. Other hydrocarbons, like ethane and propane, as well as a small amount of inorganic gases are also present in natural gas. [4, 5] The composition of natural gas varies with reserves and fields. A typical composition of natural gas [3] is listed in Table 1-1.

Table 1-1. The composition of natural gas. (Redrawn based on Ref.3)

| Gas component | Concentration range, vol% |
|---|---------------------------|
| Methane | 70-90 |
| Ethane | 0-20 |
| Propane | |
| Butane | |
| Pentane and higher hydrocarbons | 0-10 |
| Carbon dioxide | 0-8 |
| Oxygen | 0-0.2 |
| Nitrogen | 0-5 |
| Hydrogen sulfide, carbonyl sulfide | 0-5 |
| Rare gas: argon, helium, neon, | Trace |

There are abundant natural gas reserves globally, which were confirmed to be double that of oil and forecasted to outlast oil by 60 years [6-8]. As oil reserves diminish and its price increases, natural gas will be increasingly important in the future energy matrix [9]. Nevertheless, certain portion of the proven reserves (around 40%) are found in rural areas, which are far away from final markets or users [6, 8, 10-12].

Thus, a delivery system is required to transport natural gas to the final markets. In order to deliver natural gas, many means have been developed, and the pipeline delivery is very popular. Nevertheless, the transportation of natural gas by pipelines is efficient only for short distances in most cases [8, 13].

To achieve effective transportation and/or gain economic benefits, natural gas should preferably be converted into liquid fuels or valuable products. Some examples of the natural gas conversion are shown in Figure 1-1.

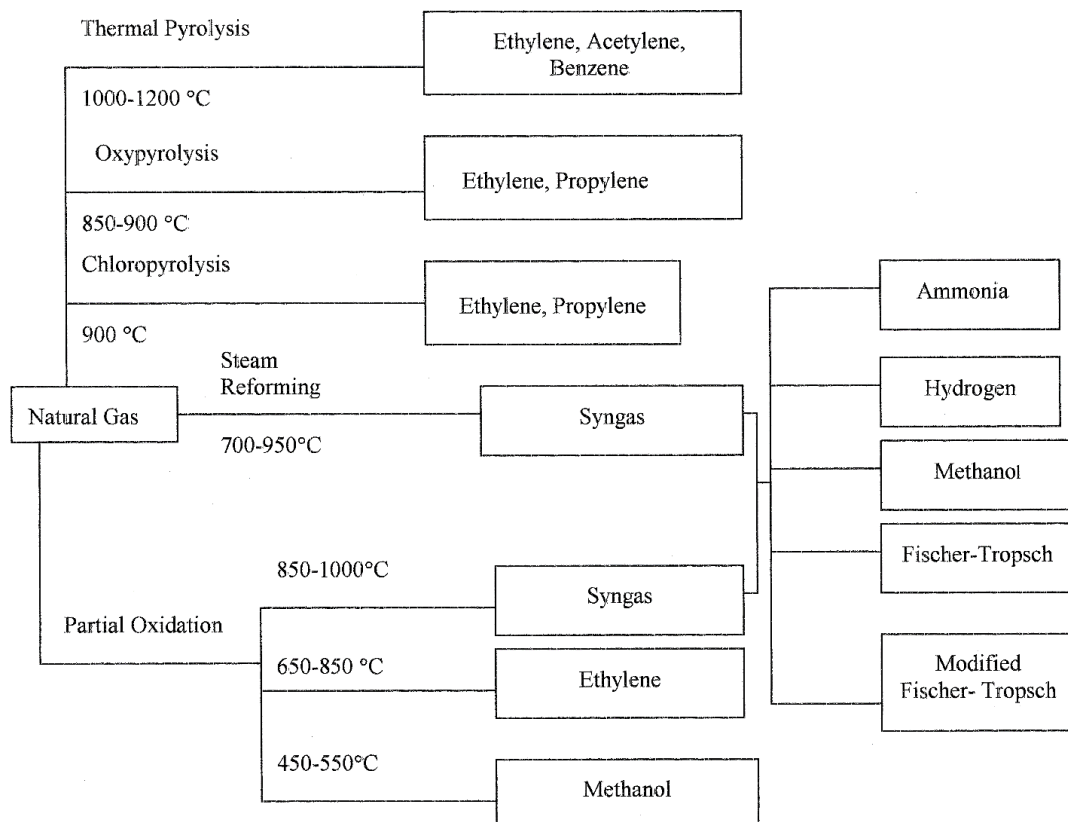


Figure 1-1. Routes for the transformation of methane into value-added products [5]. (Reprinted with permission from Elsevier)

Two paths of the natural gas conversion were developed: the first one is the direct conversion of methane, where methane is pyrolysed or reacts with an oxidant to produce more useful products; the other path is indirect path, which produces syngas ($\text{CO} + \text{H}_2$) as an intermediate through methane reforming. Then, the syngas is converted to liquid fuels or valuable products [8, 14].

1.1.1 Direct natural gas conversion

The direct conversion of natural gas refers to converting methane to products in one step, and the paths of the conversion are listed below:

1. Thermal pyrolysis:



2. Oxidative coupling:



3. Partial oxidation:



4. Oxidative chlorination:



The direct path eliminates the expensive step of syngas production, which accounts for 60% or more of the total cost of the indirect path [6, 15, 16]. However, the practical utilization of those direct paths for bulk chemical production is limited [2]. It is because the direct path has achieved so far low yields [17]. Methane is quite stable, and high temperature is required to activate the structurally symmetrical molecule. Once it is activated to form radicals, gas phase radical reactions would dominate [12, 15, 18]. It is because the products are much more reactive than methane, which thermodynamically favors the further reaction into C or CO₂ [19]. Therefore, the attempts to achieve high methane conversions will lead to low product selectivity. The inherent limits of the production yields have been calculated by

many researchers. For example, the upper limit of the C2 (C₂H₄ and C₂H₆) yield via the oxidative coupling of methane at atmospheric pressure and the O₂/CH₄ molar ratio of 0.5 would be less than 30% [15, 20]; the limits of methanol and formaldehyde yields via the direct oxidation would be 8% and 4%, respectively [4]. The limitation makes the direct path less economically attractive and competitive compared with the indirect path.

1.1.2 Indirect natural gas conversion

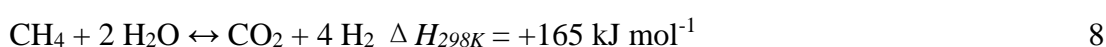
The first step in the indirect natural gas conversion is the production of syngas via methane reforming with an oxidant. Then, syngas is converted into liquid fuels or chemicals via the Fischer-Tropsch (F-T) process, like ammonia, methanol and dimethyl ether (DME) [21-23]. As the direct path is limited by low yields, the indirect path through the production of syngas is more viable although methane reforming is cost-intensive.

The production of syngas via methane reforming has been widely studied, and various processes have been developed. Three representative methane reforming paths have been used to produce syngas with different H₂ to CO ratios: steam reforming [24-26], dry reforming [27] and partial oxidation [28].

1.1.2.1 Steam reforming of methane

The steam reforming of methane/steam-methane reforming (SMR) is the main process for hydrogen production, accounting for more than 50% of world's H₂ production [16, 29-31].

The production of syngas via SMR involves three reactions occurring simultaneously:



Reactions 7 and 8 are highly endothermic, which makes the processes energy-intensive. For practical operations, the energy required to carry out the reactions is normally supplied via burning natural gas. Due to the water-gas-shift reaction (Reaction 9), a certain amount of CO₂ is present in the product, which is unfavorable for the downstream processes. Hence, a separation process is required [29]. In order to achieve high CH₄ conversions and limit CO₂ formation, SMR is carried out at elevated temperatures, normally above 700°C. Furthermore, an extra amount of steam is usually fed into the reactor to facilitate CH₄ conversion and suppress carbon formation over the catalysts. These eventually increase the total energy input drastically [29].

Among those three reforming paths (steam reforming, dry reforming and partial oxidation), steam reforming gives syngas with the highest H₂/CO ratio of about 3, which is good for the fuel cell application and H₂ production. In the industrial hydrogen production, the gas mixture of CO₂, CO and H₂ would go through two consecutive shift reactions (high temperature shift and low temperature shift reactions) to minimize the concentration of CO and maximize hydrogen yields. The concentration of CO after those shift reactions could be as low as 0.1% [32].

1.1.2.2 Dry reforming

The dry reforming of methane (DRM) using CO₂ as an oxidant is a promising method for not only syngas production, but also environmental protection as it consumes two major greenhouse gases [12, 33]. The reaction of the dry reforming of methane is shown below [31, 34]:



Like the SMR, dry reforming is energy-intensive as it is an endothermic reaction. Reacting with CO₂, CH₄ gives syngas product with a H₂/CO ratio of about 1 [9, 26]. The H₂/CO ratio is suitable for the production of chemicals such as dimethyl ether, acetic acid and formaldehyde [11, 18]. Ha et al. has demonstrated the production of hydrocarbons by coupling the dry reforming of methane with the Fischer-Tropsch process [35].

Due to the massive use of fossil fuels, CO₂ emission keeps increasing, which causes serious environmental problems and challenges to industry. Numerous attention has been given to seeking new technologies to reduce the greenhouse gas emission or recruit CO₂ back into the energy transmission system [33]. Dry reforming of methane is thus promising as it draws the CO₂ back into energy matrix. Moreover, there are research interests emerging on the replacement of the heat supply via burning natural gas, which releases a large amount of CO₂, with the renewable energy such as solar and nuclear energies [12, 36]. Worner et al. [37] had demonstrated the dry reforming of methane in a solar driven volumetric receiver-reactor. This concept could not only cut the CO₂ emission, but also realize the energy harvesting and transportation.

Since the first demonstration of the dry reforming of hydrocarbons with CO₂, the technology has been widely used. Nevertheless, the industrial utilization of the dry reforming is still limited [2, 31]. The main obstacle is that carbon formation readily occurs during the reforming, mainly from methane cracking and CO disproportionation [29, 38, 39] :



Although noble metal catalysts show high resistance to coking, the limited reserves and the difficulty in dealing with those spent catalysts limit its wide applications. Alternatively, Ni-based catalysts show comparable performance to noble catalysts, but carbon formation is favored [8, 16]. As a result of carbon formation, the catalysts could be easily destroyed or even block the reactor, causing safety issue. How to develop stable catalysts with high coke resistance is the bottleneck for the application of DRM.

1.1.2.3 Methane partial oxidation

Considering the energy efficiency, the partial oxidation of methane is more attractive than those endothermic steam reforming and dry reforming, as it is very exothermic. The two main reactions that occur during the partial oxidation are [4]:



The partial oxidation of methane gives syngas with a H₂/CO ratio of 2, which is suitable for the methanol production via the Fischer-Tropsch process. As the partial oxidation of methane is exothermic, heat is released during the reaction. In order to utilize those heat, the partial oxidation of methane could be performed concurrently with the endothermic steam/dry reforming [23]. With a proper control of the ratio of CH₄, O₂ and H₂O, autothermal reforming can be achieved.

The partial oxidation of methane is kinetically fast and can complete within milliseconds or microseconds [23, 40]. An intrinsic problem of a fast and exothermic reaction is the formation of hot spots in the catalysts bed [31, 41]. The formation of hot spots could readily deactivate catalysts via the sintering of the active phase or collapsing catalyst structure. Therefore, highly thermally stable or the properly structured catalyst with good heat transfer is highly demanded. Another disadvantage of the partial oxidation of methane is that pure oxygen is required, which greatly increase the production cost as oxygen is produced by an expensive cryogenic process or pressure-swing adsorption [42, 43].

1.2 Catalytic reforming and catalyst structure

1.2.1 Catalytic reforming

Methane reforming reactions normally occur in the presence of a catalyst to achieve high conversion and selectivity to desirable products at low reforming temperatures, called catalytic reforming. For example, the methane partial oxidation needs to be operated at 1200 to 1500 °C to achieve high conversions [16]. With the activation by catalysts, the reforming temperature can be reduced to 850 °C. Over the most studied porous catalysts, the catalytic reforming includes several steps:

- 1). Reactant gases diffuse from gas flow to the surface of the catalysts support, and then diffuse into the interior of pores to reach the catalysts;

- 2). Methane and oxidant (H_2O , CO_2 or O_2) are activated on catalyst surface, forming radicals such as $\text{CH}_3\cdot$ and $\text{O}\cdot$;
- 3). Radicals react to form products;
- 4). Products diffuse from catalyst surface towards outside of the pore, and then diffuse to gas flow.

Therefore, the catalytic sites are important for achieving high catalytic activity and determined by catalyst surface/particle size. Additionally, gas diffusion between catalyst surface and gas flow greatly affects the overall reaction rate, and catalyst structure determines the mass transfers.

1.2.2 Catalyst structure

1.2.2.1 Metal gauze/mesh catalysts

Metal gauze/mesh catalysts are made from metal wires through different methods (woven or knitted) [44]. The stacked metal gauze catalysts have been used for the production of nitric acid via ammonia and hydrogen cyanide via the Andrussow process [45-48].

Metal gauze catalysts are normally characterized as showing low pressure drops at high space velocities [47, 49, 50], which are attractive for the reactions that require high space velocities to achieve a high selectivity for the desired products. For example, the catalytic partial oxidation (CPO) of alkanes over metal gauze catalysts (made of Pt and its alloy with Rh) were the mostly used in researches. The residence time for the CPO is in the millisecond range (1-50 ms) [40]. Long residence time sacrifices the syngas selectivity. Pt-10%Rh gauze for the catalytic partial oxidation was studied by Hickman et al. [51], and syngas selectivity of about 90% was achieved with short space time (0.00021-0.00042s) at the CH_4/O_2 ratio of 2. Other than precious metal gauze catalyst, transition metal catalysts, like Ni mesh, were also adopted for methane reforming [52, 53].

A high surface area of metal catalysts is sought for most of the catalytic processes. However, the surface area of the self-supported metal gauze/mesh catalyst is extremely low compared with supported catalysts [54]. It results in low catalytic activity when applying non-precious metal gauze. Monnerat et al. studied the catalytic cracking of methane over a nickel gauze [49]. In order to increase the surface area, a layer of Raney Ni was firstly formed on the surface of Ni gauze, and then the aluminum was removed to increase surface area. Nevertheless, the resulted surface area of about 26.7 m²/g was still below that of supported catalysts.

1.2.2.2 Metal foam

Another type of metal catalyst is the “open-cell” foam. Typically, the three-dimensional (3D) cellular structure of the foam is constructed by three connecting components: metallic framework (strut), spherical cells and open windows [55, 56]. Metal combining with the cellular structure gives groups of properties such as good electrical and thermal conductivity, ductility/malleability, low volume density, high strength to weight ratio, and high surface area to volume ratio (on the order of 10000 m²/m³) [57-61]. The foams are used in various processes such as filtration, VOC abatement and heat exchange [62-64].

Considering the 3-D structure, metallic foam could be an excellent catalyst/support for the heterogeneous catalysis. Firstly, the high porosity, up to 97%, can greatly reduce the pressure drop at high space velocities, enabling the occurrence of those kinetically fast reactions at short contact times to maximize the yields of valuable intermediates and achieve high throughputs [56, 65]. Secondly, the distorted flow path through those cells gives rise to the turbulence, which improves mass transfer via enhancing the convective transfer [66-68]. The transport phenomena during the catalytic partial oxidation of methane over Rh and Pt foam catalysts were studied by Horn et al. [69], demonstrating that the metal foam is beneficial to form a uniform temperature profile along the catalysts bed and eliminate the formation of hot and cool spots. Coleman et al. studied the catalytic partial oxidation of methane over a nickel foam [70]. Methane conversion, H₂ and CO selectivity achieved 89%, 96% and 97% at 850°C, respectively, which are comparable with that of the supported Ni/γ-Al₂O₃ catalyst. Other applications of foam catalysts or metallic foam supported

catalysts in methane steam/dry reforming were also reported in the literature [58, 71-75].

Like metal gauze/mesh catalysts, the low surface areas of metallic foams ($< 0.1 \text{ m}^2/\text{g}$) restrains its applications [70]. Various methods have been developed to increase the surface area of metallic foam, for instance wash-coat and impregnation [76, 77]. However, it is not effective due to the poor adhesion of the wash-coat to metallic surface. Although some methods have been developed, it is still challenging to form a highly porous layer on the surface of metal foams.

1.2.2.3 Monolith-supported catalyst

Monolith-supported catalysts are normally referred as a thin layer of catalysts deposited on the internal channel surface of monolith substrate, either ceramic or metallic [78]. The built-in channels could be straight, crimped or wavy with the different shapes of cross-section, such as round, square or polygon [65].

Monolith itself is not a good candidate for the catalyst support due to low surface areas, normally less than $4 \text{ m}^2/\text{g}$, which restrains catalyst loading and dispersion [66, 79]. In order to increase the internal surface area, many methods have been developed, and preparing wash coat is widely used due to its simplicity [78]. By depositing a porous layer such as γ -alumina on the surface, the wash coat can significantly increase surface area to be several orders of magnitude higher than bare monoliths [80]. The schematic diagram of the preparing monolith-supported catalysts via wash coat is shown in Figure 1-2 [81].

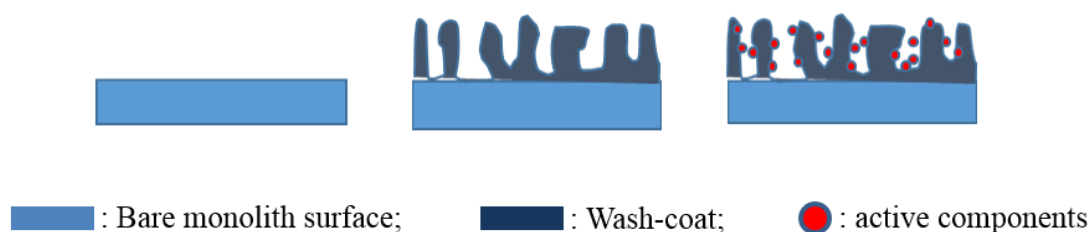


Figure 1-2. The preparation of monolith-supported catalysts via wash coat. (Redrawn based on Ref. 82)

The monolith catalysts have been used in the environmental related processes, such as the three-way catalyst for automobile emission control [48, 78, 82, 83]. The monolith catalysts have several properties that are superior to powder-supported catalysts, which are packed into a catalyst bed in reactors. The first one is low pressure drop [78, 79, 84]. The pressure drop in the monolith has been observed to be two to three orders of magnitude smaller than that in fixed beds filled with randomly packed catalyst pellets [83, 85, 86]. Secondly, monolith catalysts show low internal diffusion resistances [79, 87]. The thickness of wash coat is normally less than 100 μm [84]. Hence, the resistance of the internal diffusion within wash coat is small compared with that of granular catalysts with particle size more than 1 mm.

However, the practical applications of monolith catalysts in non-environmental processes are rather limited. One of the reasons is its high cost. The manufacture of monolith substrates and the preparation process of the catalysts are expensive [79, 86]. Another shortcoming of the monolith catalysts is the low utilization efficiency of reactor volume because the majority of reactor volume is occupied by monoliths [68, 82].

1.2.2.4 Powder-supported catalysts

Powder-supported metal catalysts are widely used in industries and laboratory researches. Catalyst particles are supported on ceramic powders, and ceramic powders provide a large surface area of $> 200 \text{ m}^2/\text{g}$ for supporting catalyst particles to achieve high catalyst dispersion [88]. Catalyst catalytic performances are determined by both catalysts and supports. The properties of catalysts and supports depend on preparation methods.

The preparation of powder-supported catalyst processes can be classified into two categories: one is impregnation: catalysts and supports are prepared separately. The other one is called one-pot synthesis. Catalysts and supports are prepared by one process, such as precipitation and sol-gel process.

1.2.2.4.1 Impregnation

Impregnation is the most used method for the preparation of powder-supported catalysts with a pre-shaped/structured support due to its simplicity [89]. The impregnation procedure could be realized via a sequence of steps: dissolving catalyst precursors (e.g. salts) in a solvent; depositing physically or chemically catalyst precursor on the support via the contact of the metal containing precursor solution with supports; removing solvent by drying; converting catalyst precursors into catalysts by heat treatment and sometimes reduction [81].

Catalyst distribution profile indicates catalyst efficiency. With a certain catalyst loading, a uniform distribution of catalysts throughout the carrier body could give small particle size and high dispersion and therefore high catalytic performance. However, it is still a challenge to achieve uniform catalyst distribution. There are two reasons that can cause the non-uniform distribution of catalysts: some small pores are inaccessible for catalyst solution due to trapped air. Vacuuming can improve the impregnation process [81]. The other reason is relocating catalyst precursors caused by drying as solvent evaporation starts from surface to inside. During drying process, catalyst precursors concentrate in the remained solvent, which leads to the inhomogeneous distribution of catalysts.

Limited by the solubility of metal precursor, the catalyst loading of the impregnated catalysts is generally below 10% [89]. To achieve higher catalyst loadings, the repeated impregnation process is required. The impregnation process is also used for the preparation of monolith catalysts via infiltrating the catalyst precursor solution in the pores of wash-coat layer [79]. In this case, catalyst loading is also limited by the thin wash-coat layer, and the repeated impregnation can cause catalyst aggregation.

1.2.2.4.2 Precipitation

Precipitation is the crystallization of hydroxide or carbonate from a catalyst precursor solution. The precipitation process starts with the formation of a super-saturation condition via a physical/chemical process such as solvent evaporation and pH

variation [90], and then separating the precipitates from the solution, followed by converting catalyst precursors to catalysts via heat treatment.

By having the precursors of support and metal catalyst in one solution, precipitation is an effective method to prepare supported catalysts in one step (known as co-precipitation). This is normally carried out by mixing support and catalyst precursors, and the precursors precipitate from the solution by adding a precipitating agent such as ammonia. Catalysts of high surface area can be obtained during the decomposition of catalyst precursors such as hydroxides. Moreover, as catalyst and support precursors are well-dispersed in solution, the catalyst prepared via precipitation showed very high dispersion and small particle size. Liu et al. compared the silica supported Ag catalysts prepared by impregnation and precipitation [91]. Much smaller particles were produced from precipitation. The particle size produced by precipitation and impregnation were 3.5 and 15-18 nm, respectively.

Compared with the impregnated catalysts, the catalysts prepared by precipitation show flexibly controlled catalyst loadings/contents via simply adjusting the composition of catalyst precursor solution. However, catalyst particles aggregate as catalyst content increases, which reduces catalyst efficiency. Seo et al. studied the effect of Ni content on the performance of a Ni-Al₂O₃ catalyst [92], and found that the catalytic performance in steam reforming increased with increasing Ni content up to 50%. Further increasing Ni content did not improve catalytic performance. The main problem with precipitated catalysts is that the catalysts readily aggregate during drying, calcination and reaction. Small and fresh particle sizes formed during precipitation can grow into agglomerates during subsequent heat treatments. In addition, a certain amount of catalyst precursors are left in solution, reducing catalyst utilization efficiency [81].

1.2.2.4.3 Sol-gel

Sol-gel process utilizes the transformation of catalyst precursor solution by adding an agent. The agent interacts with metal ions to avoid the segregation of catalyst precursors from solution during the subsequent solvent evaporation. As the solvent is evaporated, the precursor is turned into gel, and the gel finally becomes a foam with

large pore volume formed by solvent evaporation. Then, the catalyst foam precursor is converted into catalyst powder during calcination. A large amount of gases are released due to the burning off of organic agents, which is beneficial for forming catalyst powders with high surface areas. Crisan and coworkers successfully synthesized sol-gel based Al_2O_3 and $\text{Ni}/\text{Al}_2\text{O}_3$ with surface areas of 207.4 and 321.2 m^2/g , respectively [93]. High surface area of 800 m^2/g of so-gel-derived material was also reported [94].

Like precipitation process, sol-gel process can produce catalysts with high dispersion and loading/content. However, during the calcination of catalyst precursor, combustion occurs because a certain amount of organic agent is employed and the decomposition of catalyst precursors produces heat. The combustion incurs the temperature differences, resulting in inhomogeneous particle sizes, even severe aggregation [95]. The use of organic agent also increases preparation cost.

A comparison regarding catalysts synthesis, advantages, disadvantages and stability of various methodologies mentioned above is shown in table 1-2.

Table 1-2. The comparison of the catalyst preparation methods

| Methods | Synthesis | Advantages | Disadvantages | Stability |
|---------------|--|---|--|-----------------------------------|
| Sol-gel | A third agent to prevent the segregation; one-pot synthesis | High surface area; high dispersion at low catalyst loadings, | Temperatures, mass transfer limitation; inhomogeneous particle sizes | Easy aggregation at high loadings |
| Impregnation | Simple, easy operation; repeated impregnation might be required | Controllable distribution of catalyst over pre-shaped support; fast mass transfer | Limited catalyst loading; large support volume | Easy aggregation |
| Precipitation | Catalysts precept form solution via changing temperature /pH; requires good control of temperature or pH | High dispersion and small particle size | Temperatures; mass transfer limitation | Easy aggregation at high loadings |

1.2.2.4.4 Effects of calcination temperature and catalyst content

Different preparation methods have different parameters affecting catalyst properties [96]. However, there are two parameters that are applicable for all methods and heavily determine catalyst performances. The first one is calcination temperature [97]. Calcination is normally the final step in catalyst preparation (the activation of catalysts by reduction is normally carried out in situ in reactors). The catalyst properties, especially catalyst particle size, are strongly related to calcination temperature [98, 99]. Although low calcination temperatures are preferred to form catalysts with small particle sizes, catalytic reaction at high temperatures, like methane reforming (600-850 °C), will cause further sintering during reactions. Catalyst particle sintering reduces catalyst active surface; catalyst support sintering causes pore structure collapse and wrap catalyst particles in agglomerations. As a result, some catalyst particles are inaccessible to reactant gases.

Moreover, high calcination temperatures could form the strong interaction between catalysts and supports, which is also an important property of catalysts. It was

reported that high calcination temperature of Ni/MgAl₂O₄ catalyst improved catalytic activity and stability for the catalytic partial oxidation of methane [100]. It is because the strong interaction formed after high temperature calcination maintained Ni dispersion after reduction. Guo et al. also found that a strong interaction between Ni and the support Mg₂AlO₄ was beneficial for high performance and resistance to carbon formation in the dry reforming of methane [101]. Roh et al. reported the positive effect of the strong metal-support interaction on the catalytic performance of a Ni/Ce-ZrO₂ catalyst in methane steam reforming [102]. However, some opposite conclusions have been drawn because the catalyst structure shows low thermal stability and the surface area of catalyst greatly decreased with increasing calcination temperature [99, 103]. Therefore, calcination temperature greatly affects catalyst performances while the effects depend on catalyst structure, materials and preparation method.

The other important parameter affecting catalyst properties is catalyst loading/content. Catalyst content can be flexibly controlled by adjusting the composition of catalyst precursor solution during one-pot synthesis processes. In the impregnation process, catalyst content can also be controlled by the times of repeating impregnation process. The overall catalytic activity of catalysts is determined by catalyst content and dispersion. Normally, high dispersion can be achieved at a low catalyst content while it decreases with increasing catalyst content. Hence, increasing catalyst content is effective to improve catalyst performances at low catalyst content. For example, a steady increase in CH₄ conversion with the Ni content from 5 to 20% was observed by Alipour et al. over Ni/Al₂O₃ nanocatalyst during the dry reforming of methane [104]. Dong et al. synthesized a series of Ni catalysts with Ce-ZrO₂ as the support [105], and an upper limit of 15% Ni loading was observed to be beneficial for achieving high CH₄ conversions.

However, increasing catalyst content causes catalyst aggregation when catalyst content reaches a certain level. Li et al. studied a group of Ni/Al₂O₃ catalysts and found that the particle size increased drastically from 7 nm to 49 nm when the Ni loading increased from 0.2 to 10.6% [106]. In the catalytic methane reforming, it has been proved that the carbon formation is structurally favored on large Ni particles [107]. With the increase of the particle size, Alipour et al. observed the increase of

carbon formation with the increase of the Ni loading [104]. In Dong's work [105], when the nickel further increased to 20%, the reaction was quickly stopped as the reactor was plugged by carbon due to the big Ni particle size. Thus it can be concluded that a suitable catalyst loading is crucial to achieve high catalytic activity and stability.

1.2.2.4.5 Limitations of powder-supported catalysts in methane reforming

Although powder-supported catalysts demonstrated many advantages, there are two disadvantages caused by its structure. The first one is mass transfer limitation. As shown in Figure 1-3, there are internal diffusion and external diffusion involved in a catalytic reaction. External diffusion is gas transfer from bulk gas flow to catalyst support surface or backwards. As the majority of catalyst particles are located within internal pore surface of supports, there is an internal gas diffusion from catalyst support surface to internal pore surface.

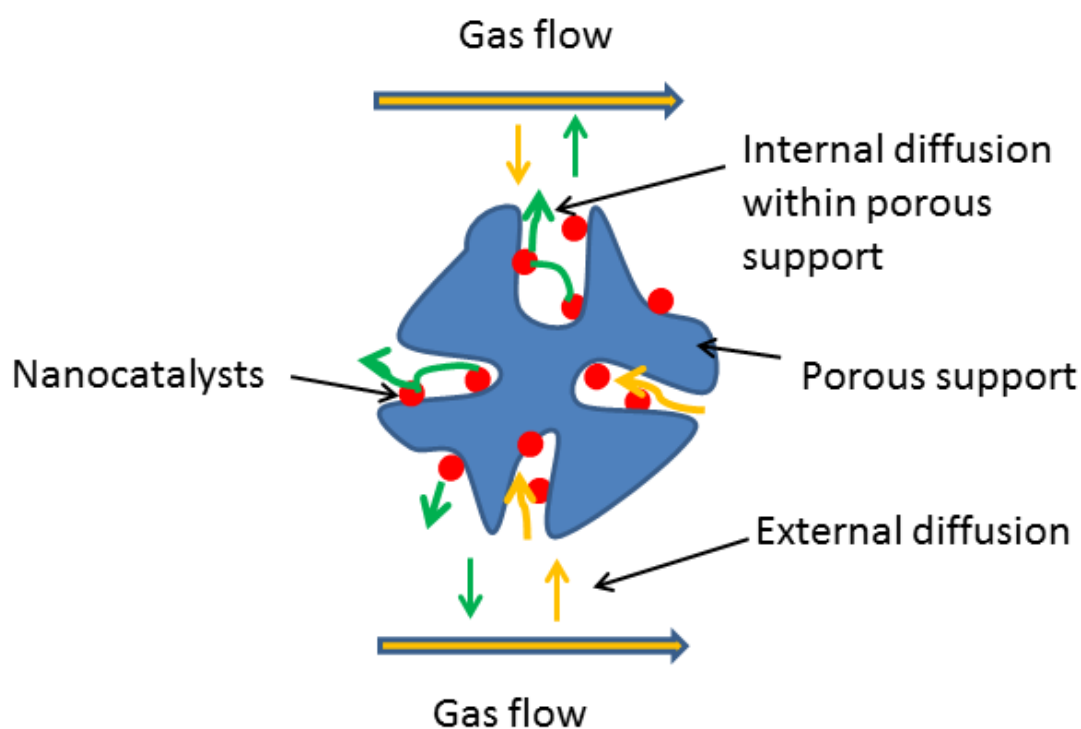


Figure 1-3. Gas diffusion over powder-supported catalysts.

As methane reforming is normally operated at 600-850 °C to achieve high conversion, the catalytic reactions can often be limited by mass transfer. Powder-supported catalysts show more serious diffusion limitation than metal gauze/mesh catalysts and monolith catalysts, because of the existence of the internal diffusion, which depends the particle sizes of catalyst powder. Small catalyst particles have small internal gas diffusion resistance. However, it is unfeasible for practical applications because the small catalyst powders cause a large pressure drop through a powder-packed catalyst bed, especially when high gas velocities are used to achieve high yields or selectivity. To reduce the pressure drop, the powder catalysts are made into big granules or pellets [108, 109]. It greatly exacerbates the internal gas diffusion.

The other disadvantage of powder-supported catalysts in methane reforming is low thermal stability. Both catalyst particles and powder supports can aggregate during catalyst calcination and high temperature reaction. For example, the methane partial oxidation is exothermic, and hot-spots can readily form during the reaction. Moreover, catalysts are normally calcined at low temperatures (below 700 °C) to retain small catalyst particle sizes and high support surface area while catalytic reactions are operated at a higher temperature, such as methane steam and dry reforming [110, 111]. Methane steam reforming is endothermic, and high reaction temperatures are thermodynamically favorable. Catalysts calcined at low temperatures are operated at high temperatures for catalytic reactions, which causes further sintering of catalyst before and during reactions. However, catalyst properties such as particle size are characterized after calcination. Therefore, the characterization results do not necessarily reflect the properties of the catalysts in reactions.

1.3 Significance of this study

The above literature review has shown that many catalysts with different structures have been employed in the conversion of natural gas. Each type of catalyst has advantages and disadvantages. Generally speaking, metal gauze/mesh/foam catalysts and monolith catalysts are structurally advantageous in pressure management, showing low pressure drop under high space velocity. Furthermore, they are less

porous (monolith with wash coat) than the traditional porous catalysts or non-porous (metal gauze/mesh/foam), where the internal diffusion resistance to reactants, desired intermediates and products are improved or eliminated. These advantages are favorable for catalytic methane reforming, which are kinetically fast or operated at elevated temperatures, to maximize the selectivity for desired products. However, the overall catalytic activities of those catalysts, metal gauze/mesh/foam and monolith, are often limited by the low surface area or low volume utilization efficiency of reactors.

Powder-supported catalysts offer high surface areas and therefore high catalytic activity owing to nanosized-catalyst particles in the support. However, this kind of catalysts is suitable for slow reactions due to the presence of internal diffusion. In the cases of the catalytic methane reforming, reactions over a powder-supported catalyst can often be limited by mass transfer within porous supports. The internal diffusion can be minimized by decreasing the catalysts particulates size. However, it would be irreducible in practical when considering the substantial pressure drop through a catalyst bed.

A clear way forward in research and development of catalytic methane reforming is a new catalyst that combines the advantages of the two types of catalysts to achieve both high catalytic activity and fast gas diffusion. Fibrous catalysts are a good candidate to reach the target [112]. There are two main ways to prepare ceramic fibrous catalysts: templating synthesis and electrospinning.

Our group had developed a templating synthesis method using eggshell membrane that is constructed by interwoven protein fibers as the template [113]. The preliminary study of the templated fibrous catalyst was conducted in the partial oxidation of methane, and the templated NiO/CeO₂ catalyst with a Ni content of 47.8 wt% produced 96% of methane conversion at a very short contact time of 98 μs. As a new method, it is not clear how the preparation parameters such as calcination temperature and immersion time would affect the microstructure of the template catalysts and subsequent catalytic performances including methane conversion and carbon formation.

Electrospinning process is a facile way to prepare ceramic fibers with controllable composition and microstructure [114]. However, there are few studies on electrospun fibrous catalysts used in methane reforming. The knowledge on the electrospun fibrous catalysts for methane reforming is desired to develop a new catalyst for efficient natural gas conversion.

This study was designed to contribute to the knowledge gaps identified above. The preparation processes of the two methods were investigated to optimize preparation parameters to achieve high and stable reforming performances. The relationship between catalyst structure and reforming performances was studied, and the merits of the fibrous catalysts were confirmed. In conclusion, fibrous catalysts demonstrated high and stable catalytic activity in methane reforming, and the electrospun fibrous catalysts are promising for practical applications.

1.4 Scope of thesis

The newly developed templating synthesis method using eggshell membrane as the template for catalyst preparation and the performance of the templated fibrous catalysts in the partial oxidation of methane were reported in our previous study. To further study the new method, the thesis will investigate the effects of preparation parameters on catalyst properties including the performance in methane dry/steam reforming (Chapters 3-4). Due to the limited availability and fixed and large fiber diameters of eggshell membrane template, more productive and controllable fibrous catalyst fabrication method, electrospinning, will also be studied in the second part (Chapters 5-6) of my thesis.

Chapter 2 is experimental description. Two methods used in this study for catalyst preparation will be explained in detail: eggshell membrane-templating synthesis and electrospinning process. The experimental setup used to test the catalytic methane reforming and carbon formation will be also described.

Chapters 3-4 will focus on the study of the fibrous NiO/CeO₂ catalyst templated from eggshell membrane. *Chapter 3* will study the carbon formation over fibrous catalysts during dry reforming. Parameters influencing carbon formation will be

investigated, including calcination temperature, Ni content and the gas hourly space velocity. *Chapter 4* will present the effects of the preparation parameters, such as immersion time and calcination temperature, on catalyst properties. The catalytic performances of these catalysts were evaluated for the steam reforming of methane.

Chapters 5-6 will demonstrate the fibrous Ni/Al₂O₃ catalysts prepared by electrospinning process. In *Chapter 5*, high yields of syngas over fibrous Ni/Al₂O₃ catalysts will be reported at the highest recorded gas space velocity during methane partial oxidation. The effect of Ni content on catalyst properties was investigated. In *Chapter 6*, the effect of calcination temperature on catalyst properties will be discussed, including catalyst microstructure, reducibility and catalytic performances in dry reforming.

Chapter 7 will summarize the study and suggest the future work in this field.

1.5 References

- [1] World energy outlook 2014, IEA, ISBN 978-92-64-20804-9, 2014.
- [2] J. Ross, A. Van Keulen, M. Hegarty, K. Seshan, The catalytic conversion of natural gas to useful products, *Catalysis Today*, 30 (1996) 193-199.
- [3] J.G. Speight, *Natural gas: a basic handbook*, Elsevier, 2007.
- [4] A.P. York, T. Xiao, M.L. Green, Brief overview of the partial oxidation of methane to synthesis gas, *Topics in Catalysis*, 22 (2003) 345-358.
- [5] J. Zaman, Oxidative processes in natural gas conversion, *Fuel Processing Technology*, 58 (1999) 61-81.
- [6] A.M. Rabiou, I.M. Yusuf, Industrial Feasibility of Direct Methane Conversion to Hydrocarbons over Fe-Based Fischer Tropsch Catalyst, *Journal of Power and Energy Engineering*, 1 (2013) 41.
- [7] S. Cornot-Gandolphe, Changes in world gas reserves and resources, *Energy exploration & exploitation*, 13 (1995) 3-17.
- [8] J.H. Lunsford, Catalytic conversion of methane to more useful chemicals and fuels: a challenge for the 21st century, *Catalysis Today*, 63 (2000) 165-174.
- [9] R. Burch, S.C. Tsang, Natural gas conversion, *Current Opinion in Solid State and Materials Science*, 2 (1997) 90-93.
- [10] C. Perego, R. Bortolo, R. Zennaro, Gas to liquids technologies for natural gas reserves valorization: The Eni experience, *Catalysis Today*, 142 (2009) 9-16.
- [11] A. Holmen, O. Olsvik, O. Rokstad, Pyrolysis of natural gas: chemistry and process concepts, *Fuel Processing Technology*, 42 (1995) 249-267.

- [12] B.C. Enger, R. Lødeng, A. Holmen, A review of catalytic partial oxidation of methane to synthesis gas with emphasis on reaction mechanisms over transition metal catalysts, *Applied Catalysis A: General*, 346 (2008) 1-27.
- [13] N. Parkyns, C. Warburton, J. Wilson, Natural gas conversion to liquid fuels and chemicals: Where does it stand?, *Catalysis today*, 18 (1993) 385-442.
- [14] M.J. Gradassi, N. Wayne Green, Economics of natural gas conversion processes, *Fuel Processing Technology*, 42 (1995) 65-83.
- [15] A. Holmen, Direct conversion of methane to fuels and chemicals, *Catalysis Today*, 142 (2009) 2-8.
- [16] T.V. Choudhary, V.R. Choudhary, Energy - Efficient Syngas Production through Catalytic Oxy - Methane Reforming Reactions, *Angewandte Chemie International Edition*, 47 (2008) 1828-1847.
- [17] M. Alvarez-Galvan, N. Mota, M. Ojeda, S. Rojas, R. Navarro, J. Fierro, Direct methane conversion routes to chemicals and fuels, *Catalysis Today*, 171 (2011) 15-23.
- [18] T.J. Hall, J.S. Hargreaves, G.J. Hutchings, R.W. Joyner, S.H. Taylor, Catalytic synthesis of methanol and formaldehyde by partial oxidation of methane, *Fuel processing technology*, 42 (1995) 151-178.
- [19] V. Sokolovskii, N. Coville, A. Parmaliana, I. Eskendirov, M. Makoa, Methane partial oxidation. Challenge and perspective, *Catalysis Today*, 42 (1998) 191-195.
- [20] Y. San Su, J.Y. Ying, W.H. Green, Upper bound on the yield for oxidative coupling of methane, *Journal of Catalysis*, 218 (2003) 321-333.
- [21] V.R. Choudhary, K.C. Mondal, CO₂ reforming of methane combined with steam reforming or partial oxidation of methane to syngas over NdCoO₃ perovskite-type mixed metal-oxide catalyst, *Applied energy*, 83 (2006) 1024-1032.

- [22] K. Aasberg-Petersen, I. Dybkjær, C. Ovesen, N. Schjødt, J. Sehested, S. Thomsen, Natural gas to synthesis gas—catalysts and catalytic processes, *Journal of Natural Gas Science and Engineering*, 3 (2011) 423-459.
- [23] S.S. Bharadwaj, L.D. Schmidt, Catalytic partial oxidation of natural gas to syngas, *Fuel Processing Technology*, 42 (1995) 109-127.
- [24] J.P. Van Hook, Methane-steam reforming, *Catalysis Reviews—Science and Engineering*, 21 (1980) 1-51.
- [25] E. Achenbach, E. Riensche, Methane/steam reforming kinetics for solid oxide fuel cells, *Journal of Power Sources*, 52 (1994) 283-288.
- [26] J.H. Edwards, A.M. Maitra, The chemistry of methane reforming with carbon dioxide and its current and potential applications, *Fuel Processing Technology*, 42 (1995) 269-289.
- [27] H. Er-Rbib, C. Bouallou, F. Werkoff, Dry reforming of methane—review of feasibility studies, *Chemical Engineering*, 29 (2012).
- [28] B. Christian Enger, R. Lødeng, A. Holmen, A review of catalytic partial oxidation of methane to synthesis gas with emphasis on reaction mechanisms over transition metal catalysts, *Applied Catalysis A: General*, 346 (2008) 1-27.
- [29] S. Tsang, J. Claridge, M. Green, Recent advances in the conversion of methane to synthesis gas, *Catalysis Today*, 23 (1995) 3-15.
- [30] D. Wilhelm, D. Simbeck, A. Karp, R. Dickenson, Syngas production for gas-to-liquids applications: technologies, issues and outlook, *Fuel processing technology*, 71 (2001) 139-148.
- [31] Y.H. Hu, E. Ruckenstein, Catalytic conversion of methane to synthesis gas by partial oxidation and CO₂ reforming, *Advances in catalysis*, 48 (2004) 297-345.

- [32] J. Xu, G.F. Froment, Methane steam reforming, methanation and water - gas shift: I. Intrinsic kinetics, *AIChE Journal*, 35 (1989) 88-96.
- [33] P. Ferreira-Aparicio, I. Rodríguez-Ramos, J. Anderson, A. Guerrero-Ruiz, Mechanistic aspects of the dry reforming of methane over ruthenium catalysts, *Applied Catalysis A: General*, 202 (2000) 183-196.
- [34] M.C.J. Bradford, M.A. Vannice, Catalytic reforming of methane with carbon dioxide over nickel catalysts II. Reaction kinetics, *Applied Catalysis A: General*, 142 (1996) 97-122.
- [35] K.-S. Ha, J.W. Bae, K.-J. Woo, K.-W. Jun, Efficient utilization of greenhouse gas in a gas-to-liquids process combined with carbon dioxide reforming of methane, *Environmental science & technology*, 44 (2010) 1412-1417.
- [36] J.K. Dahl, A.W. Weimer, A. Lewandowski, C. Bingham, F. Bruetsch, A. Steinfeld, Dry reforming of methane using a solar-thermal aerosol flow reactor, *Industrial & engineering chemistry research*, 43 (2004) 5489-5495.
- [37] A. Wörner, R. Tamme, CO₂ reforming of methane in a solar driven volumetric receiver–reactor, *Catalysis today*, 46 (1998) 165-174.
- [38] B. Fidalgo, J.Á. Menendez, Carbon Materials as Catalysts for Decomposition and CO₂ Reforming of Methane: A Review, *Chinese Journal of Catalysis*, 32 (2011) 207-216.
- [39] J. Edwards, A. Maitra, The chemistry of methane reforming with carbon dioxide and its current and potential applications, *Fuel Processing Technology*, 42 (1995) 269-289.
- [40] M. Fichtner, J. Mayer, D. Wolf, K. Schubert, Microstructured rhodium catalysts for the partial oxidation of methane to syngas under pressure, *Industrial & engineering chemistry research*, 40 (2001) 3475-3483.

- [41] Q. Jing, H. Lou, L. Mo, J. Fei, X. Zheng, Combination of CO₂ reforming and partial oxidation of methane over Ni/BaO-SiO₂ catalysts to produce low H₂/CO ratio syngas using a fluidized bed reactor, *Journal of Molecular Catalysis A: Chemical*, 212 (2004) 211-217.
- [42] A. Smith, J. Klosek, A review of air separation technologies and their integration with energy conversion processes, *Fuel Processing Technology*, 70 (2001) 115-134.
- [43] W. Haihui, C. You, Y. Weishen, Partial oxidation of methane to syngas in tubular oxygen-permeable reactor, *Chinese Science Bulletin*, 47 (2002) 534-537.
- [44] B. Horner, Knitted platinum alloy gauzes, *Platinum Metals Review*, 37 (1993) 76-85.
- [45] A. Heywood, The Recovery of Platinum from Ammonia Oxidation Catalysts, *Platinum Metals Review*, 26 (1982) 28-32.
- [46] C.N. Satterfield, D.H. Cortez, Mass transfer characteristics of woven-wire screen catalysts, *Industrial & Engineering Chemistry Fundamentals*, 9 (1970) 613-620.
- [47] A. Kołodziej, J. Łojewska, M. Jaroszyński, A. Gancarczyk, P. Jodłowski, Heat transfer and flow resistance for stacked wire gauzes: Experiments and modelling, *International Journal of Heat and Fluid Flow*, 33 (2012) 101-108.
- [48] A. Kołodziej, J. Łojewska, Experimental and modelling study on flow resistance of wire gauzes, *Chemical Engineering and Processing: Process Intensification*, 48 (2009) 816-822.
- [49] B. Monnerat, L. Kiwi-Minsker, A. Renken, Hydrogen production by catalytic cracking of methane over nickel gauze under periodic reactor operation, *Chemical engineering science*, 56 (2001) 633-639.

- [50] A. Kołodziej, J. Łojewska, Optimization of structured catalyst carriers for VOC combustion, *Catalysis today*, 105 (2005) 378-384.
- [51] K.H. Hofstad, O. Rokstad, A. Holmen, Partial oxidation of methane over platinum metal gauze, *Catalysis letters*, 36 (1996) 25-30.
- [52] U. Flesch, R. Dahl, R. Peters, D. Stöver, Properties of Nickel Mesh as a Methane Steam Reforming Catalyst and its Application in SOFCs, in: *Functional Materials*, Wiley-VCH Verlag GmbH & Co. KGaA, 2006, pp. 187-192.
- [53] A. Weber, B. Sauer, A.C. Müller, D. Herbstritt, E. Ivers-Tiffée, Oxidation of H₂, CO and methane in SOFCs with Ni/YSZ-cermet anodes, *Solid State Ionics*, 152–153 (2002) 543-550.
- [54] E. Bergene, O. Tronstad, A. Holmen, Surface areas of Pt–Rh catalyst gauzes used for ammonia oxidation, *Journal of Catalysis*, 160 (1996) 141-147.
- [55] M. Twigg, J. Richardson, Theory and applications of ceramic foam catalysts, *Chemical Engineering Research and Design*, 80 (2002) 183-189.
- [56] M.V. Twigg, J.T. Richardson, Fundamentals and applications of structured ceramic foam catalysts, *Industrial & engineering chemistry research*, 46 (2007) 4166-4177.
- [57] L.-P. Lefebvre, J. Banhart, D. Dunand, Porous metals and metallic foams: current status and recent developments, *Advanced Engineering Materials*, 10 (2008) 775-787.
- [58] Y. Li, Q. Zhang, R. Chai, G. Zhao, Y. Liu, Y. Lu, Structured Ni - CeO₂ - Al₂O₃/Ni - Foam Catalyst with Enhanced Heat Transfer for Substitute Natural Gas Production by Syngas Methanation, *ChemCatChem*, (2015).

- [59] A. Bhattacharya, V. Calmidi, R. Mahajan, Thermophysical properties of high porosity metal foams, *International Journal of Heat and Mass Transfer*, 45 (2002) 1017-1031.
- [60] M. Phanikumar, R. Mahajan, Non-Darcy natural convection in high porosity metal foams, *International Journal of Heat and Mass Transfer*, 45 (2002) 3781-3793.
- [61] J. Banhart, Manufacture, characterisation and application of cellular metals and metal foams, *Progress in materials science*, 46 (2001) 559-632.
- [62] G. Pontikakis, G. Koltsakis, A. Stamatelos, Dynamic filtration modeling in foam filters for diesel exhaust, *Chemical Engineering Communications*, 188 (2001) 21-46.
- [63] O. Sanz, F.J. Echave, M. Sánchez, A. Monzón, M. Montes, Aluminium foams as structured supports for volatile organic compounds (VOCs) oxidation, *Applied Catalysis A: General*, 340 (2008) 125-132.
- [64] K. Boomsma, D. Poulidakos, F. Zwick, Metal foams as compact high performance heat exchangers, *Mechanics of materials*, 35 (2003) 1161-1176.
- [65] R. Hayes, A. Rojas, J. Mmbaga, The effective thermal conductivity of monolith honeycomb structures, *Catalysis Today*, 147 (2009) S113-S119.
- [66] J. Gascon, J. van Ommen, J. Moulijn, F. Kapteijn, Structuring catalyst and reactor—an inviting avenue to process intensification, *Catalysis Science & Technology*, (2015).
- [67] R. Singh, H. Kasana, Computational aspects of effective thermal conductivity of highly porous metal foams, *Applied thermal engineering*, 24 (2004) 1841-1849.
- [68] X. Cheng, X.T. Bi, A review of recent advances in selective catalytic NO_x reduction reactor technologies, *Particuology*, 16 (2014) 1-18.

- [69] R. Horn, K.A. Williams, N.J. Degenstein, A. Bitsch-Larsen, D. Dalle Nogare, S.A. Tupy, L.D. Schmidt, Methane catalytic partial oxidation on autothermal Rh and Pt foam catalysts: Oxidation and reforming zones, transport effects, and approach to thermodynamic equilibrium, *Journal of Catalysis*, 249 (2007) 380-393.
- [70] L. Coleman, E. Croiset, W. Epling, M. Fowler, R. Hudgins, Evaluation of Foam Nickel for the Catalytic Partial Oxidation of Methane, *Catalysis Letters*, 128 (2009) 144-153.
- [71] S. Kim, C.-W. Lee, A review on manufacturing and application of open-cell metal foam, *Procedia Materials Science*, 4 (2014) 305-309.
- [72] L. Sang, B. Sun, H. Tan, C. Du, Y. Wu, C. Ma, Catalytic reforming of methane with CO₂ over metal foam based monolithic catalysts, *international journal of hydrogen energy*, 37 (2012) 13037-13043.
- [73] Y. Du, C. Zhao, Y. Zhu, Steam Reforming of Methane in Metal-foam Filled Reactor, (2014).
- [74] N. Gokon, Y. Yamawaki, D. Nakazawa, T. Kodama, Kinetics of methane reforming over Ru/ γ -Al₂O₃-catalyzed metallic foam at 650–900° C for solar receiver-absorbers, *international journal of hydrogen energy*, 36 (2011) 203-215.
- [75] H. Yu, H. Chen, M. Pan, Y. Tang, K. Zeng, F. Peng, H. Wang, Effect of the metal foam materials on the performance of methanol steam micro-reformer for fuel cells, *Applied Catalysis A: General*, 327 (2007) 106-113.
- [76] L. Giani, C. Cristiani, G. Groppi, E. Tronconi, Washcoating method for Pd/ γ -Al₂O₃ deposition on metallic foams, *Applied Catalysis B: Environmental*, 62 (2006) 121-131.
- [77] I. Aartun, B. Silberova, H. Venvik, P. Pfeifer, O. Görke, K. Schubert, A. Holmen, Hydrogen production from propane in Rh-impregnated metallic microchannel reactors and alumina foams, *Catalysis today*, 105 (2005) 469-478.

- [78] J.L. Williams, Monolith structures, materials, properties and uses, *Catalysis Today*, 69 (2001) 3-9.
- [79] V. Tomašić, F. Jović, State-of-the-art in the monolithic catalysts/reactors, *Applied Catalysis A: General*, 311 (2006) 112-121.
- [80] W.B. Kolb, A. Papadimitriou, R. Cerro, D. Leavitt, J. Summers, The ins and outs of coating monolithic structures, *Chemical Engineering Progress*; (United States), 89 (1993).
- [81] J. Ross, 4. Catalyst Preparation, in: *Heterogeneous Catalysis*, Elsevier, pp. 84.
- [82] G. Groppi, E. Tronconi, Honeycomb supports with high thermal conductivity for gas/solid chemical processes, *Catalysis today*, 105 (2005) 297-304.
- [83] V. Tomašić, Z. Gomzi, Development of the structured catalysts for the exhaust gas treatment, (2001).
- [84] M.J. Stutz, D. Poulikakos, Optimum washcoat thickness of a monolith reactor for syngas production by partial oxidation of methane, *Chemical Engineering Science*, 63 (2008) 1761-1770.
- [85] R.M. Heck, S. Gulati, R.J. Farrauto, The application of monoliths for gas phase catalytic reactions, *Chemical Engineering Journal*, 82 (2001) 149-156.
- [86] A. Cybulski, J.A. Moulijn, *Structured catalysts and reactors*, CRC Press, 2005.
- [87] A. Cybulski, J.A. Moulijn, Monoliths in heterogeneous catalysis, *Catalysis Reviews—Science and Engineering*, 36 (1994) 179-270.
- [88] W.M. Carty, P.W. Lednor, Monolithic ceramics and heterogeneous catalysts: honeycombs and foams, *Current Opinion in Solid State and Materials Science*, 1 (1996) 88-95.

- [89] F. Pinna, Supported metal catalysts preparation, *Catalysis Today*, 41 (1998) 129-137.
- [90] J.A. Schwarz, C. Contescu, A. Contescu, Methods for preparation of catalytic materials, *Chemical Reviews*, 95 (1995) 477-510.
- [91] H. Liu, D. Ma, R.A. Blackley, W. Zhou, X. Bao, Highly active mesostructured silica hosted silver catalysts for CO oxidation using the one-pot synthesis approach, *Chem. Commun.*, (2008) 2677-2679.
- [92] Y.-S. Seo, Y.-S. Jung, W.-L. Yoon, I.-G. Jang, T.-W. Lee, The effect of Ni content on a highly active Ni-Al₂O₃ catalyst prepared by the homogeneous precipitation method, *International Journal of Hydrogen Energy*, 36 (2011) 94-102.
- [93] M. Crişan, M. Zaharescu, V.D. Kumari, M. Subrahmanyam, D. Crişan, N. Drăgan, M. Răileanu, M. Jitianu, A. Rusu, G. Sadanandam, J. Krishna Reddy, Sol-gel based alumina powders with catalytic applications, *Applied Surface Science*, 258 (2011) 448-455.
- [94] K. Balakrishnan, R.D. Gonzalez, Preparation of Pt/alumina catalysts by the sol-gel method, *Journal of Catalysis*, 144 (1993) 395-413.
- [95] Y. Chen, W. Zhou, Z. Shao, N. Xu, Nickel catalyst prepared via glycine nitrate process for partial oxidation of methane to syngas, *Catalysis Communications*, 9 (2008) 1418-1425.
- [96] J. Chen, R. Wang, J. Zhang, F. He, S. Han, Effects of preparation methods on properties of Ni/CeO₂-Al₂O₃ catalysts for methane reforming with carbon dioxide, *Journal of Molecular Catalysis A: Chemical*, 235 (2005) 302-310.
- [97] H.Y. Wang, E. Ruckenstein, CO₂ reforming of CH₄ over Co/MgO solid solution catalysts — effect of calcination temperature and Co loading, *Applied Catalysis A: General*, 209 (2001) 207-215.

- [98] F. Boccuzzi, A. Chiorino, M. Manzoli, P. Lu, T. Akita, S. Ichikawa, M. Haruta, Au/TiO₂ Nanosized Samples: A Catalytic, TEM, and FTIR Study of the Effect of Calcination Temperature on the CO Oxidation, *Journal of Catalysis*, 202 (2001) 256-267.
- [99] C.R. Jung, J. Han, S.W. Nam, T.H. Lim, S.A. Hong, H.I. Lee, Selective oxidation of CO over CuO-CeO₂ catalyst: effect of calcination temperature, *Catalysis Today*, 93-95 (2004) 183-190.
- [100] H. Ozdemir, M.A.F. Oksuzomer, M.A. Gurkaynak, Effect of the calcination temperature on Ni/MgAl₂O₄ catalyst structure and catalytic properties for partial oxidation of methane, *Fuel*, 116 (2014) 63-70.
- [101] J. Guo, H. Lou, Y. Zhu, X. Zheng, CO₂ Reforming of CH₄ over Nickel and Cobalt Catalysts Prepared from La-Based Perovskite Precursors, *Journal of Natural Gas Chemistry*, 12 (2003) 17-22.
- [102] H.-S. Roh, K.-W. Jun, W.-S. Dong, S.-E. Park, Y.-S. Baek, Highly stable Ni catalyst supported on Ce-ZrO₂ for oxy-steam reforming of methane, *Catalysis letters*, 74 (2001) 31-36.
- [103] J.G. Seo, M.H. Youn, J.S. Chung, I.K. Song, Effect of calcination temperature of mesoporous nickel-alumina catalysts on their catalytic performance in hydrogen production by steam reforming of liquefied natural gas (LNG), *Journal of Industrial and Engineering Chemistry*, 16 (2010) 795-799.
- [104] Z. Alipour, M. Rezaei, F. Meshkani, Effect of Ni loadings on the activity and coke formation of MgO-modified Ni/Al₂O₃ nanocatalyst in dry reforming of methane, *Journal of Energy Chemistry*, 23 (2014) 633-638.
- [105] W.-S. Dong, H.-S. Roh, K.-W. Jun, S.-E. Park, Y.-S. Oh, Methane reforming over Ni/Ce-ZrO₂ catalysts: effect of nickel content, *Applied Catalysis A: General*, 226 (2002) 63-72.

- [106] B. Li, K. Maruyama, M. Nurunnabi, K. Kunimori, K. Tomishige, Effect of Ni loading on catalyst bed temperature in oxidative steam reforming of methane over α -Al₂O₃-supported Ni catalysts, *Industrial & engineering chemistry research*, 44 (2005) 485-494.
- [107] S. Xu, R. Zhao, X.L. Wang, Highly coking resistant and stable Ni/Al₂O₃ catalysts prepared by W/O microemulsion for partial oxidation of methane, *Fuel Processing Technology*, 86 (2004) 123-133.
- [108] S. Specchia, L.D. Vella, B. Lorenzut, T. Montini, V. Specchia, P. Fornasiero, Effect of the Catalyst Load on Syngas Production in Short Contact Time Catalytic Partial Oxidation Reactors, *Industrial & Engineering Chemistry Research*, 49 (2010) 1010-1017.
- [109] H. Tanaka, R. Kaino, K. Okumura, T. Kizuka, K. Tomishige, Catalytic performance and characterization of Rh-CeO₂/MgO catalysts for the catalytic partial oxidation of methane at short contact time, *Journal of Catalysis*, 268 (2009) 1-8.
- [110] N. Rahemi, M. Haghghi, A.A. Babaluo, M.F. Jafari, S. Allahyari, The effect of the calcination temperature on the physicochemical properties and catalytic activity in the dry reforming of methane over a Ni-Co/Al₂O₃-ZrO₂ nanocatalyst prepared by a hybrid impregnation-plasma method, *Catalysis Science & Technology*, 3 (2013) 3183-3191.
- [111] Y. Zheng, Y. Wei, K. Li, X. Zhu, H. Wang, Y. Wang, Chemical-looping steam methane reforming over macroporous CeO₂-ZrO₂ solid solution: Effect of calcination temperature, *International Journal of Hydrogen Energy*, 39 (2014) 13361-13368.
- [112] E. Reichelt, M.P. Heddrich, M. Jahn, A. Michaelis, Fiber based structured materials for catalytic applications, *Applied Catalysis A: General*, 476 (2014) 78-90.

[113] D.H. Dong, X. Shao, Z.T. Wang, C. Lievens, J.F. Yao, H.T. Wang, C.Z. Li, Fibrous NiO/CeO₂ nanocatalysts for the partial oxidation of methane at microsecond contact times, RSC Adv., 3 (2013) 1341-1345.

[114] Y. Dai, W. Liu, E. Formo, Y. Sun, Y. Xia, Ceramic nanofibers fabricated by electrospinning and their applications in catalysis, environmental science, and energy technology, Polymers for Advanced Technologies, 22 (2011) 326-338.

Every reasonable effort has been made to acknowledge the owners of copyright materials. I would be pleased to hear from any copyright owner who has been omitted or incorrectly acknowledged.

Chapter 2

Experimental methods

2.1 Catalyst preparation

Two methods were used for the preparation of fibrous catalysts in this study: eggshell membrane-templating and electrospinning.

2.1.1 Eggshell membrane-templating

Bio-templates have attracted a great amount of research interests due to their distinctive structures. The structures have been duplicated in many materials by a templating process. The examples of these bio-templates include cage-shaped protein, the wings of the butterfly, wood, plant leaves, DNA and swim bladder membrane [1-5].

Eggshell membrane (ESM) has a fibrous structure constructed by interwoven protein fibers. In this study, ESM was employed as the template to produce fibrous catalysts. ESM bonded to eggshell has three layers: outer shell membrane, inner shell membrane and limiting membrane [6]. The limiting membrane doesn't have fibrous structure. After remove the limiting membrane, the two layers reserved were used as a template. The principle of the templating synthesis and application in CPOM is shown in Figure 2-1 [7].

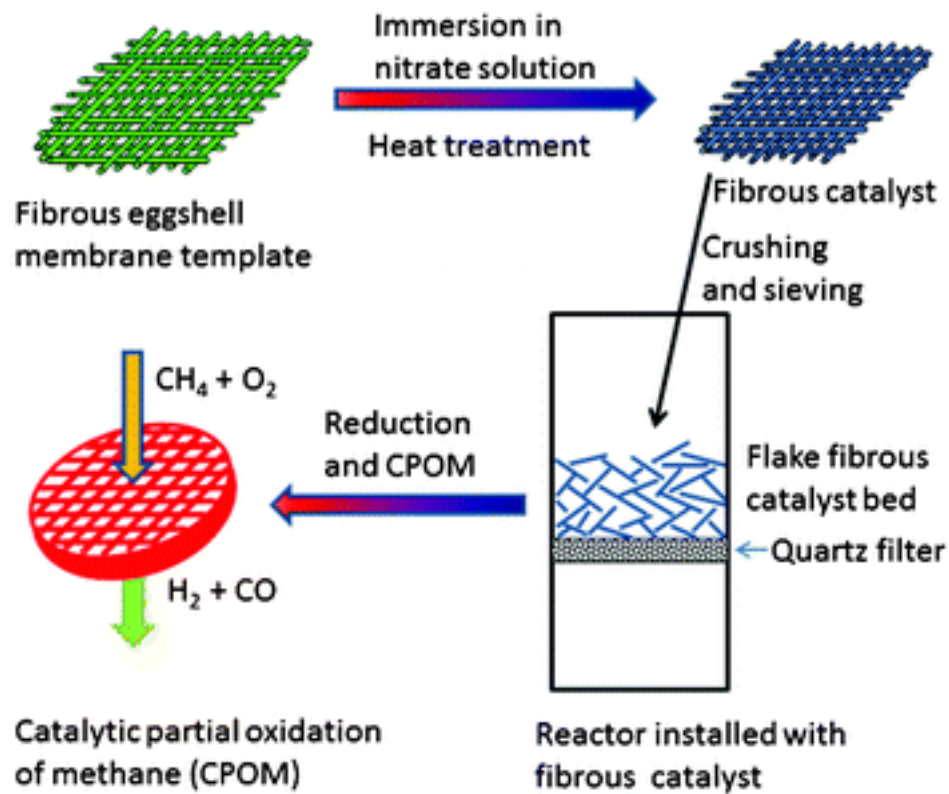


Figure 2-1. Schematic representation of the one-step template synthesis of fibrous NiO/CeO₂ catalysts for the CPOM at microsecond contact times (Reproduced from Ref. 7 with permission from the Royal Society of Chemistry).

ESM is immersed in a solution containing catalyst and support metal ions, and then protein fibers are soaked with the solution. Metal ions are absorbed by protein fibers through ion exchange, forming protein-metal ion composite fibers after drying. The subsequent heat treatment/calcination removes organic compound and finally produces ceramic catalysts with catalyst particles supported on ceramic porous scaffold.

The procedure of templating synthesis is shown in Figure 2-2.

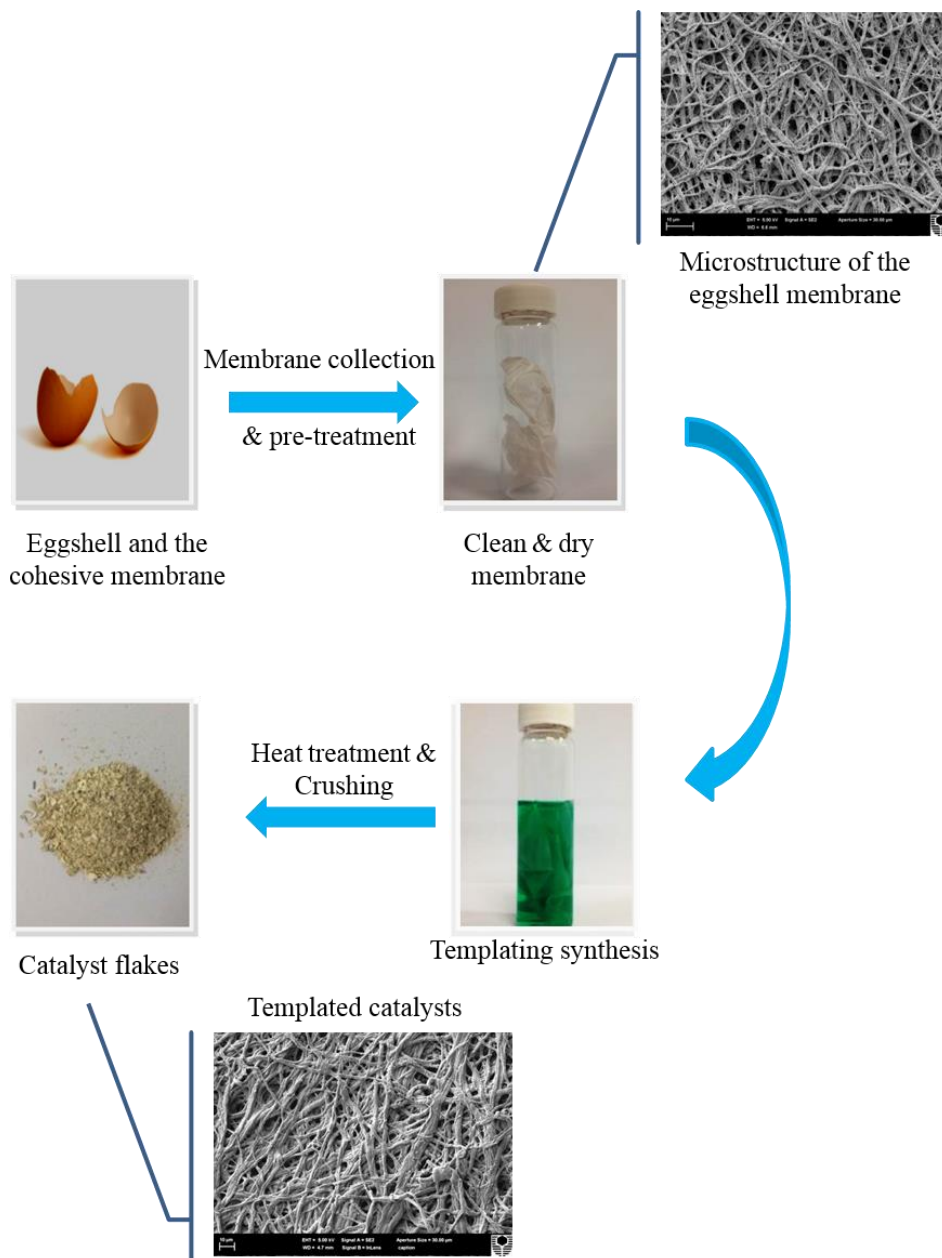


Figure 2-2. A schematic diagram of the templating synthesis process.

Eggshells were collected from chicken eggs. The carbonate eggshell was removed by immersing the eggshell in nitric acid (about 1M). The ESM was separated from carbonate shell after immersion for about 5 minutes. The ESM was washed with deionized water to remove big protein particles and the limiting membrane layer, followed by a drying process. Then, the dried ESM was immersed in a $\text{Ni}(\text{NO}_3)_2 \cdot 6\text{H}_2\text{O}$ and $\text{Ce}(\text{NO}_3)_3 \cdot 6\text{H}_2\text{O}$ solution. After the immersion for about 3 hours, metal ions (Ni^{2+} and Ce^{3+}) were absorbed into the fiber body, forming a metal-organic composite. The metal-organic composite was taken out of the solution and

the excessive solution on the membrane surface was removed by tissue. Subsequently, the metal-organic composite was dried and calcined at a pre-set temperature up to 1100°C to remove organics and form ceramic fibers. Those catalyst mats were finally crushed into small flakes (500-600 μm) for catalytic test.

Additional details about the preparation procedures and parameters are shown in **3.2.1** and **4.2.1**.

2.1.2 Electrospinning

Electrospinning is an effective method to fabricate nanofibers and fiber-structured materials. Many fibrous materials have been successfully fabricated such as metals, ceramics and polymers [8-10].

A schematic diagram of basic electrospinning setup is shown in Figure 2-3. There are mainly three parts in a electrospinning setup: a high voltage generator, a capillary needle where the spinnable solution would be ejected, and a metal collector where electrospun fibers would deposit on [11]. The spinnable solution is delivered by a pump from outside the electric field to the tip of the needle. The solution droplet formed at the tip of needle would be charged, forming the Taylor cone under the electric force, surface tension, electrostatic repulsion and gravity. Further increasing the strength of the electric field, the droplet will be ejected, forming fibers. Before reaching the collector, the fibers are further stretched and dried, and the dimension of the fibers would be greatly reduced. Those fibers are finally deposited on the collector [12, 13].

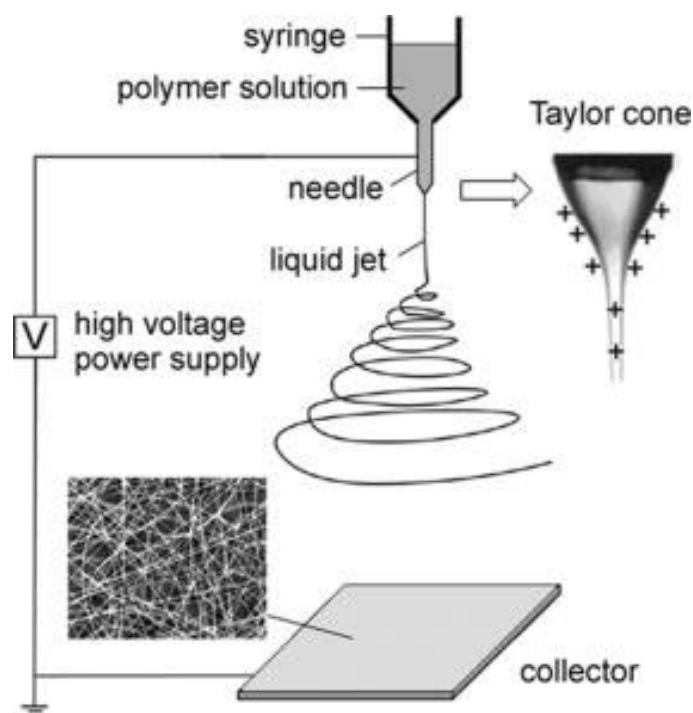


Figure 2-3. A schematic diagram of a basic electrospinning setup [11]. (Reprinted with permission John Wiley and Sons)

The fabrication of fibrous catalysts via electrospinning was carried out on NABOND-NEU, shown in Figure 2-4. The spinning process and the properties of the spun fibers are greatly affected by the physic/chemical properties of the solution, such as solution viscosity, solvent volatility and the concentration of the polymer/metal precursor [14]. Several solvents that were widely used in literature such as deionized water, ethanol, DMF and acetic acid were screened. Considering solvent boiling point and the solubility, deionized water and ethanol were selected to be the solvent in this study. In consideration of the ambient temperature and humidity, the weight ratio of $\text{H}_2\text{O}/\text{CH}_3\text{CH}_2\text{OH}$ was set to 4 for a smooth and continuous spinning. With a higher ethanol content, the spinning process would be readily stopped, because the solution droplet formed on the tip of needle would be quickly dried blocking the needle as the result of solvent evaporation. However, reducing the ethanol content makes the spinning process harder due to the high surface tension of deionized water.

Polymer property as well as its concentration in solution could greatly affect fiber morphology; normally high concentration and molecular weight (M_w) yield big fibers [15]. Polyvinylpyrrolidone (PVP) with an M_w of 1300000 was finally selected for its high dissolvability in various solvents. In order to get fibers that are strong enough to undertake the high temperature calcination and the reforming test, the PVP concentration was finally set to 13-15% to fabricate robust fibers. Tentative experiments show that tiny beads, rather than continuous fiber, were preferred when the PVP concentration was lower than 8%. Increasing PVP concentration (>15%) high voltage was required to overcome the high viscosity of the solution, and fibers spun with high PVP concentration show a wide dimension distribution.

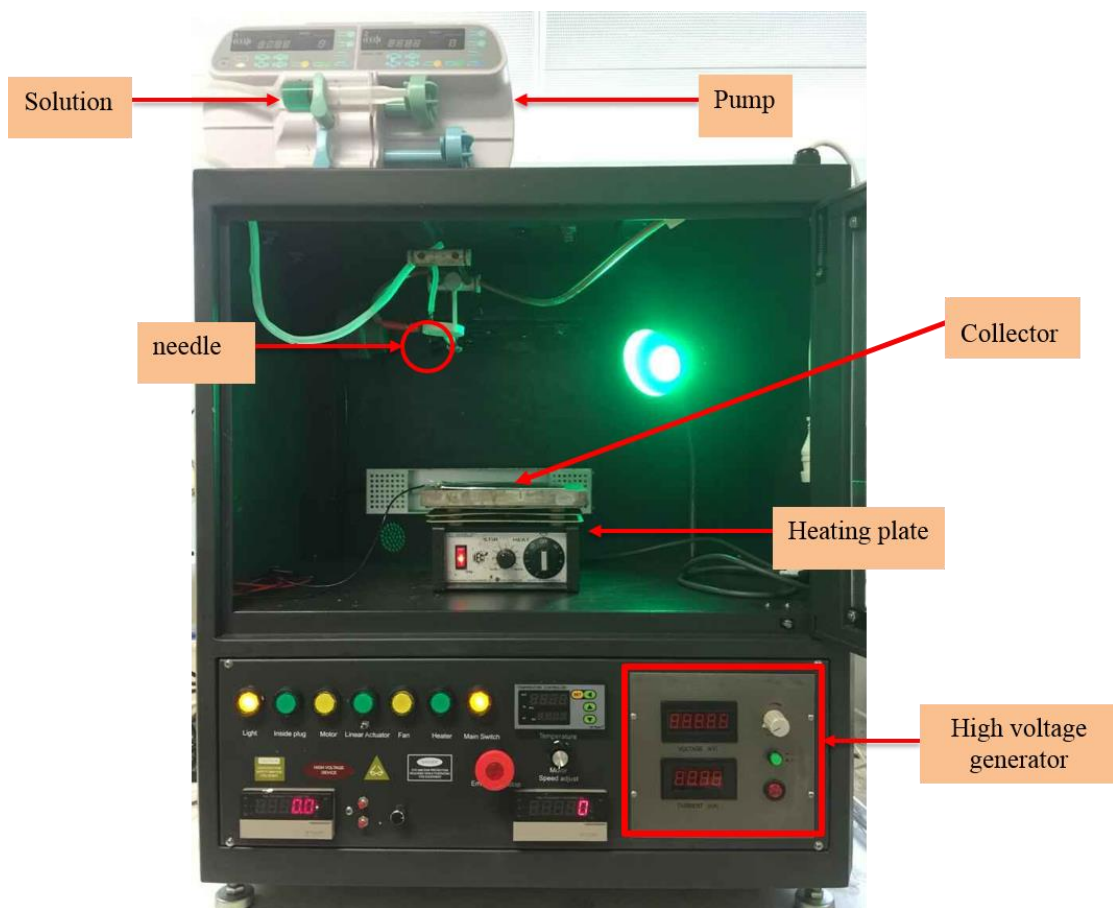


Figure 2-4. NABOND-NEU electrospinning setup.

Considering the solubility and accessibility, nitrates were finally employed, and the concentration was optimized to form strong ceramic fibers. Fibers with small

dimension could be spun with a solution that is low in precursor concentration, but those slim fibers are readily be deformed by high temperature calcination.

Once spinning solution is prepared, the morphology of fiber product, such as fiber diameter and fibrous mate porosity, are mainly controlled by two main parameters: flow rate and strength of the electric field. A high flow rate and low electric force form fibers with big diameters [16]. In a typical spinning process, an electric field of 2.4 kV/cm was formed between the needle and collector, and the metal-PVP solution was delivered into the electric field by a pump that was mounted on the top of the spinning chamber through a double-layer plastic tubing at a flow rate of 0.5 ml/min. The flow rate and the strength of the electric field were determined based on the requirement for a continuous spinning process and desirable product morphology. Those spun fibers were deposited on the collector that was wrapped by aluminum foil for ease collection.

As the ambient humidity could be readily absorbed by PVP and re-melt newly formed fibers, a heating plate was placed under the collector to increase the collector temperature and avoid the re-melt of fiber. The as-spun fibers were collected from the aluminum foil and sent to oven at 55°C waiting for further treatment. In order to investigate the catalytic capability of the spun catalysts, the metal-polymer fiber would be calcined at high temperatures (700-1000 °C) to burn the polymer and crystallize the catalysts.

2.2 Catalyst evaluating system

Methane reforming tests were carried out in a fixed-bed quartz reactor in a designated experiment rig, the schematic diagram of the testing system is shown in Figure 2-5.

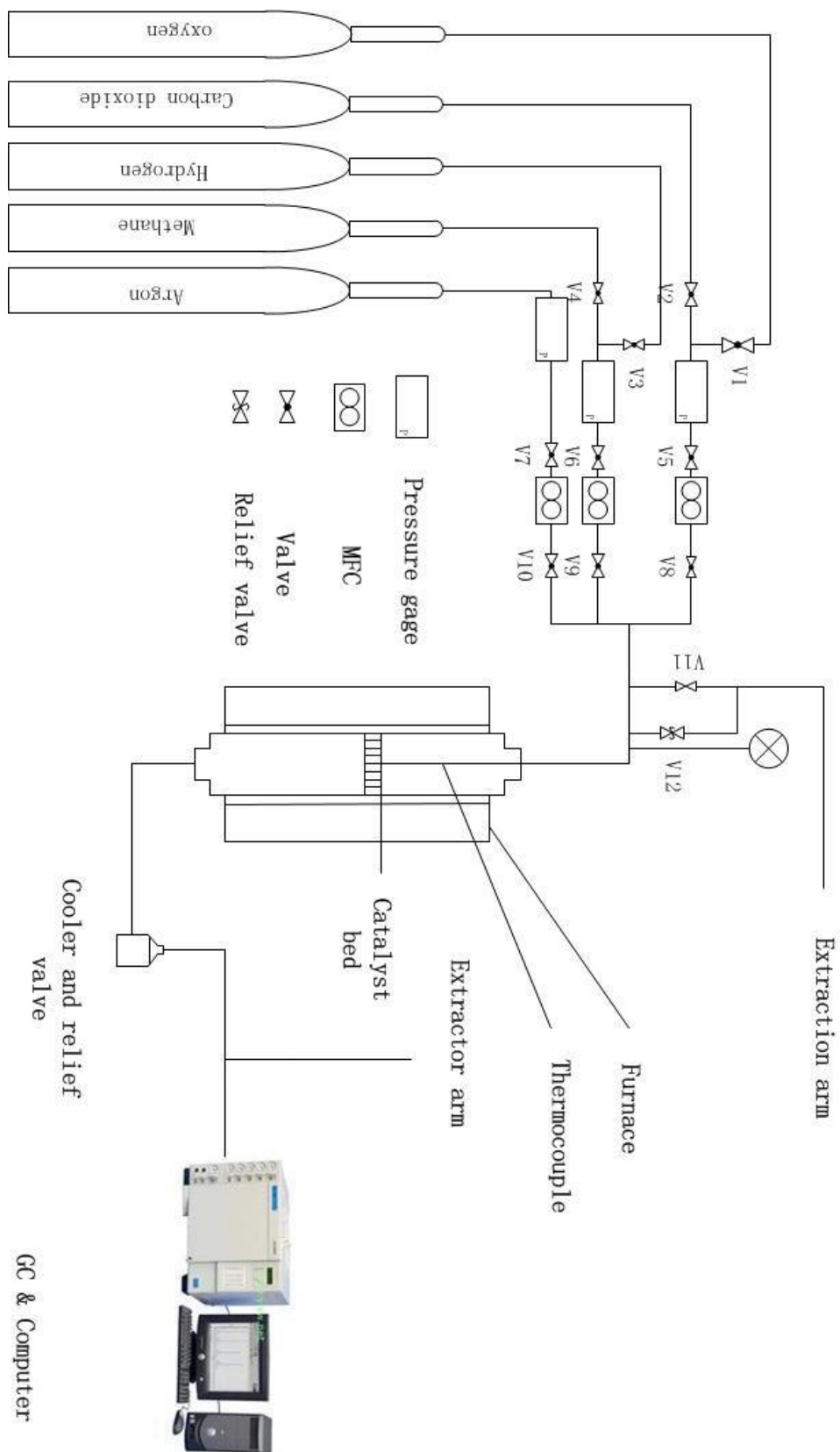


Figure 2-5. A schematic diagram of the catalyst testing system.

In order to have a good control over gas hourly space velocity, reactors with two different internal diameters (10 and 20 mm) were used in different reforming tests. Samples were loaded on a quartz frit that was positioned in the middle of the quartz reactor (see Figure 2-6), and then the quartz tube reactor was positioned vertically in the furnace.

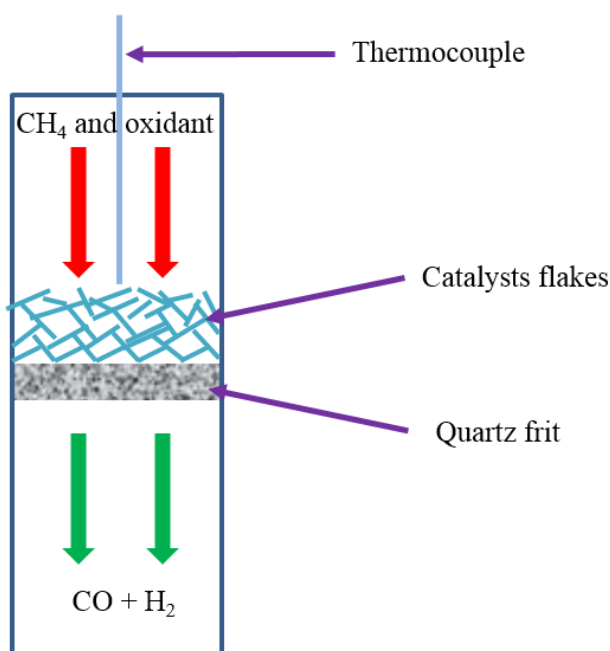


Figure 2-6. A schematic diagram of the arrangement of catalyst flakes in reactor.

During the reduction of catalysts and reforming test, a K-type thermocouple was used to monitor temperature in the vicinity of the catalyst bed. To avoid any possible effects of the thermocouple to the catalysts, the thermocouple was placed right above the catalyst bed. Before test, catalysts were reduced under a stream of H₂ (20 vol %) balanced with Ar for 1h.

For the composition of reactants, the volumetric flow rates of CH₄ and O₂/CO₂ were controlled separately by mass flow controllers (MFCs, AALBORG/Alicat Scientific). After MFCs, those gases were mixed in a spiral tube with a length of about 1.5 m before the reactor to make a homogeneous reactant gas. For the methane steam reforming test, a HPLC pump (M626, Alltech) was used to deliver water into the reactor via a stainless steel tubing (water would transform into steam at high

temperature). In order to fully mix steam with CH₄, counter-current flow was formed about 20cm above the catalyst bed, as shown in Figure 2-7.

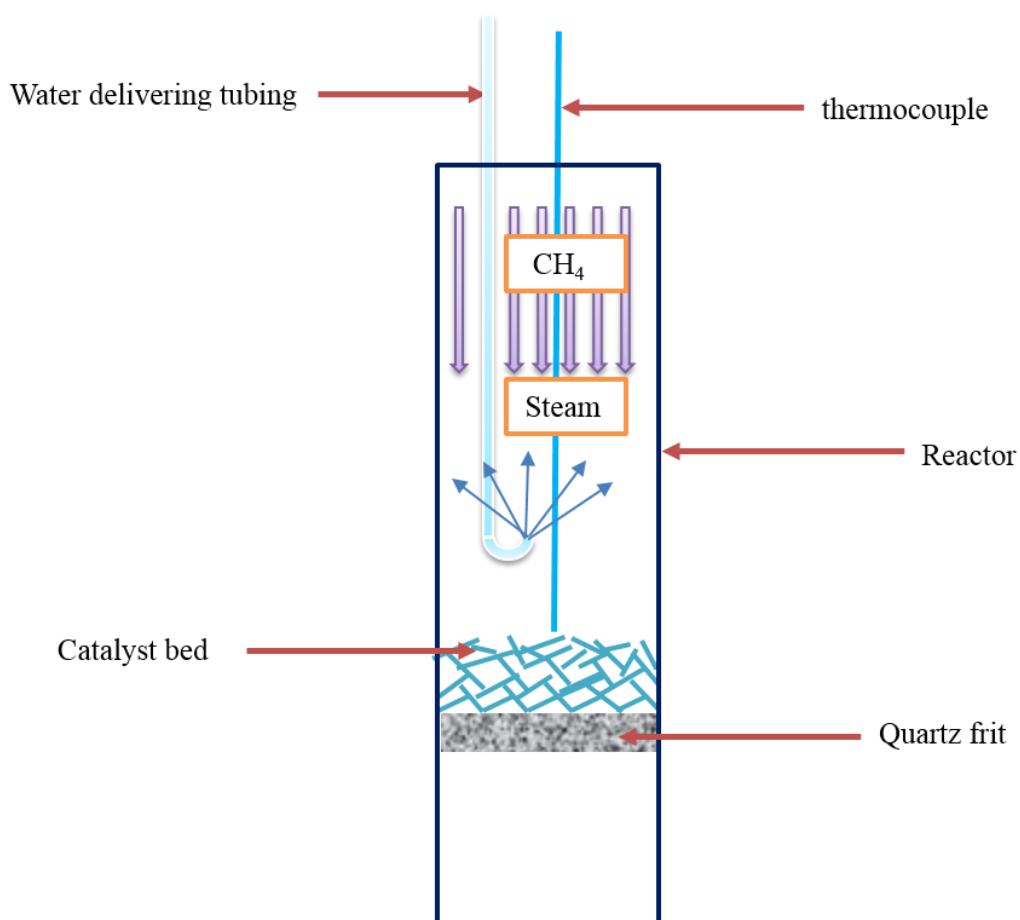


Figure 2-7. Counter-current flow in the reactor for steam methane mixing.

The product gas was collected by sampling bags for the subsequent analysis with a gas chromatography (GC, Agilent 6890).

For safety consideration, several safety precautions were installed in the experiment rig. Before the reactor, there was a release valve, which will be activated when the pressure in reactor increased beyond 40KPa. A cooler and relief valve was set before the sampling outlet, which would not only condense the water in product gas, but also released pressure if the outlet was blocked. Two extraction arms were positioned above the reactor and the outlet to extract any gases that might leak from the reactor.

The detailed information about those reactions can be found in: **3.2.4 & 6.2.3** for dry reforming of methane; **4.2.3** for steam reforming of methane; and **5.2.3** for partial oxidation of methane.

2.3 Quantification of carbon formed in catalyst

Carbon formation over Ni-based catalysts occurs readily during the methane dry/steam reforming, which decreases the catalytic performance by encapsulating the active sites or destroying catalyst structure by lifting catalyst up from support [17]. Studying carbon formation is a basic approach to evaluate reforming catalysts.

The amount of carbon formed over the NiO/CeO₂ fibrous catalysts during the dry reforming of methane was measured via burning the carbon deposited on catalysts, collecting product gas and analyzing the product gas composition by GC. A schematic diagram of the carbon burning rig is shown in Figure 2-8.

The carbon deposited on catalysts was burned in a U-tube reactor that was heated by a furnace in flowing 5% O₂ in N₂. In order to make sure that all carbon could be transformed into CO₂, an excessive amount of oxygen was provided. 0.01-0.04g of the spent catalysts were loaded in a U-type quartz reactor supported by quartz-wool. The volumetric flow of oxidizing gas (5% O₂ in N₂) was controlled by a rotameter. The furnace temperature was programmed by a computer at a ramping rate of 10 °C/min, and temperature in the vicinity of catalysts bed was monitored by a K-type thermocouple (positioned on the top of catalysts bed). The gas coming from the U-tube reactor was collected by a gas bag, and a certain amount of CH₄ was injected into the gas bag as a calibrating gas to test the volume of the collected gas according to CH₄ concentration profile analyzed by GC.

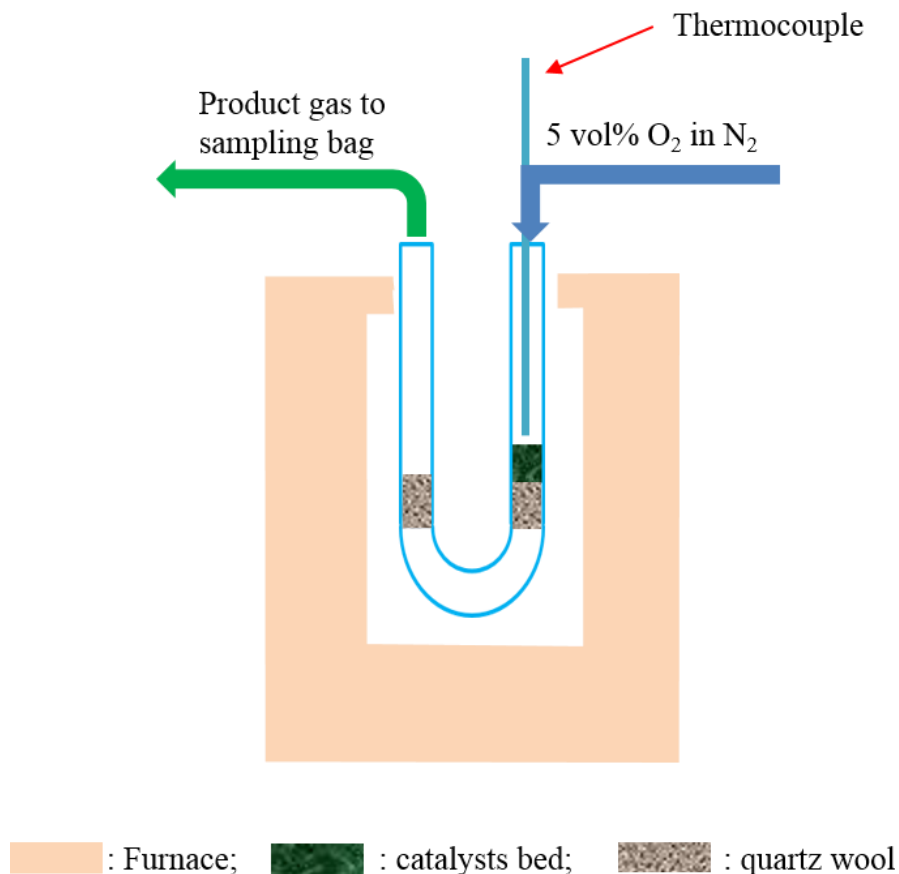


Figure 2-8. The schematic diagram of the carbon burning reactor.

For carbon burning, both CO and CO₂ could be produced, as the occurrence of:



According to the GC results, CO₂ was the only C-containing species in the product gas. The amount of carbon formed on the catalyst was calculated based on the CO₂ amount in the bag.

2.4 References

- [1] I. Yamashita, J. Hayashi, M. Hara, Bio-template synthesis of uniform CdSe nanoparticles using cage-shaped protein, apoferritin, *Chemistry Letters*, 33 (2004) 1158-1159.
- [2] M.R. Weatherspoon, Y. Cai, M. Crne, M. Srinivasarao, K.H. Sandhage, 3D Rutile Titania-Based Structures with Morpho Butterfly Wing Scale Morphologies, *Angewandte Chemie International Edition*, 47 (2008) 7921-7923.
- [3] H. Sieber, Biomimetic synthesis of ceramics and ceramic composites, *Materials Science and Engineering: A*, 412 (2005) 43-47.
- [4] Z. Miao, Z. Liu, B. Han, Y. Wang, Z. Sun, J. Zhang, Synthesis of TiO₂ nanotube networks from the mineralization of swim bladder membrane in supercritical CO₂, *The Journal of supercritical fluids*, 42 (2007) 310-315.
- [5] K. Tanaka, M. Shionoya, Programmable metal assembly on bio-inspired templates, *Coordination Chemistry Reviews*, 251 (2007) 2732-2742.
- [6] D. Yang, L. Qi, J. Ma, Hierarchically ordered networks comprising crystalline ZrO₂ tubes through sol-gel mineralization of eggshell membranes, *Journal of Materials Chemistry*, 13 (2003) 1119-1123.
- [7] D. Dong, X. Shao, Z. Wang, C. Lievens, J. Yao, H. Wang, C.-Z. Li, Fibrous NiO/CeO₂ nanocatalysts for the partial oxidation of methane at microsecond contact times, *RSC Adv.*, 3 (2013) 1341-1345.
- [8] S.-S. Choi, S.G. Lee, S.S. Im, S.H. Kim, Y.L. Joo, Silica nanofibers from electrospinning/sol-gel process, *Journal of Materials Science Letters*, 22 (2003) 891-893.
- [9] Z.-M. Huang, Y.-Z. Zhang, M. Kotaki, S. Ramakrishna, A review on polymer nanofibers by electrospinning and their applications in nanocomposites, *Composites science and technology*, 63 (2003) 2223-2253.

- [10] J.T. McCann, M. Marquez, Y. Xia, Melt coaxial electrospinning: a versatile method for the encapsulation of solid materials and fabrication of phase change nanofibers, *Nano letters*, 6 (2006) 2868-2872.
- [11] D. Li, Y. Xia, Electrospinning of nanofibers: reinventing the wheel?, *Advanced materials*, 16 (2004) 1151-1170.
- [12] A. Greiner, J.H. Wendorff, Electrospinning: a fascinating method for the preparation of ultrathin fibers, *Angewandte Chemie International Edition*, 46 (2007) 5670-5703.
- [13] S. Ramakrishna, K. Fujihara, W.-E. Teo, T.-C. Lim, Z. Ma, An introduction to electrospinning and nanofibers, *World Scientific*, 2005.
- [14] C. Mit-uppatham, M. Nithitanakul, P. Supaphol, Ultrafine electrospun polyamide-6 fibers: effect of solution conditions on morphology and average fiber diameter, *Macromolecular Chemistry and Physics*, 205 (2004) 2327-2338.
- [15] A. Koski, K. Yim, S. Shivkumar, Effect of molecular weight on fibrous PVA produced by electrospinning, *Materials Letters*, 58 (2004) 493-497.
- [16] Y. Shin, M. Hohman, M. Brenner, G. Rutledge, Experimental characterization of electrospinning: the electrically forced jet and instabilities, *Polymer*, 42 (2001) 09955-09967.
- [17] W.J. Lee, C.-Z. Li, Opposite effects of gas flow rate on the rate of formation of carbon during the pyrolysis of ethane and acetylene on a nickel mesh catalyst, *Carbon*, 46 (2008) 1208-1217.

Every reasonable effort has been made to acknowledge the owners of copyright material. I would be pleased to hear from any copyright owner who has been omitted or incorrectly acknowledged.

Chapter 3

A study on carbon formation over fibrous NiO/CeO₂ nanocatalysts during dry reforming of methane

3.1 Introduction

The efficient utilization of energy resources and greenhouse gas utilization have attracted a massive research interests to deal with a carbon-constrained future. Natural gas is one of the important fossil energy resources, and mainly utilized via low efficient combustion such as gas-fired power plants. Methane, the predominant component of natural gas, is also a relatively potent greenhouse gas. Besides natural gas, there is a significant amount of CO₂ in CH₄-riched gas resources such as biogas and coal seam gas. In addition, purified CO₂ can be captured from oxyfuel combustion plants or liquefied natural gas process. The two greenhouse gases can be used as a feedstock for chemical conversion processes for example dry reforming where CH₄ and CO₂ are reformed into syngas (a mixture of H₂ and CO). As an intermediate, the syngas can be converted into valuable liquid fuels and chemicals via the Fischer-Tropsch process [1]. Compared to steam reforming of methane and methane partial oxidation, the dry reforming produces a lower H₂/CO ratio, which favors liquid fuel production such as DME [2].

Although remarkable economic and environmental benefits can be derived from the dry reforming, the catalytic process suffers from catalyst deactivation because of carbon formation and catalyst sintering. Carbon formation can occur during methane dehydrogenation over catalysts or be caused by Boudouard reaction ($2\text{CO} \rightarrow \text{CO}_2 + \text{C}$). It is known that carbon formation is greatly affected by both catalyst and support properties [3]. Though noble metal catalysts have high coking-resistance, Ni catalyst is widely used in methane reforming in consideration of high cost and shortage of noble metal catalysts. However, Ni catalyst has high activity for methane activation, resulting in severe carbon formation. Conventional nanocatalysts are usually supported on porous substrates such as metal oxide powders, and carbon formation is sensitive to support properties [3, 4]. Generally, catalyst supports (e.g. CeO₂) also provide oxygen species to oxidize carbonaceous deposits [5], and the oxygen species are formed through converting the adsorbed CO₂ to CO [6-8]. As a result, the interaction between catalyst and support greatly determines carbon formation [4]. In addition, our previous research showed carbon formation over nickel mesh was greatly affected by radical desorption from catalyst surface, which occurred within

the gas film around mesh wires. Carbon formation could be limited when the gas film was thinned by increasing gas flow rate to facilitate radical desorption [9, 10].

Recently, we have developed a fibrous NiO/CeO₂ nanocatalyst with a hierarchical structure: Interwoven micro-fibres construct a three-dimensional structure, and individual ceramic fibre consists of uniform NiO nanocatalysts supported on CeO₂ scaffold [11]. The catalysts showed high performances in the partial oxidation of methane at microsecond contact times (i.e. high gas flow rates). Though high NiO content (up to 59.2 wt%) was applied, no obvious performance decay was founded during a running period of 12 h, indicating high coking-resistance. However, carbon formation during dry reforming more readily occurs than that during the partial oxidation because of different ways of supplying oxygen species to oxidize carbonaceous deposits. In this study, we will investigate carbon formation over the fibrous catalysts during dry reforming. The effect of catalyst content, crystallization temperature and gas flow rate on carbon formation will be investigated. The high porosity of catalyst bed (above 95%) enabled dry reforming to be operated at high gas flow rates without building up pressure within reactors [11], and therefore it feasible to study the carbon formation affected by gas flow rate. To our knowledge, there are few studies discovering these over supported catalysts.

3.2 Experimental

3.2.1 Catalyst preparation

NiO/CeO₂ catalysts were synthesized using eggshell membrane (ESM) as a template, as described in the previous study [11]. Typically, Ni(NO₃)₂·6H₂O (>99.99 %) and Ce(NO₃)₃·6H₂O (>99.9 %) were dissolved in deionized water to obtain 200 ml 0.5 M metal ion (Ni²⁺ + Ce³⁺) solutions with the Ni²⁺/Ce³⁺ molar ratios of 1:2, 1:1 and 4:1 respectively. The ESM template was derived from commercial chicken eggs. The CaCO₃ shell of eggs was removed by soaking into 1M HNO₃ solution for 5 min, and then the ESM was washed with deionized water, followed by drying in an oven set at 95 °C for 2 h. 2 g of the dried ESM was immersed into each solution at room temperature for 3 h. Then, the ESM-metal composites were dried at 95 °C for 2 h after the removal of surface solution, and subsequently crystallized at 1000 or 1100

°C for 2 h in air. All chemicals were purchased from Sigma Aldrich Australia without further treatment.

3.2.2 Catalyst characterization

The crystalline structure of the templated catalysts was confirmed by using CuK α radiation with a Bruker D8 Advance diffractometer equipped with a LynxEye detector (Bruker-AXS, Karlsruhe, Germany) at a scan rate of 2 °/min and a step size of 0.02°. The composition of the templated catalysts was tested by an induced coupled plasma (ICP, Optima 7300 DV, PerkinElmer) after dissolving the catalysts by the mixture of hydrochloric acid (36 wt%), sulphuric acid (98 wt%) and hydrogen peroxide with the same volume ratio. The microstructures of the catalysts were observed by a microscope (Zeiss Neon 40EsB FIBSEM). To avoid charging on NiO/CeO₂ catalysts, the samples were set on an electron-conductive stick tape, and then coated with 3 nm Pt film. The accelerating voltage applied was 5 KV.

3.2.3 Temperature programmed reduction (TPR)

TPR was performed on ChemBET3000 (Quantachrome Instruments). 0.03g of NiO/CeO₂ catalyst was put into a U-tube with quartz wool as a catalyst holder. The U-tube was purged with nitrogen to remove the air presenting in the lines, and then heated to 250 °C for 30 min in N₂ atmosphere with a flow rate of 40 ml/min in order to remove the moisture and impurities on the sample surface, and then it was cooled to room temperature. The nitrogen was replaced by a gas mixture (5% H₂ in N₂) for the TPR experiments. The catalyst was heated up to 900 °C at the ramp rate of 10 °C /min. The hydrogen consumption by catalyst reductions at certain temperatures was detected by thermal conductivity detector (TCD), and was recorded by a TPRWinTM software.

3.2.4 Dry reforming test

The templated NiO/CeO₂ catalysts were firstly crushed into flakes with the sizes of 1 to 2 mm. Then, 0.15 g of the flake catalyst was put on the quartz filter in the middle of a quartz tube reactor with an inner diameter of 20 mm. The reactor was heated by

a tubular furnace, and the temperature on the surface of catalyst bed was indicated by a K-type thermocouple. The NiO/CeO₂ catalyst was reduced by a mixed gas of 20 vol% H₂/Ar at 750 °C for 1 h, and then a gas mixture of 50Ar: 25CH₄: 25CO₂ (volume) was introduced into the reactor to conduct dry reforming at 750 °C. Gas hourly space velocity (GHSV) was adjusted by mass flow controllers (AALBORG). The GHSV was calculated according to the below formula:

GHSV = Volumetric flow rate of feed gas at room temperature/catalyst real volume.

The component of the exit gas from the reactor was analyzed by a Gas Chromatography (GC, Agilent 6890), and CH₄ conversion was evaluated using the following defined parameters:

$$\text{CH}_4 \text{ conversion} = (\text{CH}_{4, \text{ in}} - \text{CH}_{4, \text{ out}}) / \text{CH}_{4, \text{ in}}$$

3.2.5 Carbon formation test

Thermogravimetric analysis cannot be used for the carbon formation test because the used catalyst can be oxidized during burning off carbon. The U-tube reactor used in TPR was employed to test carbon formation by burning off carbon in furnace with flow of 5% O₂ in N₂. 0.01-0.04g of the tested catalysts was used with varied gas flow rates to convert all carbon into CO₂, which was confirmed by GC results that there was no CO detected. The exit gas from the U-tube reactor was collected and analyzed by GC to quantify CO₂ amount, which was used to calculate carbon formation rate.

3.3 Results and discussion

3.3.1 The effect of NiO content and crystallization temperature

The fibrous catalysts were prepared by the template synthesis utilizing strong metal-protein bond, and metal ions uniformly absorbed within protein fibers of eggshell membranes. After the removal of protein template by heat treatment in air, well-dispersed NiO and CeO₂ nanocrystals compacted into solid fibers [12]. At the crystallization temperature of 900 °C, solid fiber catalyst showed negligible activity

in dry reforming. As crystallization temperature was increased to 1000 °C, the solid fibers were transformed into porous fibers, resulting in the increased surface area. In our experiment, the NiO/CeO₂ catalysts were crystallized at 1000 or 1100 °C for dry reforming.

Figure 3-1 shows the crystallinity of the NiO/CeO₂ catalysts. There are only NiO and CeO₂ crystals and no solid solution is found, which is consistent with the previous study [13]. According to diffraction peak intensities, increasing NiO content from 12.9 wt% to 47.8 wt% decreased CeO₂ crystal size while slightly increased NiO crystal size from 36.5 to and 42.4 nm according to scherrer equation[11]. It was attributed to the dispersion role of CeO₂ in the template synthesis process [6]. Vice versa, NiO also prevented CeO₂ aggregation formation. As the catalyst was crystallized at 1000 °C, which is much higher than that in conventional catalyst preparation, the fibrous catalyst at NiO loading of 47.8 wt% has a smaller BET surface area (4.2 m²/g) and very lower pore volume (0.005 cm³/g) according to nitrogen adsorption-desorption tests [11]. Both NiO and CeO₂ crystal sizes of the 47.8 wt% NiO/CeO₂ catalyst were increased when crystallization temperature was increased from 1000 to 1100 °C.

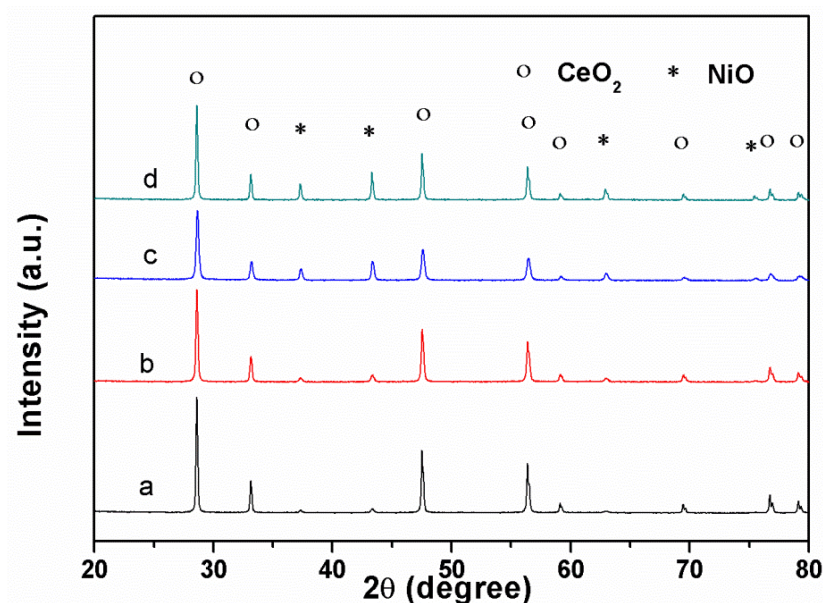


Figure 3-1. XRD patterns of the NiO/CeO₂ catalysts with the NiO contents of (a) 12.9 wt%; (b) 27.7 wt% and (c) 47.8 wt% at a crystallization temperature of 1000 °C and (d) 47.8 wt% at a crystallization temperature of 1100 °C.

In Figure 3-2, scan electron microscopy (SEM) images show a hierarchical structure of the fibrous catalysts. In macroscale, interwoven ceramic fibers construct a three-dimensional structure, formed through the sintering between the templated ceramic fibres during the heat treatment. Compared to conventional powder catalysts, the fibrous catalyst should show higher thermal stability owing to the high sintering resistance of the ceramics with a three-dimensional structure, which is confirmed by the nanostructure retaining at 1000 °C; for individual ceramic fiber, it shows nanoporous structure: NiO nanoparticles supported on CeO₂ scaffold. The hierarchical structure enables high NiO catalyst loadings without causing catalyst aggregation. As NiO content was increased, both fibers itself and the three-dimensional structure became more porous due to the enhanced dispersion role of NiO and the reduction of NiO that would form more voids as a result of the removal of O and the shrink of the Ni particle. Increasing crystallization temperature to 1100 °C densified the porous structure via ceramic sintering and caused fiber fracture.

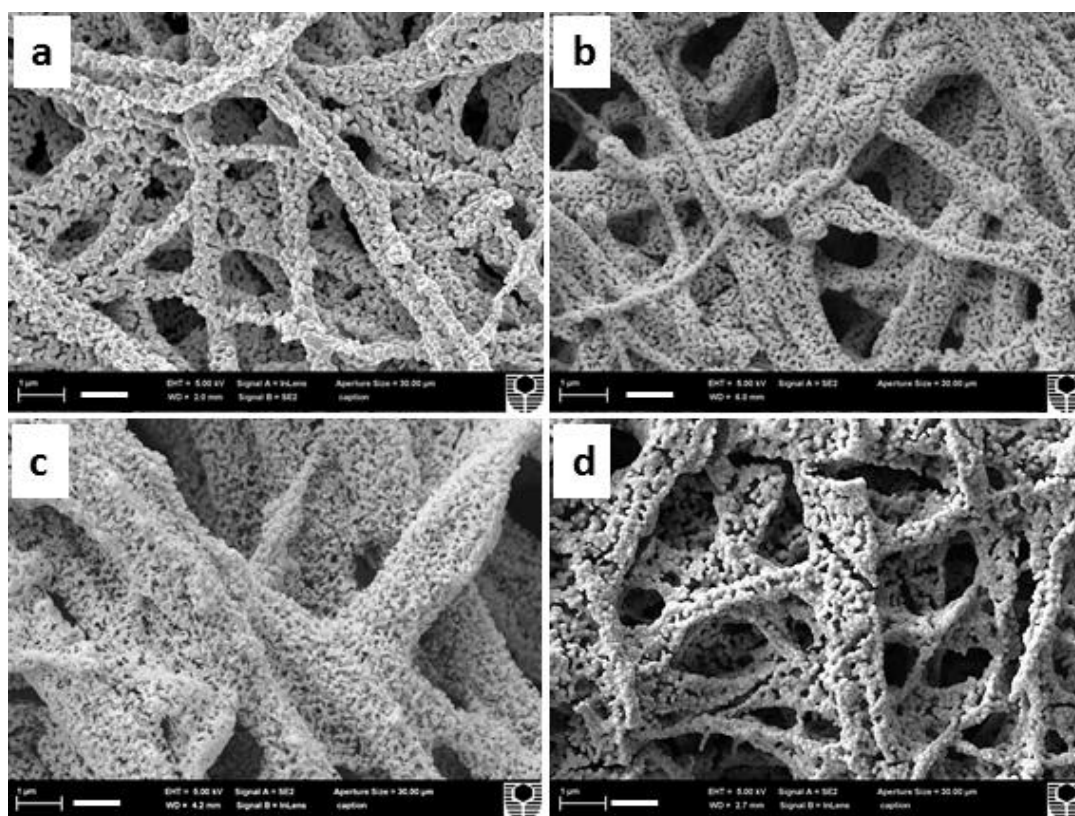


Figure 3-2. SEM images of the NiO/CeO₂ catalysts with the NiO contents of (a) 12.9 wt%; (b) 27.7 wt% and (c) 47.8 wt% at the crystallization temperature of 1000 °C and (d) 47.8 wt% at the crystallization temperature of 1100 °C. The scale bar is 1 μm.

TPR was conducted to investigate catalyst reduction behaviour and in turn the interaction between NiO catalyst and CeO₂ support. In general, the reductions of NiO and CeO₂ occur at around 400 and 800 °C, respectively [13, 14]. However, there is another peak between 400 and 600 °C presenting in all fibrous catalysts in Figure 3-3, which is close to NiO reduction peak and therefore expected to be related to NiO reduction. The reduction of NiO causes hydrogen species spill over, and then induces CeO₂ support reduction [6, 13, 15]. Hence, the interaction between NiO and CeO₂ plays an important role in the reduction. In other words, TPR curves can indicate the interaction. For the 12.9 wt% NiO/CeO₂ catalyst with a less porous structure, all NiO particles were supported on CeO₂ support or even partially covered by CeO₂, and the strong interaction between NiO and CeO₂ support resulted in the simultaneous reduction of NiO and CeO₂ at temperatures between 400 and 600 °C. As a result, there was no NiO reduction peak. As NiO content was increased, a high peak representing NiO reduction at about 400 °C appeared while the NiO-CeO₂ reduction at 400-600 °C was diminished. It is because more NiO particles stuck out from CeO₂ support at high NiO contents, leading to the weak interaction with CeO₂ support. For the 47.8 wt% NiO/CeO₂ catalyst, the increase of crystallization temperature from 1000 to 1100 °C led to an enhanced peak at 400-600 °C because high-temperature sintering strengthened the NiO-CeO₂ interaction, which is in accordance to SEM images in Figure 3-2. From CeO₂ reduction at around 800 °C, the reduction peak shifted to high temperature as CeO₂ particle size increased because large particles required a long time to complete reduction.

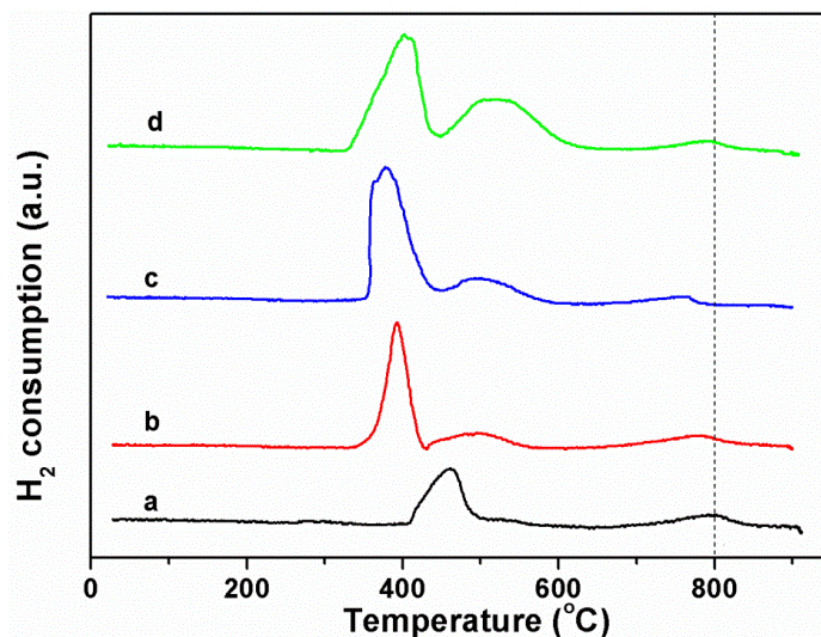


Figure 3-3. TPR profiles of the NiO/CeO₂ catalysts with the NiO contents of (a) 12.9 wt%; (b) 27.7 wt% and (c) 47.8 wt% at a crystallization temperature of 1000 °C and (d) 47.8 wt% at a crystallization temperature of 1100 °C.

Dry reforming was performed over the fibrous catalysts at 750 °C with a GHSV of $2.7 \times 10^5 \text{ h}^{-1}$. From reforming performances shown in Figure 3-4, CH₄ conversion experienced increase at initial several hours and then decreased, and a similar result was reported on the supported powder catalyst [16]. It is because that the generation of carbon nanofibres increase the accessible surface area of Ni particles *via* lifting it off from supports, as explained below. There was a significant conversion decrease for the 47.8% NiO/CeO₂ catalyst within an operation time of 10 h, and the performance decay was diminished over the catalyst with low NiO contents. Interestingly, the 47.8 wt% NiO/CeO₂ catalyst sintered at 1100 °C produced a higher CH₄ conversion than that sintered at 1000 °C though catalyst surface area, an important property of catalyst, was decreased at the higher crystallization temperature. Moreover, no performance decay was found over the catalyst sintered at 1100 °C, which has a strong NiO-CeO₂ interaction indicated by TPR results. Therefore, the interaction plays a more important role in the catalytic reaction than catalyst surface area. The reforming performance decay is related to catalyst deactivation caused by catalyst sintering and/or carbon formation. Conventional supported catalysts are prepared at low temperatures to obtain small catalyst particles

with high surface area, and catalytic reaction at high temperatures may cause catalyst and/or catalyst support sintering. The fibrous NiO/CeO₂ catalysts in this study were prepared at 1000 or 1100°C, which is much higher than the operating temperature (750 °C). Thereby, the catalyst deactivation should be mainly caused by carbon formation.

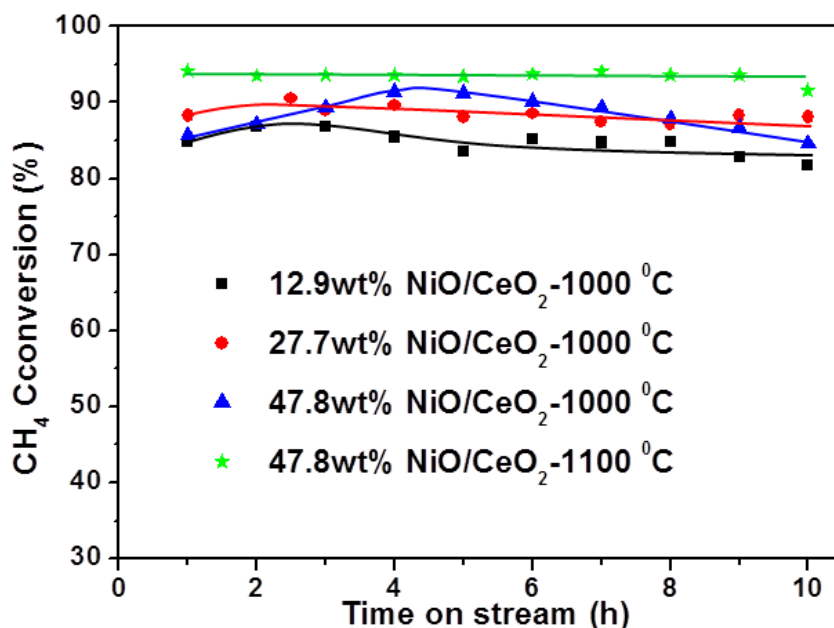


Figure 3-4. CH₄ conversion decay during dry reforming for 10 h over the NiO/CeO₂ catalysts with different NiO contents at different crystallization temperatures.

Carbon formation over the fibrous catalyst was tested after dry reforming for 10 h. As shown in Figure 3-5, carbon formation rate increased with NiO content including a sharp increase at NiO contents above 27.8 wt%. It can be explained by XRD and TPR results. The increased NiO particles size can cause carbon formation. Nevertheless, the high carbon formation rate should be mainly attributed to the weak interaction between NiO catalyst and CeO₂ support at high NiO contents. For the 47.8 wt% NiO/CeO₂ catalyst, increasing catalyst crystallization temperature from 1000 to 1100 °C decreased carbon formation rate though NiO particle size was increased. Therefore, the interaction between NiO catalyst and CeO₂ support greatly determines carbon formation over the fibrous catalysts during dry reforming.

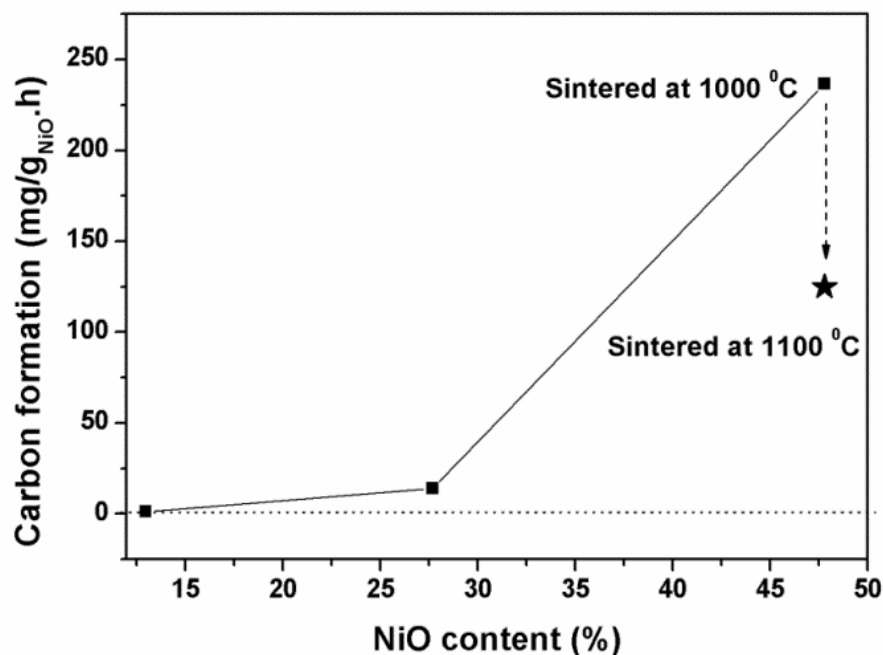


Figure 3-5. The effect of NiO content and crystallization temperature of the NiO/CeO₂ catalysts on carbon formation rate.

3.3.2 The effect of gas flow rate

It is believed that methane is activated over catalyst surface, and the formed radicals desorb from catalyst surface or is further dehydrogenated to form carbonaceous deposits. Failing to oxidize the carbonaceous deposits will form carbon on catalyst surface (carbon formation). Consequently, the success of radical desorption also affects coke formation. Increasing the rate of gas flow passing through catalyst bed could reduce the thickness of gas film or boundary layer around catalysts and therefore facilitate radical desorption from catalyst surface [9]. There are few studies reporting the effect of gas flow rate on carbon formation during dry reforming over supported catalysts. It is because conventional powder catalysts have small particles sizes, and catalytic reactions are operated at low gas flow rates to avoid pressure drop in reactors. Highly porous catalyst in this study enables dry reforming to be operated at high gas flow rates without causing safety issue. As shown in Figure 3-6, GHSV (i.e. gas flow rate) greatly affects carbon formation rate, which drastically decreases as GHSV is increased. At the GHSVs above $4.1 \times 10^6 \text{ h}^{-1}$, there is a very low carbon formation rate. There are two possible reasons causing the decreased coke formation rates at high gas flow rates. Mass transfer at high gas flow rates was improved, which

facilitated radical desorption; the rate of carbon formation caused by dehydrogenation and Boudouard reaction was decreased due to low methane conversions at high gas flow rates.

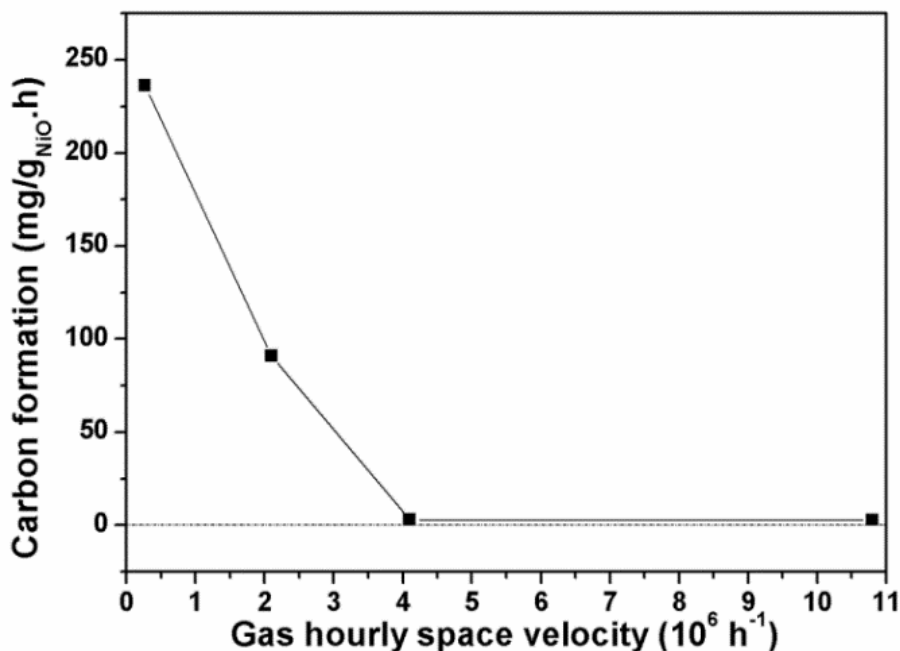


Figure 3-6. The effect of gas flow rate on carbon formation rate over the 47.8 wt% NiO/CeO₂ catalyst.

Figure 3-7 shows SEM images of catalysts after dry reforming for 10 h at different GHSVs. At low GHSVs such as 2.7×10^5 and $2.1 \times 10^6 \text{ h}^{-1}$, a large amount of carbon nanofibers was formed. The diameter of the carbon nanofibers was reduced as the GHSV was increased because carbon formation rate determines the carbon fiber diameter [17]. Moreover, the growth of carbon nanofibers destroyed the fibrous structure of catalyst. The reason for the catalyst destruction is related to the formation mechanism of carbon fibers. Carbon diffuses through the Ni particles and precipitates on the rear side of the Ni particles where carbon fibers grow, and consequently the Ni particles are lifted from supports by carbon fibers, as evidenced by the Ni particle seating at the tip of a carbon fiber in Figure 3-8 [18]. As a small amount of carbon was formed at high GHSVs of $4.1 \times 10^6 \text{ h}^{-1}$ and $1.1 \times 10^7 \text{ h}^{-1}$ according to low carbon formation rates, the catalyst microstructure was retained after test, and no carbon nanofiber was observed. There might be amorphous carbon covering catalyst surface, which cannot be observed by SEM.

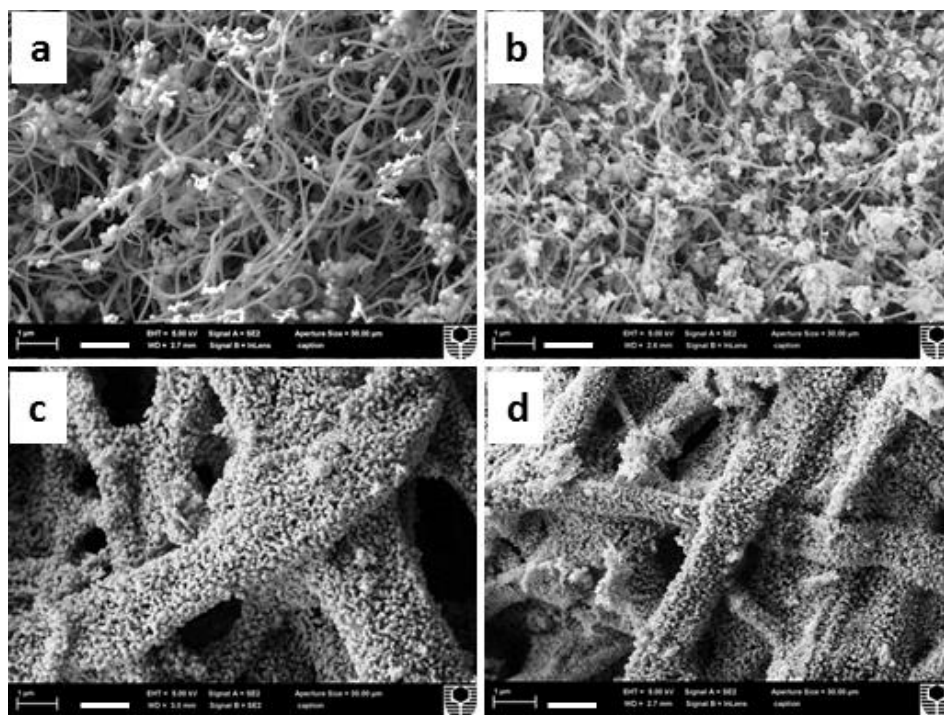


Figure 3-7. SEM images of the 47.8 wt% NiO/CeO₂ catalysts after dry reforming at different GHSVs: a, $2.7 \times 10^5 \text{ h}^{-1}$; b, $2.1 \times 10^6 \text{ h}^{-1}$; c, $4.1 \times 10^6 \text{ h}^{-1}$ and d, $1.1 \times 10^7 \text{ h}^{-1}$. The scale bar is 1 μm .

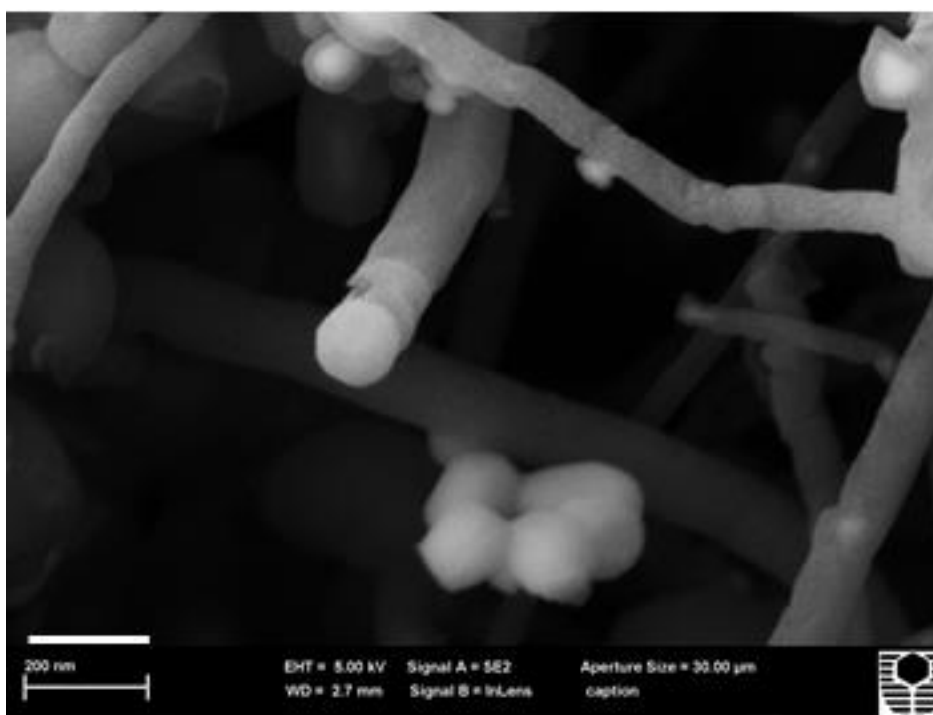


Figure 3-8. SEM image of Ni particle at the tip of carbon nanofiber after dry reforming. The scale bar is 200 nm.

Catalytic reaction rates changing with operating time are shown in Figure 3-9. As the GHSV was increased, the reaction rate was increased. It indicates the reaction is controlled by external mass transfer, and increasing gas flow rate improved the mass transfer through reducing the thickness of gas film or boundary layer [19]. Carbon formation has different effects on the reaction rate at different GHSVs. At low GHSVs, the generation of carbon nanofibers initially increases the accessible Ni surface area and therefore reaction rate. However, carbon nanofibers finally destroy catalyst structure and decrease the reaction rate as reforming continues. In contrast, a small amount of amorphous carbon formed at low GHSVs causes the initial decrease of reaction rate, and it then becomes stable.

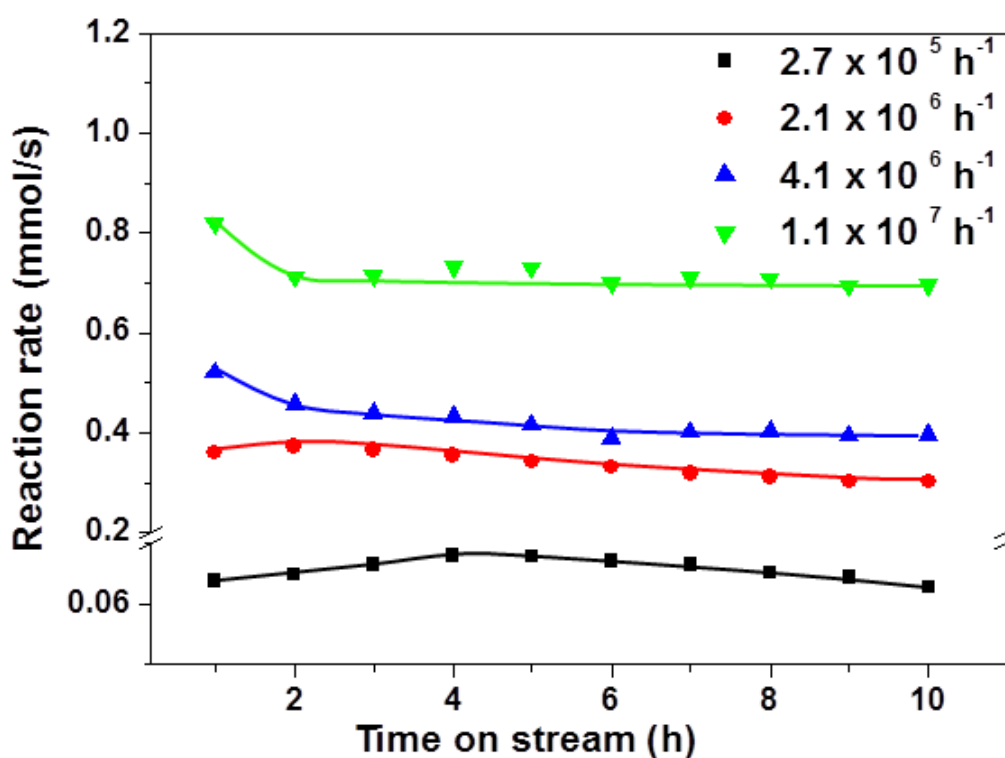


Figure 3-9. Reaction rate change with time on stream during dry reforming over the 47.8 wt% NiO/CeO₂ catalyst for 10 h at different GHSVs.

3.4 Conclusion

Coke formation over fibrous NiO/CeO₂ catalysts has been studied as functions of NiO content, crystallization temperature and gas flow rate. The effect of NiO content and crystallization temperature can be attributed to its influence on the interaction

between NiO catalyst and CeO₂ support, which was reflected by NiO reduction behaviors in TPR profiles. The stronger interaction resulted in higher coking-resistance. Also, increasing gas flow rate could reduce coke formation rate through facilitating radical desorption and/or due to low methane conversions. The results would be valuable in the design of coking-resistant catalysts and stable catalytic reaction processes.

3.5 References

- [1] A. Jess, R. Popp, K. Hedden, Production of diesel oil and wax by Fischer-Tropsch-synthesis using a nitrogen-rich synthesis gas - Investigations on a semi-technical scale, *Oil Gas-Eur. Mag.*, 24 (1998) 34-43.
- [2] J.H. Flores, D.P.B. Peixoto, L.G. Appel, R.R. de Avillez, M.I.P. da Silva, The influence of different methanol synthesis catalysts on direct synthesis of DME from syngas, *Catal. Today*, 172 (2011) 218-225.
- [3] Y.H. Hu, E. Ruckenstein, Catalytic conversion of methane to synthesis gas by partial oxidation and CO₂ reforming, *Advances in Catalysis*, Vol 48, 48 (2004) 297-345.
- [4] M.C.J. Bradford, M.A. Vannice, CO₂ reforming of CH₄ over supported Pt catalysts, *J. Catal.*, 173 (1998) 157-171.
- [5] R.J. Gorte, Ceria in Catalysis: From Automotive Applications to the Water Gas Shift Reaction, *Aiche J.*, 56 (2010) 1126-1135.
- [6] A. Kambolis, H. Matralis, A. Trovarelli, C. Papadopoulou, Ni/CeO₂-ZrO₂ catalysts for the dry reforming of methane, *Appl. Catal. A-Gen.*, 377 (2010) 16-26.
- [7] P. Kumar, Y. Sun, R.O. Idem, Nickel-based ceria, zirconia, and ceria-zirconia catalytic systems for low-temperature carbon dioxide reforming of methane, *Energy Fuels*, 21 (2007) 3113-3123.
- [8] S.B. Wang, G.Q. Lu, Role of CeO₂ in Ni/CeO₂-Al₂O₃ catalysts for carbon dioxide reforming of methane, *Appl. Catal. B-Environ.*, 19 (1998) 267-277.
- [9] W.J. Lee, C.Z. Li, Coke formation and reaction pathways of catalyst-surface-generated radicals during the pyrolysis of ethane using Ni mesh catalyst, *Appl. Catal. A-Gen.*, 316 (2007) 90-99.

- [10] E.B.H. Quah, C.Z. Li, Roles of desorbed radicals and reaction products during the oxidation of methane using a nickel mesh catalyst, *Appl. Catal. A-Gen.*, 258 (2004) 63-71.
- [11] D.H. Dong, X. Shao, Z.T. Wang, C. Lievens, J.F. Yao, H.T. Wang, C.Z. Li, Fibrous NiO/CeO₂ nanocatalysts for the partial oxidation of methane at microsecond contact times, *RSC Adv.*, 3 (2013) 1341-1345.
- [12] D.H. Dong, Y.Z. Wu, X.Y. Zhang, J.F. Yao, Y. Huang, D. Li, C.Z. Li, H.T. Wang, Eggshell membrane-templated synthesis of highly crystalline perovskite ceramics for solid oxide fuel cells, *J. Mater. Chem.*, 21 (2011) 1028-1032.
- [13] V.M. Gonzalez-Delacruz, F. Ternero, R. Pereniguez, A. Caballero, J.P. Holgado, Study of nanostructured Ni/CeO₂ catalysts prepared by combustion synthesis in dry reforming of methane, *Appl. Catal. A-Gen.*, 384 (2010) 1-9.
- [14] W.J. Shan, M. Fleys, F. Lopicque, D. Swierczynski, A. Kiennemann, Y. Simon, P.M. Marquaire, Syngas production from partial oxidation of methane over Ce_{1-x}Ni_xO_y catalysts prepared by complexation-combustion method, *Appl. Catal. A-Gen.*, 311 (2006) 24-33.
- [15] W.S. Dong, H.S. Roh, K.W. Jun, S.E. Park, Y.S. Oh, Methane reforming over Ni/Ce-ZrO₂ catalysts: effect of nickel content, *Appl. Catal. A-Gen.*, 226 (2002) 63-72.
- [16] X.E. Verykios, Catalytic dry reforming of natural gas for the production of chemicals and hydrogen, *Int. J. Hydrog. Energy*, 28 (2003) 1045-1063.
- [17] W.J. Lee, C.Z. Li, Opposite effects of gas flow rate on the rate of formation of carbon during the pyrolysis of ethane and acetylene on a nickel mesh catalyst, *Carbon*, 46 (2008) 1208-1217.
- [18] K.O. Christensen, D. Chen, R. Lodeng, A. Holmen, Effect of supports and Ni crystal size on carbon formation and sintering during steam methane reforming, *Appl. Catal. A-Gen.*, 314 (2006) 9-22.

[19] D.A. Hickman, L.D. Schmidt, Synthesis Gas-Formation by Direct Oxidation of Methane over Pt Monoliths, *J. Catal.*, 138 (1992) 267-282.

Every reasonable effort has been made to acknowledge the owners of copyright materials. I would be pleased to hear from any copyright owner who has been omitted or incorrectly acknowledged.

Chapter 4

Hierarchically structured NiO/CeO₂ nanocatalysts templated by eggshell membranes for methane steam reforming

4.1 Introduction

Of all fossil fuels, natural gas is relatively clean in terms of the emission of greenhouse gases and other pollutants. Unfortunately, abundant reserves of natural gas are located in remote areas. Natural gas cannot be transported efficiently to highly populated regions where there are high energy demands. The efficient conversion of these stranded natural gas resources into easily transportable liquid fuels and chemicals is therefore of great social, economic and environmental significance [1]. Natural gas reforming is the first step in the conversion of natural gas into valuable liquid fuels and chemicals. Once methane, the dominant component of natural gas, is reformed into syngas (a mixture of H_2 and CO), a variety of liquid fuels and chemicals can be synthesized, for example via the Fischer–Tropsch process [2].

Catalysts play an important role in methane reforming. Stable methane molecules are activated on the catalyst surface to form radicals, which are then oxidized into CO or CO_2 by oxygen species derived from oxidants such as O_2 , CO_2 or steam [3]. Noble metal catalysts such as Pt and Pd have high catalytic activity and coking-resistance, while high prices and low availability limit their practical applications [4]. Transition metals such as Ni and Fe are considered to be good alternatives for noble metal catalysts. However, Fe catalyst has low catalytic activity and Ni catalyst readily causes coke formation due to its high catalytic activity in methane activation [5]. The coke formation can be restrained by reducing the Ni particle size and enhancing the interaction between catalyst and support [6, 7]. Therefore, the catalyst/support structure (or morphology) greatly affects the reforming performance.

The catalyst/support structure is mainly determined by the catalyst preparation methods. Supported catalysts are generally prepared by either wet-impregnation or one-pot synthesis. Wet-impregnation has been widely used to prepare catalysts for industrial applications because of the high thermal stability of the supports and high efficiency of catalyst utilization [8]. Catalysts, noble metals or transition metals, are impregnated into porous supports such as ceramic monoliths and ceramic powders [8, 9]. Nevertheless, supports occupy the major volume of catalyst beds in reactors, and catalyst loadings are restricted by catalyst aggregation. The one-pot synthesis of

catalyst and support is mainly used in laboratories to investigate catalyst activity, including sol-gel, combustion and homogeneous precipitation processes [10-12]. High loadings of catalysts can be readily achieved by adjusting the composition of the catalyst precursors. However, catalyst sintering during the reforming at 700-900 °C incurs the decay of reforming performances because catalysts are normally calcined at low temperatures (below 700 °C) to retain high the surface areas of catalysts [10].

Template synthesis is an effective way to control material structure through selecting suitable templates [13, 14]. Green and easily available eggshell membranes are constructed of interwoven protein fibres. Utilizing the strong bonding between metal ions and proteins, we have templated three-dimensional catalytic ceramics as cathodes of solid oxide fuel cells [15, 16], and the three-dimensional structure ensured high thermal stability owing to a high resistance to sintering. Recently, we used the method to prepare fibrous NiO/CeO₂ nanocatalysts [17]. High catalyst loadings (up to 59.2%) were achieved, while no obvious aggregation of nanocatalysts was found after being heated at 1000 °C, which is higher than the temperatures of methane reforming. As a result, high syngas yields were obtained during the partial oxidation of methane at microsecond contact times. We also found that the interaction between catalyst and support greatly affected carbon formation during dry reforming of methane [18]. In this study, as a recently-developed method, the preparation parameters such as immersion time and calcination temperature will be investigated as factors influencing catalyst structure and in turn performance in steam reforming of methane.

4.2 Experimental

4.2.1 Catalyst preparation

As described in our previous study [17], eggshell membrane (ESM) was used as a template to prepare catalysts. Typically, Ni(NO₃)₂·6H₂O (>99.99%) and Ce(NO₃)₃·6H₂O (>99.9%) were dissolved in deionized water to obtain 0.5 M metal ion (Ni²⁺ + Ce³⁺) solutions with the Ni²⁺/Ce³⁺ molar ratio of 4:1. The eggshell derived from commercial eggs was immersed into 1 M nitric acid solution for 5-10 min, followed by peeling protein membrane from CaCO₃ shell. Then, the ESM was

washed with deionized water to remove egg white, and subsequently dried in oven at 95 °C for 2 h. Next, the fibrous catalyst was prepared by one step template process. 1 g of the dried ESM was immersed into 100 ml of the above nitrate solution at room temperature for 1, 3, 5 and 9 h respectively, where the adsorption of metal ions within protein fibers occurred. After taking the ESM from the solution, the excessive solution on the ESM surface was removed by rinsing with deionized water. Finally, the ESM with adsorbed catalyst precursors was dried at 95 °C for 2 h, and then calcined at 900, 950, 1000 and 1050 °C for 2 h in air respectively to remove protein fibres and crystallize catalysts. All chemicals were purchased from Sigma Aldrich Australia, and used without further treatment.

4.2.2 Catalyst characterization

Thermogravimetric analysis (TGA) of the ESM-metal composites was conducted on a thermogravimetric analyzer (Q5000, TA instruments). The microstructures of the catalysts were observed by a scanning electron microscope (Zeiss Neon 40EsB FIBSEM). X-Ray diffraction patterns of catalysts were tested by using CuK α radiation with a Bruker D8 Advance diffractometer equipped with a LynxEye detector (Bruker-AXS, Karlsruhe, Germany) at a scan rate of 2 °/min and a step size of 0.02°. Temperature-programmed reduction (TPR) was performed on a ChemBET3000 machine (Quantachrome Instruments). 0.03g of NiO/CeO₂ catalyst was put into a U-tube and held by quartz wool. The U-tube was purged with nitrogen to expel the air in the lines, and then heated to 250 °C for 30 min in N₂ atmosphere with a flow rate of 40 ml/min in order to remove the moisture and impurities on the catalyst surface. After that, it was cooled to room temperature. Next, a gas mixture (5% H₂ in N₂) replaced the nitrogen to conduct TPR. The catalyst was heated up to 900 °C at a ramp rate of 10 °C /min. The H₂ consumption by the catalyst reduction as a function of temperature was detected by thermal conductivity detector (TCD), and the data were analysed by a TPRWinTM software.

4.2.3 Steam reforming test

The templated NiO/CeO₂ catalysts were firstly crushed into flakes with the sizes of 1 to 2 mm. Then, 0.04 g of the flake catalyst was put on a quartz filter that was set in

the middle of a quartz tube reactor with an inner diameter of 10 mm. The reactor was heated by a tubular furnace, and the temperature on the surface of the catalyst bed was measured by a K-type thermocouple. The NiO/CeO₂ catalyst was reduced by a mixed gas of 20 vol% H₂/Ar at 750 °C for 1 h, and then a gas mixture of 40Ar:20CH₄: 40H₂O (volume) was introduced into the reactor to conduct steam reforming at 800 °C. The gas flow rate was adjusted by mass flow controllers (AALBORG). Steam was fed by an HPLC pump (M626, AllTech) through a pre-heating tube. The exit gas from the reactor was ventilated to air through extraction. The components of the exit gas from the reactor were analysed by Gas Chromatography (GC, Agilent 6890). According to gas volume and CH₄ concentration, CH₄ conversion was calculated as follow:

$$\text{CH}_4 \text{ conversion} = (\text{CH}_{4, \text{ in}} - \text{CH}_{4, \text{ out}}) / \text{CH}_{4, \text{ in}}$$

4.3 Results and discussion

4.3.1 Hierarchically structured NiO/CeO₂ nanocatalyst

Eggshell membrane (ESM) exhibits a structure of interwoven protein fibres, as shown in Figure 4-1a, and the structure has been duplicated by several ceramics prepared using the ESM template [19-21]. The strong bonding between metal ions and protein ensures high template efficiency. We firstly used the method to prepare highly stable catalysts for methane reforming [17]. The fibrous structure of NiO/CeO₂ catalyst is shown in Fig1b, and the diameters of the fibres are 1-5 μm, and smaller than those of the protein fibre template. The strong interconnection among the ceramic fibres has been formed by sintering during catalyst calcination, resulting in a three-dimensional structure. The structure has shown higher thermal stability compared to conventional power catalysts because of a higher resistance to sintering [17].



Figure 4-1. SEM images of template and the hierarchical structure of templated nanocatalyst: ESM template (a), ESM-templated NiO/CeO₂ nanocatalyst (b) and nanoporous catalyst fibre (c).

Moreover, each individual fibre has a nonporous structure (Figure 4-1c). Large CeO₂ particles (about 200 nm) construct a scaffold for supporting NiO nanoparticles (about 50 nm). Therefore, a hierarchically structured NiO/CeO₂ nanocatalyst has been successfully prepared by using the ESM template.

4.3.2 The effect of immersion time

The NiO/CeO₂ nanocatalyst is templated by simply immersing ESM into catalyst precursors (nitrate solution) without requiring the other chemicals that are used in conventional catalyst preparation [12]. The effect of immersion time on catalyst microstructure is investigated by immersing for 1, 3, 5 and 9 h respectively. After calcination at 1000 °C, the structures of the prepared catalysts are compared in Figure 4-2. For an immersion time of 1 h, the fibrous structure of the templated ceramic is not obvious, and it comprises larger fibers than other catalysts prepared at longer immersion times. According to the TGA results of ESM-metal composites in Figure 4-3, the ESM-metal composite prepared at the immersion time of 1 h produced the smallest amount of catalyst while other samples templated the similar amount of ceramic. Therefore, it took about 3 h to reach the saturated adsorption of metal ions within ESM in this study. The low template efficiency at the immersion time of 1 h restrained ceramic particle sintering and formed large and broken fibers. As the immersion time was increased to 3 h, the ceramic fibers became thin and robust, and showed uniform porous structure. With further increasing immersion time to 5 and 9 h, the nanoporous fiber structure became inhomogeneous, which led to fibers broken during cooling down. This might be attributed to the rearrangement of metal ions within the protein fibers through the exchange of functional groups during the long time immersion. Therefore, the catalyst prepared with the immersion time of 3 h was chosen for the following study.

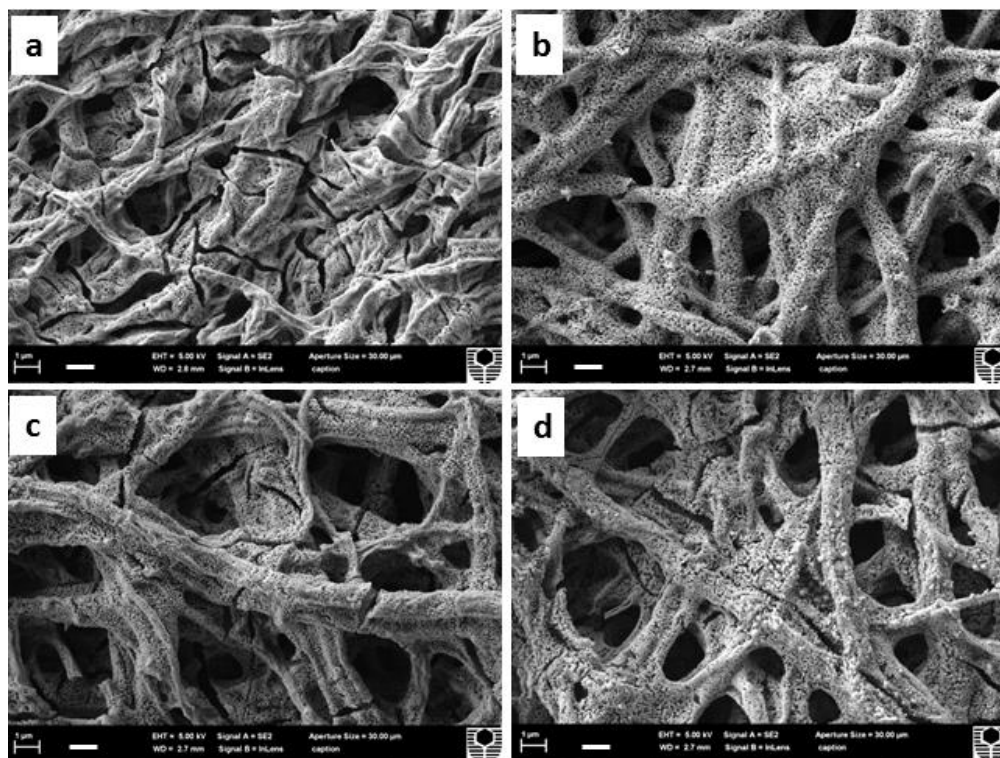


Figure 4-2. Comparison of NiO/CeO₂ nanocatalysts prepared with different immersion times: a, 1 h; b, 3 h; c, 5 h; d, 9h. Scale bar is 1 μm.

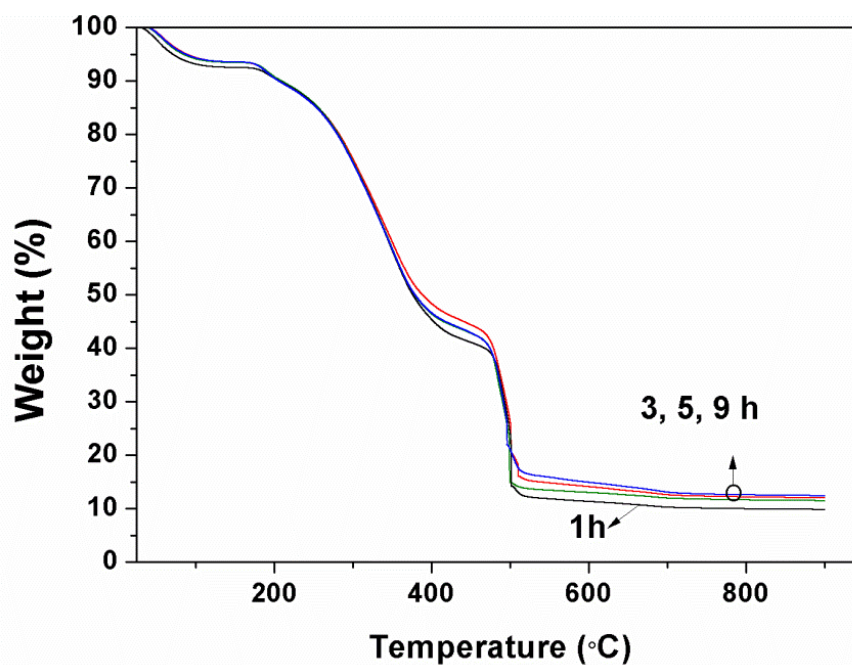


Figure 4-3. TGA profiles of the ESM-metal composites prepared at different immersion times.

4.3.3 The formation of nanoporous structure

From the TGA results, NO_3^- is decomposed before 400 °C, and the ESM template is burned off at about 500 °C [15]. To investigate the formation of the nanoporous structure of catalyst fibres, the catalyst precursor was calcined at 500, 700, 800 and 900 °C respectively. Figure 4-4 shows cross sections of the catalyst fibres. Calcined at 500 °C, catalyst fibres have a dense structure packing with newly-formed fine metal oxide crystals. As the calcination temperature was increased, the sintering of the ceramic particles resulted in a more porous structure constructed by larger particles. In addition, ceramic particle sizes became non-uniform because NiO and CeO_2 have different sinterabilities. Easily-sintering CeO_2 particles constructed a scaffold for supporting small NiO particles, as shown in Fig 1c. Nevertheless, ceramic particle sizes are retained within 100 nm after the calcination at 900 °C, which is much higher than the calcination temperatures in conventional catalyst preparation and generally higher than the operation temperatures of methane reforming. This is attributed to the template process. Metal ions were uniformly absorbed within the protein fibres of ESM during immersion and then transformed into oxide particles during calcination. The aggregation of the nanoparticles was restrained during the high temperature calcination because the location of the nanoparticles is set by the three-dimensional structure and the nanoparticles cannot move easily to promote sintering, unlike the case for powder catalysts.

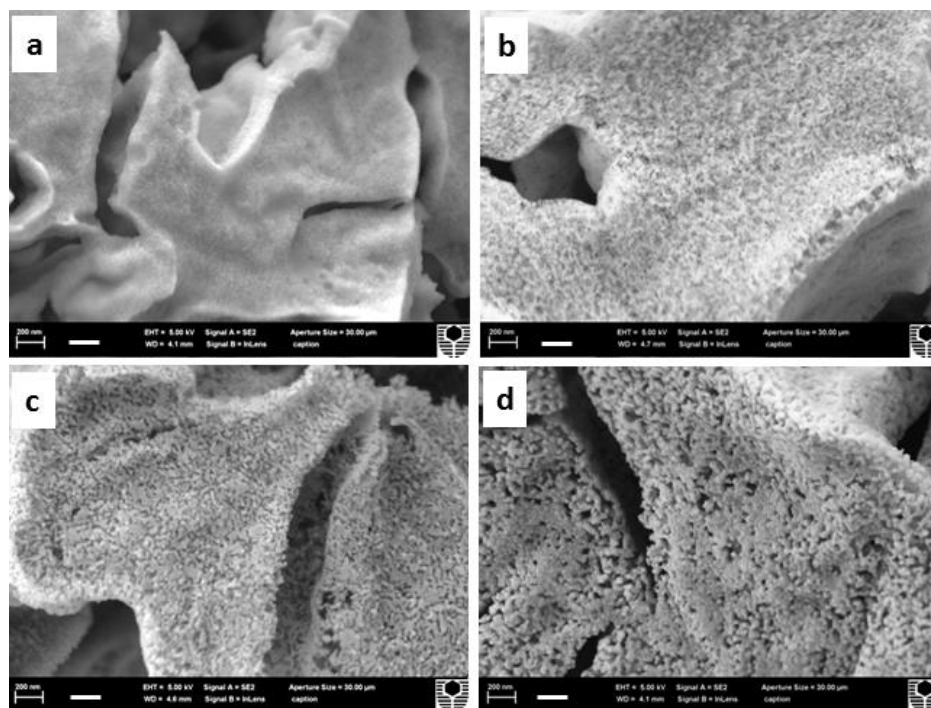


Figure 4-4. SEM images of the cross sections of the ceramic fibres calcined at different temperatures: a, 500; b, 700; c, 800 and d, 900 °C. Scale bar is 200 nm.

4.3.4 The effect of catalyst calcination temperature

Calcination temperature determines the catalyst microstructure and in turn influences methane reforming performances. As shown in Figure 4-5, the catalyst calcined at 900 °C had a less porous structure, and it produced low methane conversion in dry reforming of methane [18]. This might be the result of high mass transfer resistance within the porous catalyst fibres. As the calcination temperature increased to 950 °C and 1000 °C, the catalyst fibres became more porous and showed the increased particle sizes. However, at the calcination temperature of 1050 °C, the nanoporous structure collapsed due to the severe sintering of the CeO₂ support. According to the Scherrer Equation, XRD diffraction peaks in Figure 4-6 indicate that the NiO crystal sizes are 32, 38, 43 and 54 nm for the catalysts calcined at 900, 950, 1000 and 1050 °C, respectively. Therefore, there was a slight increase in crystal size as the calcination temperature was increased, which is consistent with the results shown in the SEM images. The high calcination temperatures produced highly crystallized catalysts with lower BET surface areas and pore volumes compared with

conventional catalysts (e.g. a $4.2 \text{ m}^2/\text{g}$ of BET and a $0.005 \text{ cm}^3/\text{g}$ of pore volume for the templated catalyst calcined at $1000 \text{ }^\circ\text{C}$) [17].

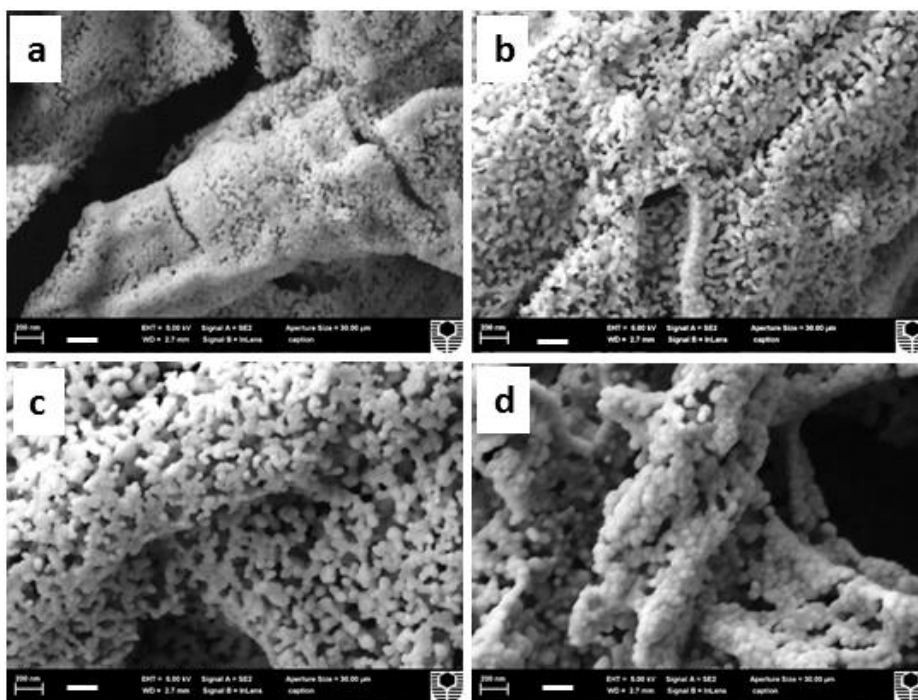


Figure 4-5. SEM images of the catalysts calcined at different temperatures: a, 900 °C; b, 950 °C; c, 1000 °C and d, 1050 °C. Scale bar is 200 nm.

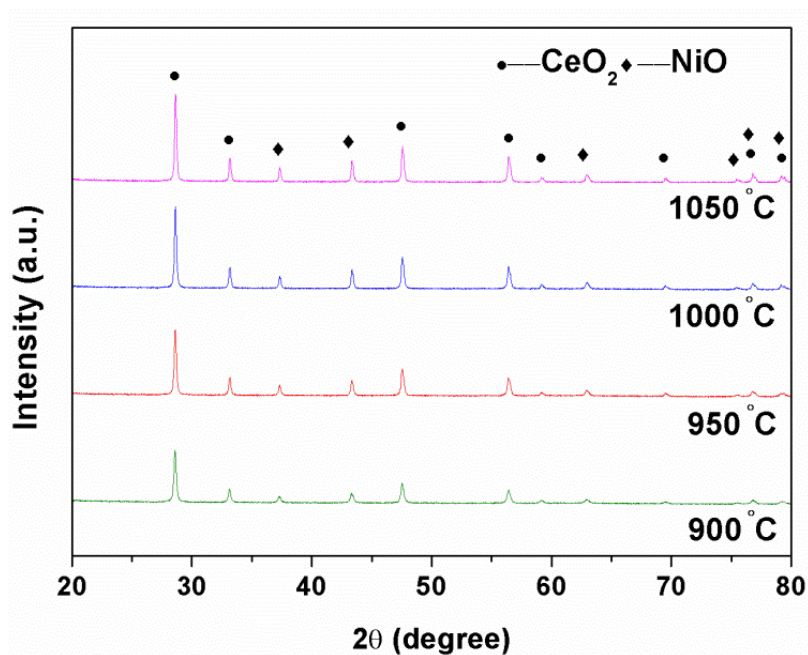


Figure 4-6. XRD patterns of the catalysts calcined at different temperatures.

TPR profiles can indicate the H₂ consumption of catalysts at different temperatures, and the H₂ amount can be quantified according to the peak area. The TPR profiles of NiO/CeO₂ catalysts in Figure 4-7 show that H₂ consumption mainly occurred between 300 and 450 °C, which is related to the reduction of NiO particles. As the calcination temperature was increased, the peaks moved to high temperatures because the increase of particle size slowed down the NiO reduction. Also, the H₂ consumption decreased due to the reduced surface area of NiO (Figure 4-7b). The peak at 450-600 °C is thought to be caused by NiO-induced CeO₂ reduction [11, 22]: the reduction of NiO causes hydrogen species to spill over, and then induces CeO₂ support reduction. The reduction indicates an interaction between NiO and CeO₂ support. At high calcination temperatures, the interaction became strong because of the sintering between NiO and CeO₂. The strong interaction promotes NiO-induced CeO₂ reduction, resulting in the increased amount of H₂ consumption.

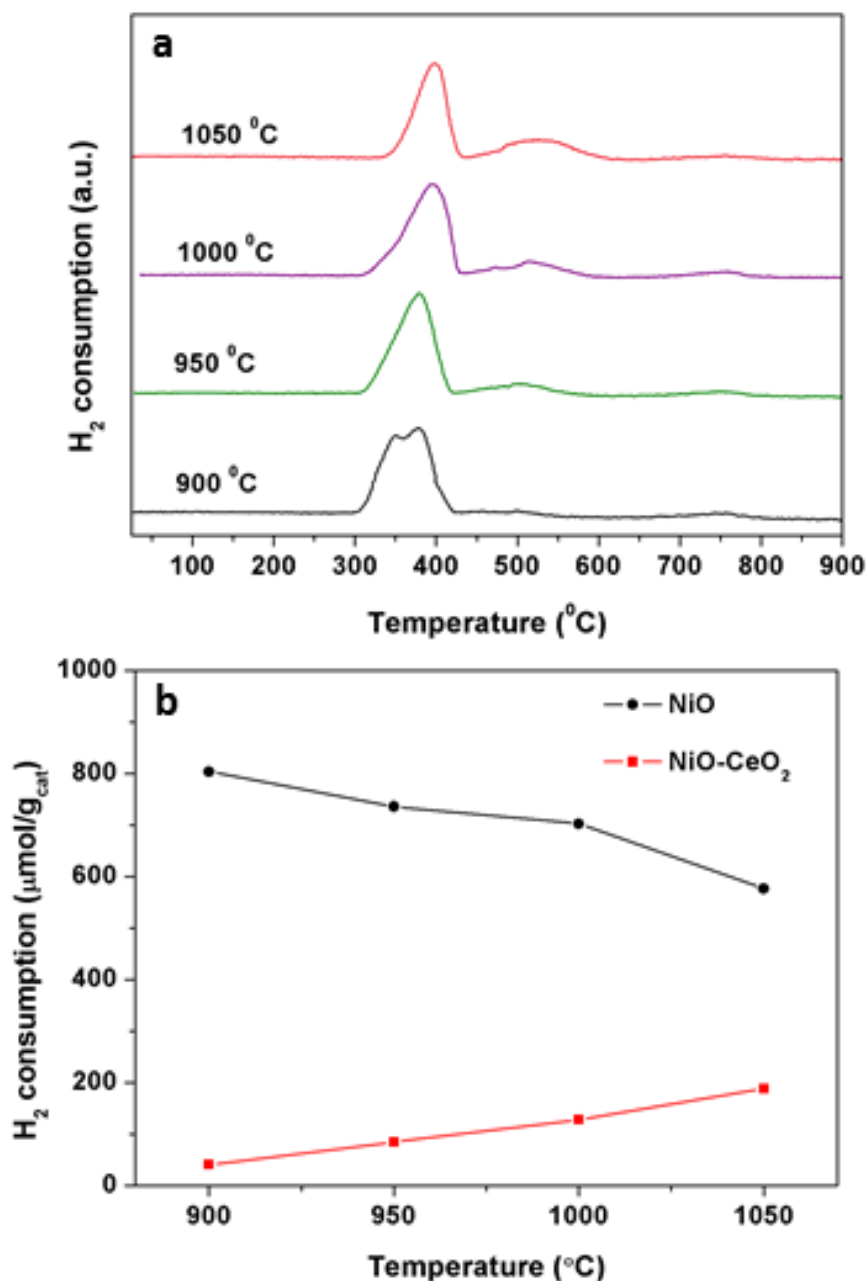


Figure 4-7. TPR profiles (a) and the corresponding H₂ consumption (b) of the catalysts calcined at different temperatures.

As shown in Figure 4-8, the calcination temperature of the catalyst greatly affects steam reforming performance. The reforming performance over the catalyst calcined at 900 °C was extremely unstable within the operation time of 300 min, and CH₄ conversion decreased from 90% at 60 min to 60% at 300 min. The performance decay was caused by severe coke formation, as shown in Figure 4-9a. The fibrous structure of the catalyst had been completely destroyed after testing due to the

growth of carbon fibres. In contrast, no carbon fibre is found in the other tested catalysts. Accordingly, the strong interaction between NiO and CeO₂ is critical to achieve coking-resistance. Performance decays of the other catalysts might be attributed to catalyst sintering and/or the formation of amorphous carbon, which cannot be observed by SEM. However, the catalyst sintering was limited by the three-dimensional structure, and the fibrous structure was retained after testing.

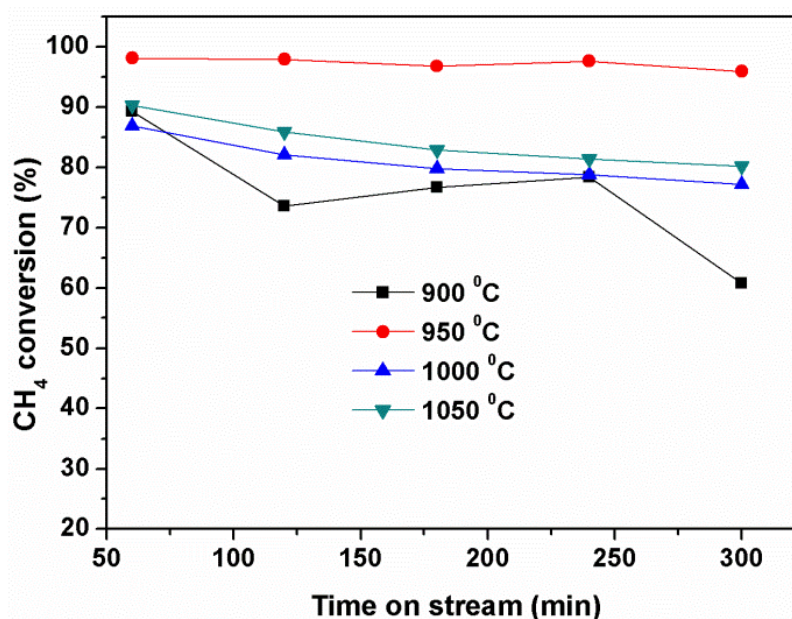


Figure 4-8. CH₄ conversion in steam reforming at 800 °C within 300 min over the catalysts calcined at different temperatures.

Among the three catalysts, the catalyst calcined at 950 °C showed the highest activity in steam reforming due to the smallest particle size of NiO catalyst. In addition, it showed more stable performance than the other two catalysts. This might be attributed to the catalyst having a more stable structure. As seen from Figure 4-9, the catalyst calcined at 950 °C well-retained the fibrous structure after test, while the other tested catalysts showed deformed fibres. The catalyst calcined at 1050 °C showed a slightly higher activity than that calcined at 1000 °C. This might be due to the stronger interaction between NiO and CeO₂, as shown in TPR profiles. Similar result was found during dry reforming [18].

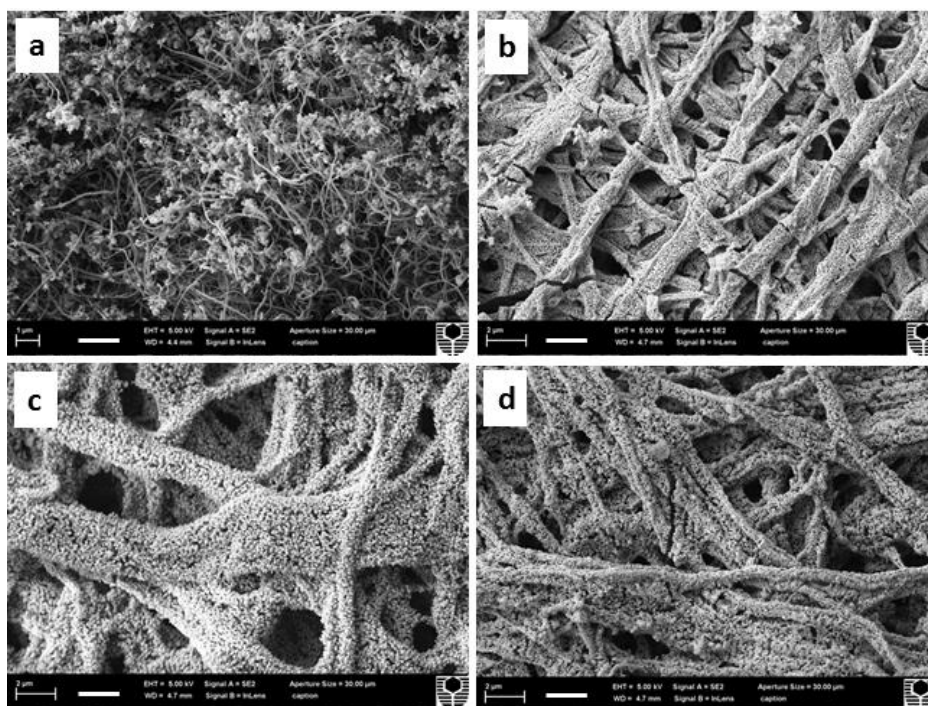


Figure 4-9. SEM images of the tested catalysts calcined at different temperatures: a, 900 °C; b, 950 °C; c, 1000 °C and d, 1050 °C. Scale bar is 2 μm.

4.3.5 The effect of operating temperature and steam/CH₄ ratio

CH₄ conversion and H₂/CO ratio were also investigated as functions of operating temperature and steam/CH₄ ratio. As shown in Figure 4-10a, CH₄ conversion increased with operating temperature due to the endothermic reaction of steam reforming. Achieving high H₂/CO ratio is important in the production H₂ by steam reforming, which is controlled by the gas-water shift reaction involved in steam reforming. Increasing the operating temperature reduced the H₂/CO ratio because the gas-shift reaction is exothermic. Also, raising the steam/CH₄ ratio in the feedstock could increase the H₂/CO ratio (Figure 4-10b). CH₄ conversion initially increased with the steam/CH₄ ratio and achieved 93% at the steam/CH₄ ratio of 2. Then, above a ratio of 2, CH₄ conversion started decrease. It is attributed to the competition between CH₄ and steam in occupying active sites of catalyst [23].

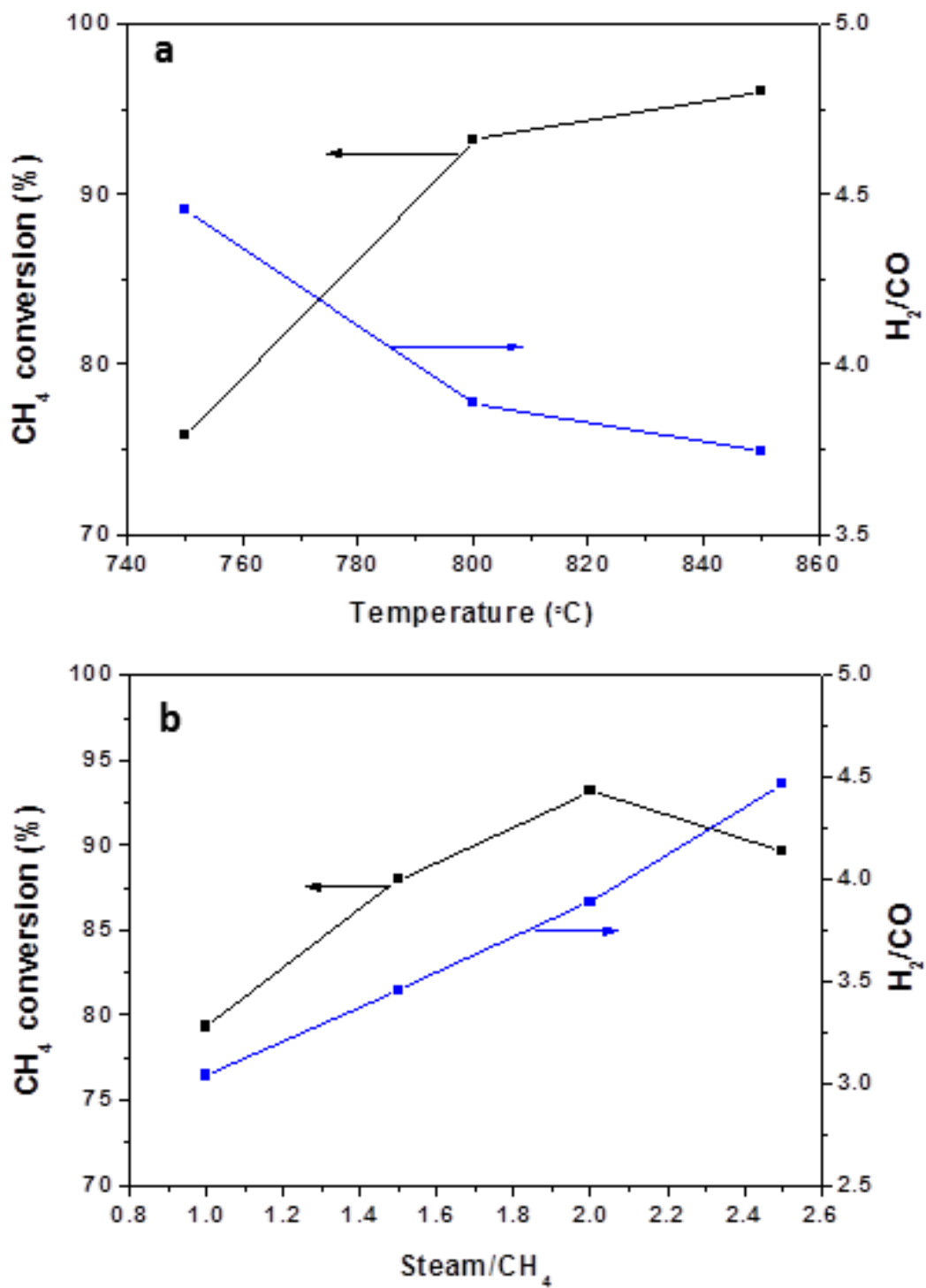


Figure 4-10. CH₄ conversion and H₂ /CO ratio as functions of operating temperature and steam/CH₄ ratio during steam reforming over the catalyst calcined at 950 °C.

4.4 Conclusions

The dependences of catalyst microstructure on immersion time and calcination temperature during templating NiO/CeO₂ nanocatalysts using ESM have been studied in detail. At the immersion time of 3 h, the template catalyst has a robust structure. The optimized calcination temperature is 950 °C in term of achieving high and stable methane conversion during steam reforming. Methane conversion reaches about 98% at 800 °C at the steam/CH₄ ratio of 2, and no obvious performance decay was found within 300 min owing to the robust hierarchical microstructure of the nanocatalyst. The study presents a novel and facile template process to prepare nanocatalysts with potential applications in industry.

4.5 References

- [1] M.J. Gradassi, N.W. Green, Economics of natural gas conversion processes, *Fuel Process. Technol.*, 42 (1995) 65-83.
- [2] A. Jess, R. Popp, K. Hedden, Fischer-Tropsch-synthesis with nitrogen-rich syngas - Fundamentals and reactor design aspects, *Applied Catalysis a-General*, 186 (1999) 321-342.
- [3] A. Kambolis, H. Matralis, A. Trovarelli, C. Papadopoulou, Ni/CeO₂-ZrO₂ catalysts for the dry reforming of methane, *Appl. Catal. A-Gen.*, 377 (2010) 16-26.
- [4] T.V. Choudhary, V.R. Choudhary, Energy-efficient syngas production through, catalytic oxy-methane reforming reactions, *Angew. Chem. Int. Ed.*, 47 (2008) 1828-1847.
- [5] J.G. Seo, M.H. Youn, Y. Bang, I.K. Song, Hydrogen production by steam reforming of simulated liquefied natural gas (LNG) over mesoporous nickel-M-alumina (M = Ni, Ce, La, Y, Cs, Fe, Co, and Mg) aerogel catalysts, *Int. J. Hydrog. Energy*, 36 (2011) 3505-3514.
- [6] K.O. Christensen, D. Chen, R. Lodeng, A. Holmen, Effect of supports and Ni crystal size on carbon formation and sintering during steam methane reforming, *Appl. Catal. A-Gen.*, 314 (2006) 9-22.
- [7] M.C.J. Bradford, M.A. Vannice, CO₂ reforming of CH₄ over supported Pt catalysts, *J. Catal.*, 173 (1998) 157-171.
- [8] P.P. Silva, F.A. Silva, H.P. Souza, A.G. Lobo, L.V. Mattos, F.B. Noronha, C.E. Hori, Partial oxidation of methane using Pt/CeZrO₂/Al₂O₃ catalysts - effect of preparation methods, *Catal. Today*, 101 (2005) 31-37.

- [9] A.J. de Abreu, A.F. Lucrecio, E.M. Assaf, Ni catalyst on mixed support of CeO₂-ZrO₂ and Al₂O₃: Effect of composition of CeO₂-ZrO₂ solid solution on the methane steam reforming reaction, *Fuel Process. Technol.*, 102 (2012) 140-145.
- [10] B. Bej, N.C. Pradhan, S. Neogi, Production of hydrogen by steam reforming of methane over alumina supported nano-NiO/SiO₂ catalyst, *Catal. Today*, 207 (2013) 28-35.
- [11] V.M. Gonzalez-Delacruz, F. Ternero, R. Pereniguez, A. Caballero, J.P. Holgado, Study of nanostructured Ni/CeO₂ catalysts prepared by combustion synthesis in dry reforming of methane, *Appl. Catal. A-Gen.*, 384 (2010) 1-9.
- [12] Y.S. Jung, W.L. Yoon, Y.W. Rhee, Y.S. Seo, The surfactant-assisted Ni-Al₂O₃ catalyst prepared by a homogeneous precipitation method for CH₄ steam reforming, *Int. J. Hydrog. Energy*, 37 (2012) 9340-9350.
- [13] W. Zhang, D. Zhang, T.X. Fan, J.J. Gu, R. Ding, H. Wang, Q.X. Guo, H. Ogawa, Novel Photoanode Structure Templated from Butterfly Wing Scales, *Chem. Mater.*, 21 (2009) 33-40.
- [14] Y.S. Shin, J. Liu, J.H. Chang, Z.M. Nie, G. Exarhos, Hierarchically ordered ceramics through surfactant-templated sol-gel mineralization of biological cellular structures, *Adv. Mater.*, 13 (2001) 728-732.
- [15] D.H. Dong, Y.Z. Wu, X.Y. Zhang, J.F. Yao, Y. Huang, D. Li, C.Z. Li, H.T. Wang, Eggshell membrane-templated synthesis of highly crystalline perovskite ceramics for solid oxide fuel cells, *J. Mater. Chem.*, 21 (2011) 1028-1032.
- [16] D.H. Dong, J.F. Yao, Y.Z. Wu, X.Y. Zhang, G.S. Xu, C.Z. Li, H.T. Wang, A 3D fibrous cathode with high interconnectivity for solid oxide fuel cells, *Electrochem. Commun.*, 13 (2011) 1038-1041.
- [17] D.H. Dong, X. Shao, Z.T. Wang, C. Lievens, J.F. Yao, H.T. Wang, C.Z. Li, Fibrous NiO/CeO₂ nanocatalysts for the partial oxidation of methane at microsecond contact times, *RSC Adv.*, 3 (2013) 1341-1345.

- [18] Z.T. Wang, X. Shao, A. Larcher, K. Xie, D.H. Dong, C.Z. Li, A study on carbon formation over fibrous NiO/CeO₂ nanocatalysts during dry reforming of methane, *Catal. Today*, 216 (2013) 44-49.
- [19] T.X. Fan, S.K. Chow, Z. Di, Biomorphic mineralization: From biology to materials, *Prog. Mater. Sci.*, 54 (2009) 542-659.
- [20] D. Yang, L.M. Qi, J.M. Ma, Eggshell membrane templating of hierarchically ordered macroporous networks composed of TiO₂ tubes, *Adv. Mater.*, 14 (2002) 1543-1546.
- [21] D. Yang, L.M. Qi, J.M. Ma, Hierarchically ordered networks comprising crystalline ZrO₂ tubes through sol-gel mineralization of eggshell membranes, *J. Mater. Chem.*, 13 (2003) 1119-1123.
- [22] W.S. Dong, H.S. Roh, K.W. Jun, S.E. Park, Y.S. Oh, Methane reforming over Ni/Ce-ZrO₂ catalysts: effect of nickel content, *Appl. Catal. A-Gen.*, 226 (2002) 63-72.
- [23] C. Pistonesi, A. Juan, B. Irigoyen, N. Amadeo, Theoretical and experimental study of methane steam reforming reactions over nickel catalyst, *Appl. Surf. Sci.*, 253 (2007) 4427-4437.

Every reasonable effort has been made to acknowledge the owners of the copyright materials. I would be pleased to hear from any copyright owner who has been omitted or incorrectly acknowledged.

Chapter 5

Nanofibrous Ni/Al₂O₃ catalysts for high yield of syngas production

5.1 Introduction

Syngas, a mixture of CO and H₂, is an important intermediate in the conversion of natural gas to chemicals or liquid fuels (e.g. methanol). Syngas production by the partial oxidation of methane can achieve high yields as the catalytic reaction can complete within a contact time of microseconds to milliseconds with catalysts [1, 2]. However, these operations were conducted over noble metal gauze catalysts with short and fast mass transfer pathway (see Figure 5-1a). Noble metal gauzes are too expensive for practical applications; cheap Ni foam and meshes show limited catalytic activity due to low surface areas (< 0.1 m²g⁻¹) [3, 4]; coated monolith catalysts also show limited catalytic capacity because a large volume portion of the catalyst bed/reaction zone is occupied by supports [5-7].

Conventional supported powder catalysts have high catalytic capacity owing to small catalyst nanoparticles. However, the reactions over the powder catalysts are limited by the mass transfer within porous supports [8], as shown in Figure 5-1b.

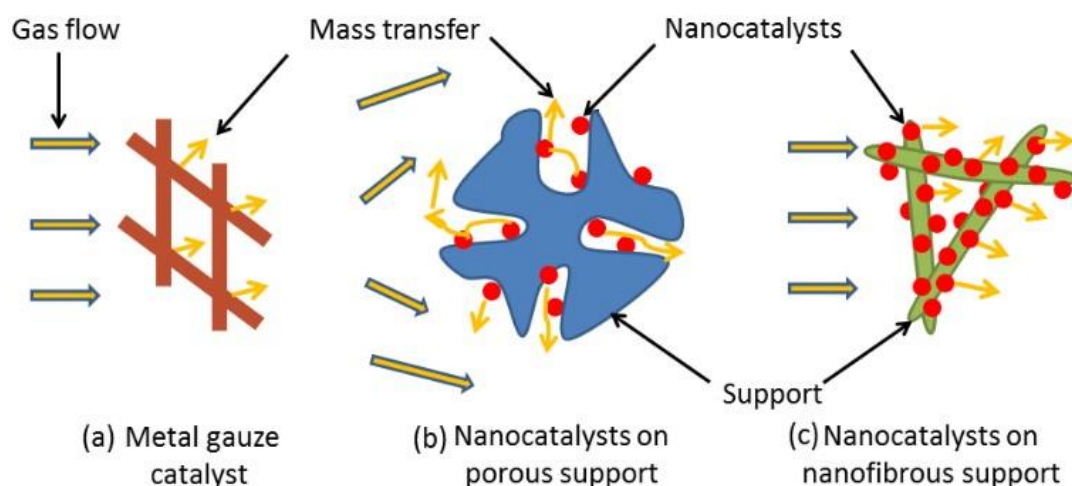


Figure 5-1. Comparison of mass transfers over the catalysts with different microstructures.

Moreover, these powder catalysts cannot be operated at high gas space velocities (GHSVs) because the resulted large pressure drop through the

catalyst bed causes safety issues. To reduce the pressure drop, the powder catalysts are made into pellets [9]. However, this exacerbates the mass transfer limitation.

It is believed that fibrous catalysts have advantages in mass transfer, heat transfer, pressure drop and productivity [10-13]. Like supported catalysts, nanocatalysts supported on ceramic fibers can achieve high catalytic activity. Having a similar structure to that of gauze, mesh and foam catalysts, fibrous catalysts provide short and fast mass transfer pathway for gas diffusion (see Figure 5-1c). Therefore, the fibrous catalysts possess the advantages of both supported catalysts and metal gauze catalysts for conducting high rate methane partial oxidation.

We had developed fibrous NiO/CeO₂ catalysts using eggshell membrane as a template, and above 96% of methane conversion was achieved at a contact time of 98 μ s [14]. However, it is hard to control the catalyst composition due to the absorption preference of eggshell membrane to different metal ions during templating synthesis. In addition, the catalyst fiber diameter of about 1 μ m is fixed by eggshell membrane template, and gas diffusion limitation exists within the porous ceramic fibers [15].

Electrospinning is an effective way to produce ceramic fibers with different diameters from 50 nm to 1 μ m, and the catalyst composition can be flexibly controlled by the spinning solution [16-18]. In this study, Ni/Al₂O₃ nanofibrous catalysts were prepared by electrospinning, and tested for methane partial oxidation. The effects of Ni content on catalyst crystal phase and methane conversion were also investigated.

5.2 Experimental

5.2.1 Catalyst preparation

Electrospinning was employed to prepare the fibrous catalysts, and the electrospinning process started with the preparation of a spinning solution.

Typically, $\text{Ni}(\text{NO}_3)_2 \cdot 6\text{H}_2\text{O}$ (> 99%), $\text{Al}(\text{NO}_3)_3 \cdot 9\text{H}_2\text{O}$ ($\geq 98\%$) and PVP ($M_w = 1.3 \times 10^6$) were dissolved in a mixture of deionized water and ethanol with a $\text{H}_2\text{O}/\text{C}_2\text{H}_5\text{OH}$ weight ratio of 4 to form the spinnable solution. The weight ratio of PVP in the solution was 13%, and the amounts of $\text{Ni}(\text{NO}_3)_2 \cdot 6\text{H}_2\text{O}$ and $\text{Al}(\text{NO}_3)_3 \cdot 9\text{H}_2\text{O}$ ($\geq 98\%$) were designed to form the catalysts with Ni contents of 7.4, 13.7, 19.2, 24.1, 28.4 and 32.3 wt%, respectively.

The spinning process was carried out on an electrospinning device (NABOND-NEU). For the spinning process, an electric field of 2.4 kV/cm was applied between a syringe tip and a collector that was wrapped with aluminium foil and positioned right below the tip. The feeding rate of the solution was 0.5 ml/min. The as-spun fibre mate was collected from the aluminium foil and then calcined in air at 1000 °C. All chemicals were purchased from Sigma Aldrich Australia.

5.2.2 Catalyst characterisation

The microstructure of the catalysts was observed via scanning electron microscopy (SEM, Zeiss Neon 40EsB FIBSEM). A scanning transmission electron microscope (STEM, JEOL3000) equipped with Energy-dispersive X-ray spectroscopy (Titan G2 60-300) was used to characterise the nanocatalysts by the operation at 80kV. The crystal phases of the spun catalysts were identified by using $\text{CuK}\alpha$ radiation with a Bruker D8 Advance diffractometer equipped with a LynxEye detector (Bruker-AXS, Karlsruhe, Germany) at a scan rate of 2 °/min and a step size of 0.02°. Temperature-programmed reduction (TPR) was carried out on a ChemBET3000 machine (Quantachrome Instruments). 0.03g of $\text{Ni}/\text{Al}_2\text{O}_3$ catalyst was loaded into a U-tube sample cell and held by quartz wool. Nitrogen was firstly introduced to expel the air in the testing system at a flow rate of 40 ml/min, and subsequently the moisture and impurities on the catalyst surface were removed at 250 °C for 30 min. Then, the sample cell was cooled down to room temperature, and then a gas mixture of 5% H_2 in N_2 was used for the TPR test. The catalysts were heated up to 1000 °C at a ramp rate of 10 °C /min. A thermal conductivity detector (TCD) detected the H_2 consumption by the catalyst reduction as a function of

temperature, which was monitored by TPRWinTM software. BET surface area was tested by nitrogen adsorption–desorption (TriStar II 3020, Micromeritics).

5.2.3 Methane reforming test

With the assistance of sieves, the prepared catalysts were crushed into flakes with sizes of 500-600 μm . Then, 0.015 g of the flake catalyst was put on a quartz filter that was set in the middle of a quartz tube reactor (inner diameter = 10 mm). The reactor was vertically positioned in and then heated by a tubular furnace, and a K-type thermocouple was placed on the top of the catalyst bed to monitor the temperature. Prior to methane reforming, a gas mixture of 20 vol% H_2/Ar was fed into the reactor at 750 $^\circ\text{C}$ to reduce the catalyst for 1 h, and then the reactant gas mixture of 10% CH_4 , 5% O_2 and 85% Ar (volume) was introduced into the reactor to conduct the reforming at 850 $^\circ\text{C}$ or designed temperatures. The gas flow rate was controlled by mass flow controllers (Alicat Scientific). The product gas composition from the reactor was analysed by gas chromatography (GC, Agilent 6890), and CH_4 conversion and selectivity were calculated as follow:

$$\text{CH}_4 \text{ conversion} = \frac{\text{CH}_{4,\text{in}} - \text{CH}_{4,\text{out}}}{\text{CH}_{4,\text{in}}}$$

$$\text{H}_2 \text{ selectivity} = \frac{\text{H}_{2,\text{out}}}{2(\text{CH}_{4,\text{in}} - \text{CH}_{4,\text{out}})}$$

$$\text{CO selectivity} = \frac{\text{CO}_{\text{out}}}{(\text{CH}_{4,\text{in}} - \text{CH}_{4,\text{out}})}$$

GHSV was calculated using the following equation:

$$\text{GHSV} = \frac{\text{Volumetric flow rate of feed gas at room temperature}}{\text{Catalyst weight}}$$

5.3 Results and discussions

5.3.1 Catalyst characterisation

5.3.1.1 X-ray diffraction (XRD)

Apart from the advantages mentioned above, fibrous catalysts have a high resistance to sintering, and catalyst sintering is one of two main reasons that cause catalyst deactivation [19]. One dimensional ceramic fiber supports have lower sinterability compared with ceramic particles; nanocatalyst particles supported on fibers are physically isolated, which significantly diminishes the aggregation of catalyst particles via sintering at high temperatures. To eliminate potential catalyst support sintering during reaction, the fibrous catalysts were calcined at 1000 °C during catalyst preparation, which is higher than the reaction temperature of 850 °C. The nanofibrous structure retains high surface area at high temperatures. For example, the BET surface area of the 24.1wt% Ni/Al₂O₃ catalyst is 19.9 m² g⁻¹, which is close to commercial 25wt% Ni/Al₂O₃ catalysts (22 m² g⁻¹) [20]. In the Ni/Al₂O₃ catalyst, Al₂O₃ acts as a support for Ni catalyst particles. During catalyst calcination, NiAl₂O₄ is formed when calcination temperature is high enough (e.g. above 700 °C) [21, 22]. The formation of NiAl₂O₄ is beneficial for improving Ni dispersion in the reduced catalyst [23].

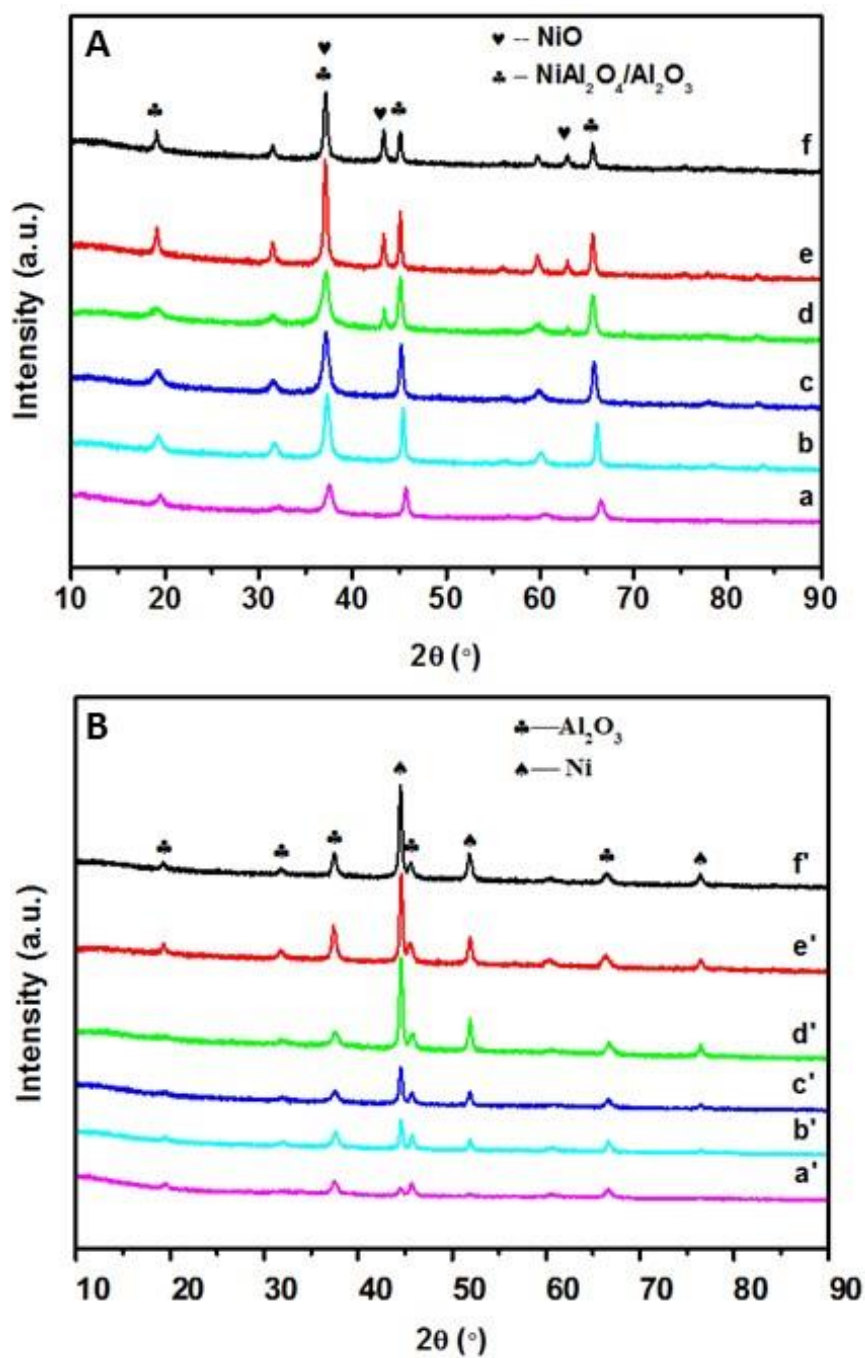


Figure 5-2. XRD patterns of the catalysts before (A) and after (B) reduction with different Ni contents: a, a'-7.4 wt%; b, b'-13.7 wt%; c, c'-19.2 wt%; d, d'-24.1 wt%; e, e'-28.4 wt%; f, f'-32.3 wt%.

Figure 5-2 shows the XRD patterns of the catalysts with different Ni contents before and after reduction. For the catalysts before reduction, as Ni content increases, the main Al_2O_3 peak at 37.5° shifts to the left, and finally stays at 37.1° , which corresponds to NiAl_2O_4 . Introducing Ni into Al_2O_3 crystals to

form NiAl_2O_4 increases the lattice parameters, which causes the peak shift [23]. As NiAl_2O_4 cannot tolerate excessive Ni, NiO is observed when Ni content is equal to or above 24.1 wt%. The same results were obtained from the TEM-EDS elemental mapping of the catalysts before reduction (see Figure 5-3). At the Ni content of 19.2 wt%, Ni distributes uniformly in the form of NiAl_2O_4 . Above the Ni content, NiO, with a higher Ni concentration compared with NiAl_2O_4 , presents and becomes aggregated as Ni content was increased. After reduction, the catalysts only present the peaks of Ni and Al_2O_3 , indicating both NiO and NiAl_2O_4 can be reduced to Ni [24].

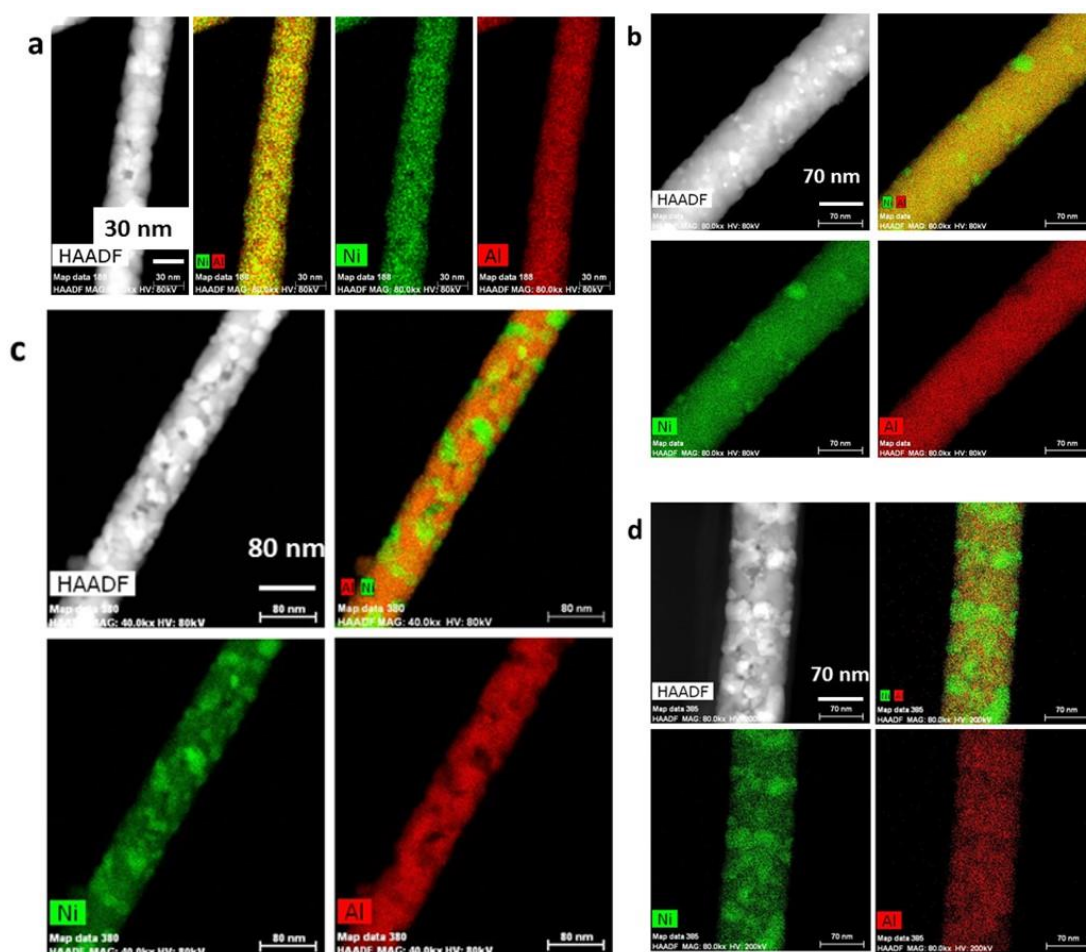


Figure 5-3. STEM-EDS elemental mapping of 19.2 wt% (a), 24.1 wt% (b), 28.4 wt% (c) and 32.3 wt% (d) Ni/ Al_2O_3 catalyst before reduction.

5.3.1.2 SEM/TEM

Figure 5-4a shows the fibrous structure of the catalyst after calcination at 1000 °C; the nanofibrous structure was retained at the high temperature. In contrast, conventional powder catalysts prepared by wet-chemical processes and impregnated catalysts are calcined at low temperatures (e.g. below 700 °C) to avoid catalyst and/or support aggregations. Moreover, the formation of NiAl₂O₄ at above 700 °C is essential to improve Ni particle dispersion in the reduced catalysts. The catalyst flakes have a thickness about 20 μm (Figure 5-4b), and the thin flask catalysts provide large contact area with reactant gas flow.

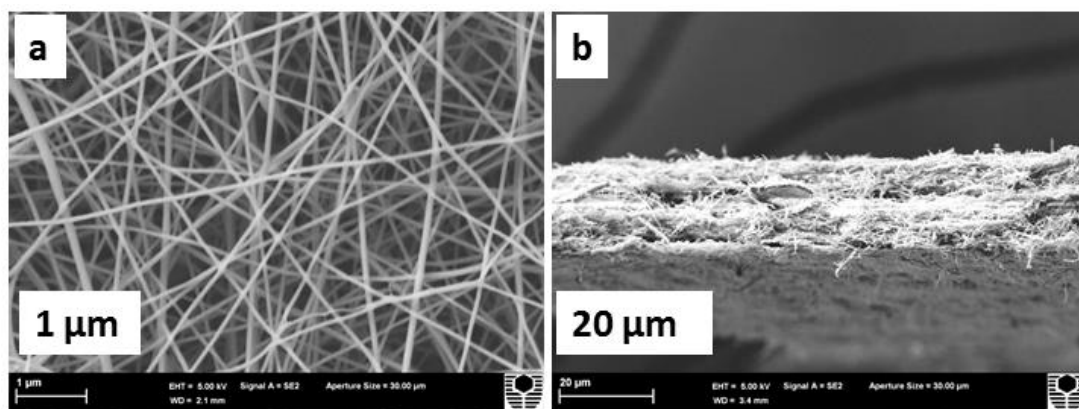


Figure 5-4. SEM images of an as-prepared Ni/ Al₂O₃ catalyst calcined at 1000 °C (a) and a cross section of the catalyst flakes (b).

After catalyst reduction by H₂, Ni particles are formed from NiO and NiAl₂O₄. As seen from Figure 5-5, small particles appear on the fibres. As the Ni content was increase to 19.2wt%, there are more and bigger Ni particles formed. However, it is hard to observe Ni particles from SEM images when the Ni content is increased to 24.1 wt%. TEM images (Figure 5-6) and EDS elemental mapping (Figure 5-7) show more details of the catalyst morphology. At the Ni content of 24.1 wt%, most of Ni particles formed by NiAl₂O₄ reduction have uniform sizes of less than 30 nm although there are some big particles formed by NiO reduction. As Ni content was increased, more and bigger Ni particles (above 30 nm) were formed due to NiO aggregation

mentioned above. In the meanwhile, Ni particles formed by NiAl_2O_4 reduction became small at the Ni content of 32.3 wt% (see Figure 5-7c), which might be attributed to the dispersion role of NiO. At the NiO content, there forms a NiO percolation to prevent NiAl_2O_4 aggregation during crystallisation, forming small NiAl_2O_4 crystals and therefore small Ni particles.

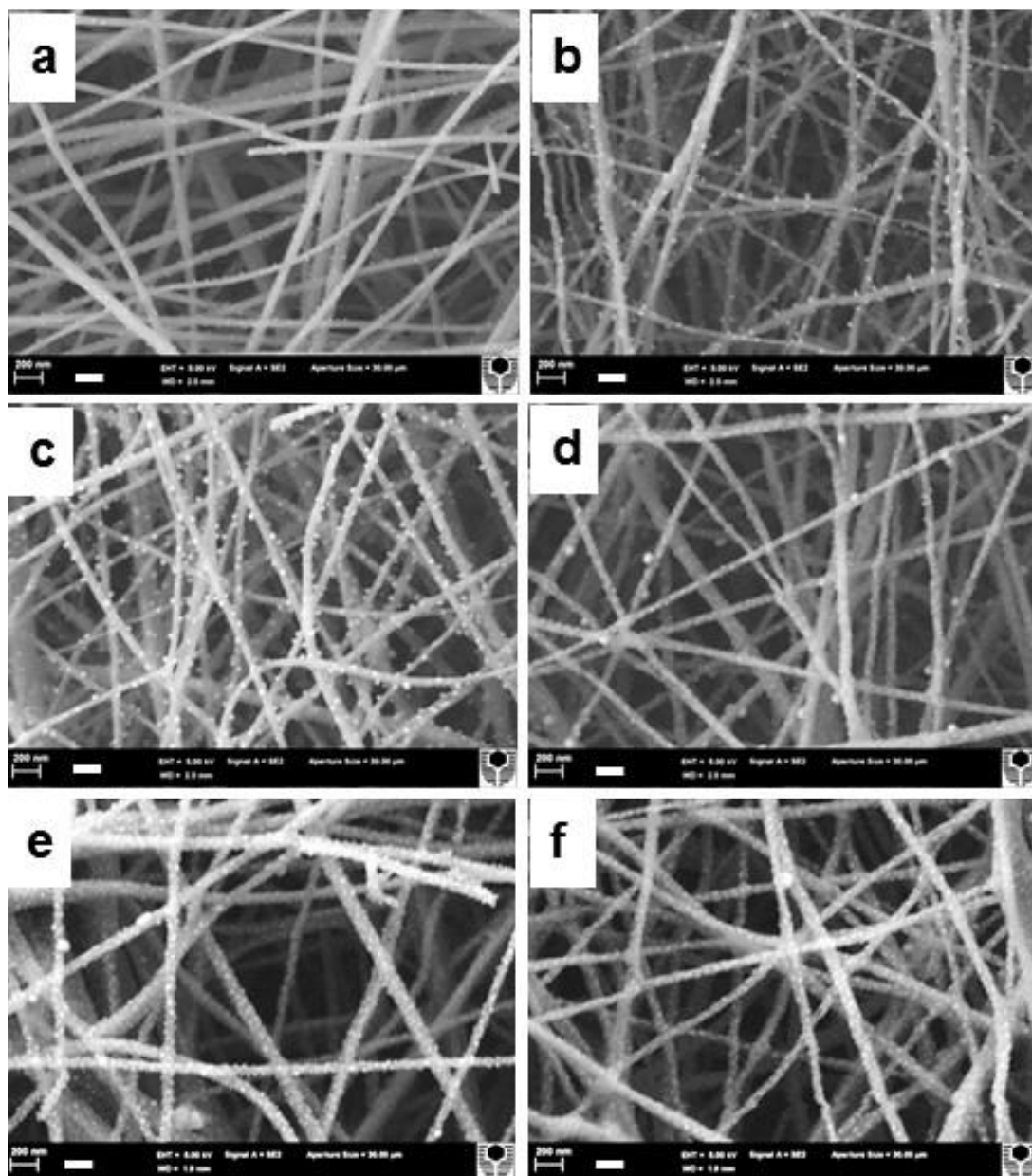


Figure 5-5. SEM images of the reduced catalysts with different Ni contents: a-7.4 wt%, b-13.7 wt%, c-19.2 wt% d-24.1 wt%, e-28.4 wt%, f-32.3 wt%. Scale bars are 200 nm.

Ni particles formed by NiAl_2O_4 reduction stand on the surface of Al_2O_3 fibre, which makes it easy to be observed. When NiO presents at high Ni contents, Ni particles formed by NiO reduction are located within fibres, where NiO was situated. Also, NiO reduction forms pore surface for Ni particles deposited from NiAl_2O_4 . These are reasons why it is hard to observe Ni particles from the SEM images at high Ni contents.

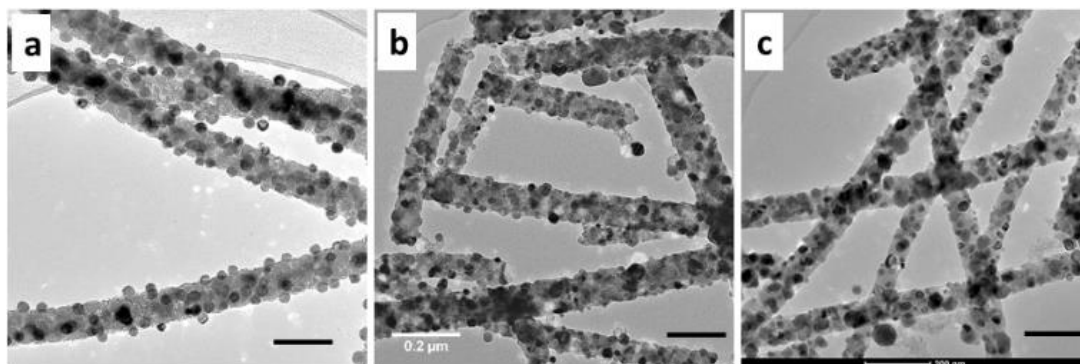


Figure 5-6. STEM images of 24.1wt% (a), 28.4 wt% (b) and 32.3 wt% (c) Ni/ Al_2O_3 catalyst after reduction. Scale bars are 100 nm.

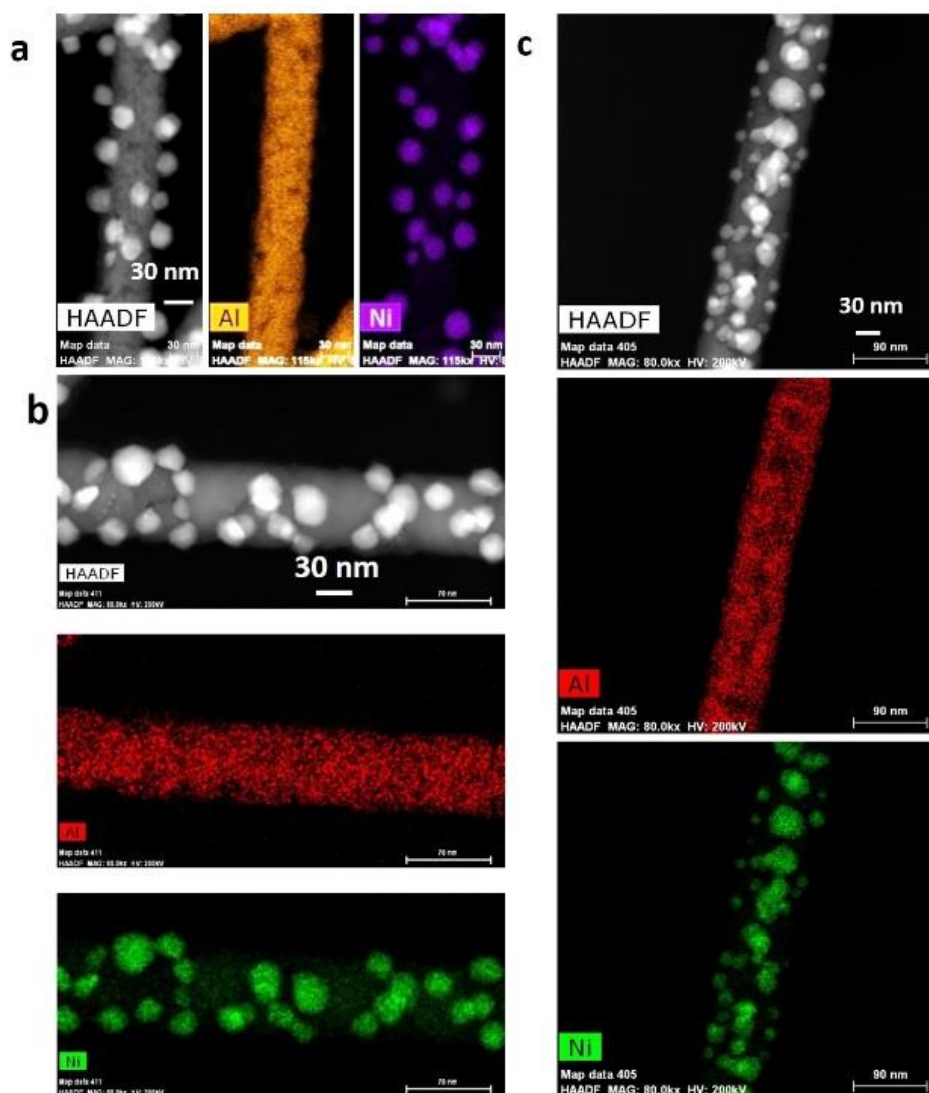


Figure 5-7. STEM-EDS elemental mapping of 24.1 wt% (a), 28.4 wt% (b) and 32.3 wt% (c) Ni/Al₂O₃ catalyst after reduction.

5.3.1.3 Temperature programmed reduction

TPR was performed on the fibrous catalysts to study their reduction behaviour and the interaction between Ni and the support. NiO and NiAl₂O₄ have different reducibilities due to different chemical bonds within the two. NiO can be reduced at low temperatures around 400 °C while NiAl₂O₄ reduction occurs at above 700 °C [25]. As shown in Figure 5-8, for the catalysts with the Ni content of 7.4 wt%, the catalyst shows the lowest reducibility and was reduced mainly at around 900 °C. As the Ni content increases, the reduction peak moves to around 850 °C, which should be related to NiAl₂O₄ reduction. Until

the Ni content increases to 24.1 wt%, H₂ consumption peak presents at around 400 °C, which is attributed to the reduction of NiO particles, as indicated in the XRD pattern. As the Ni content increases, the peak moves to higher temperatures and becomes broad. The peak shift indicates the increased interaction between NiO and NiAl₂O₄ [26]. In addition, the NiO particle size increases with Ni content, and therefore it takes a longer time to reduce the NiO, which is the reason that the peak becomes broad. As the Ni content increases, the high temperature peak initially moves to lower temperatures and then moves to higher temperatures; this phenomenon was observed in the previous study [27]. The change might be related to the distribution and dispersion of NiAl₂O₄, which changes with Ni content.

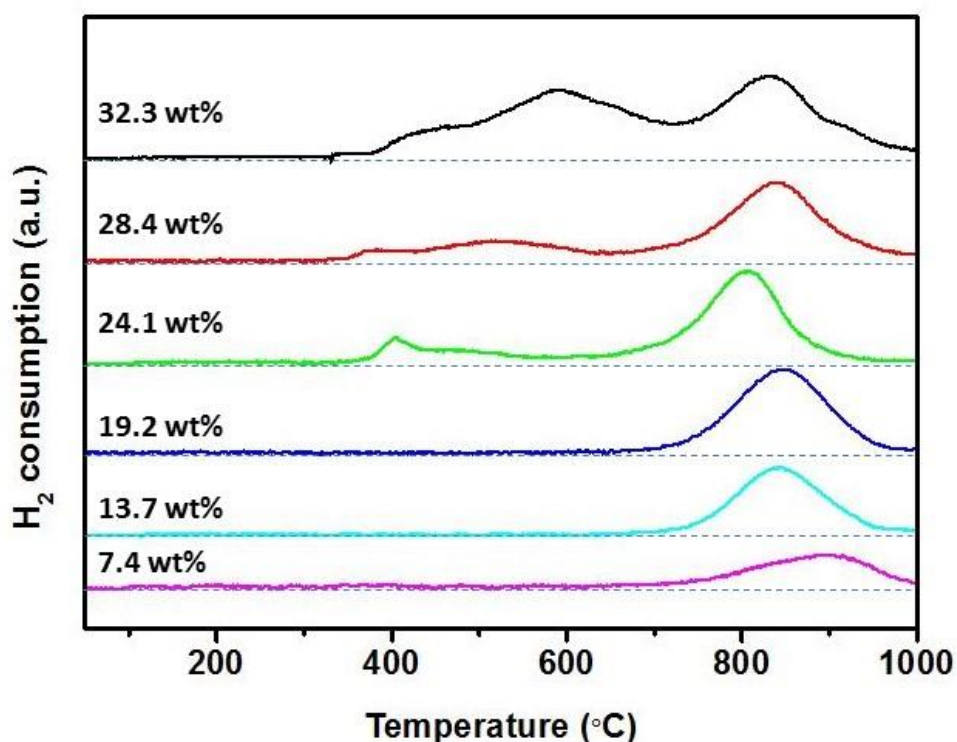


Figure 5-8. TPR profiles of the catalysts with different Ni contents.

Table 5-1. Peak areas from the TPR profiles.

| Ni content (wt%) | Peak area at low temperatures | Peak area at high temperatures | Total peak area |
|------------------|-------------------------------|--------------------------------|-----------------|
| 7.4 | | 1324 | 1324 |
| 13.7 | | 2104 | 2104 |
| 19.2 | | 2715 | 2715 |
| 24.1 | 671 | 2797 | 3468 |
| 28.4 | 1017 | 2799 | 3816 |
| 32.3 | 3696 | 3082 | 6778 |

The H₂ consumption peak areas are summarized in Table 5-1. The area of the high temperature peak (above 700 °C) attributed to NiAl₂O₄ reduction increases steadily as the Ni content increases, and becomes stable when the Ni content reaches 24.1 wt%, indicating the saturation of NiAl₂O₄ formation. Excessive NiO on the surface contributes to the low temperature peak (below 700 °C), and this peak area increases with Ni content. There is a large area increase when the Ni content reaches 32.3 wt%. It might be attributed to the formation of NiO percolation or phase separation promotes NiO reduction.

5.3.2 Catalytic methane partial oxidation

5.3.2.1 Effect of NiO content

The fibrous Ni/Al₂O₃ catalysts were tested for the partial oxidation of methane to investigate the effect of Ni content. At the Ni content of 7.4 wt%, there was no CH₄ conversion. This is because the Ni-deficient spinel is difficult to reduce, as shown in the TPR results. Furthermore, it can easily be oxidised by oxygen in the input gas. Previous studies demonstrated that the small NiO particles that are hard to reduce are easily oxidized due to the interaction between NiO and the support [26, 28]. As shown in Figure 5-9a, CH₄ conversion increases with Ni content up to 24.1 wt%. Further increasing Ni content causes decreased CH₄ conversions, especially when the Ni content increases from 24.1 wt% to 28.4wt%. It is attributed to NiO aggregation, which is indicated by SEM and TEM-EDS images discussed above. It also indicates

the catalytic activity is mainly contributed by small Ni particle from NiAl_2O_4 reduction.

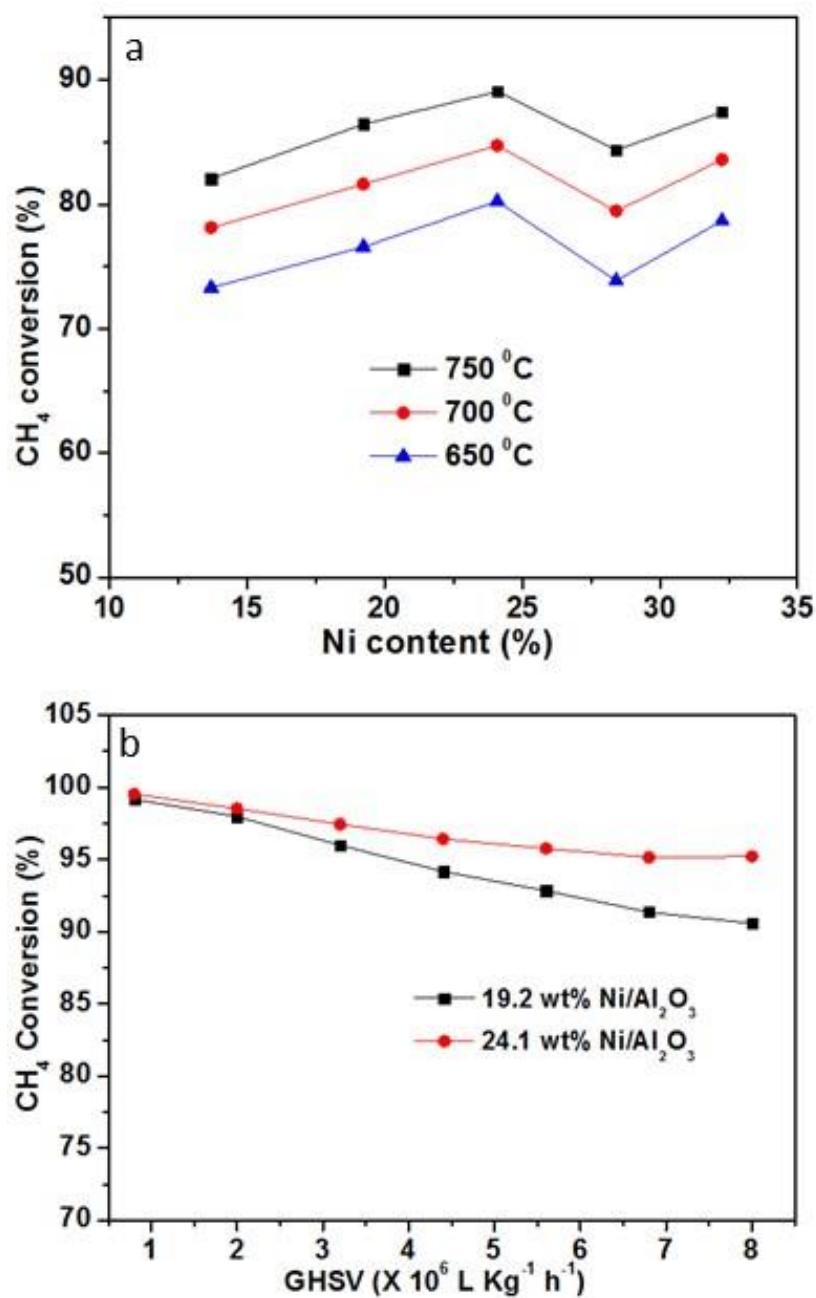


Figure 5-9. Effect of catalyst content on methane conversion at a GHSV of 8×10^6 $\text{L Kg}^{-1} \text{h}^{-1}$ (a) and the effect of GHSV on methane conversion at the Ni contents of 19.2 wt% and 24.1 wt% at 850 °C (b).

To further explore the catalytic capacity of the fibrous catalysts for the comparison with other catalysts in term of syngas yield, two catalysts with Ni contents of 19.2 wt% and 24.1 wt% were chosen to be operated at 850 °C. Figure 5-9b shows that CH₄ conversion decreases with GHSV increase for both catalysts, while the 24.1 wt% Ni/Al₂O₃ catalyst exhibits a lower rate of decrease than the 19.2 wt% Ni/Al₂O₃ sample, owing to the higher NiO content and the smaller Ni particle sizes in the former. As the gas flow rate increases from 8×10^5 to 8×10^6 LKg⁻¹h⁻¹, CH₄ conversion decreases from 99.6% to 95.6%; a 4% of conversion decrease, when the flow rate is increased by 10 times, shows the high catalytic capacity of the fibrous catalyst. Moreover, the conversion curve starts to plateau as the GHSV increases to 7×10^6 LKg⁻¹h⁻¹, indicating that the high conversion can probably be achieved at high GHSVs. The GHSV of 8×10^6 LKg⁻¹h⁻¹ is the highest recorded for the partial oxidation of methane over supported catalysts.

5.3.2.2 Syngas yield comparison

The fibrous catalysts were compared with other supported catalysts in term of syngas yield in Table 5-2. To be able to be operated at high GHSVs, these catalysts were made into granules by either crushing commercial cylinder catalysts or pelletizing powder catalysts to reduce pressure drop through catalyst beds. At 850 °C, the fibrous 24.1wt% Ni/Al₂O₃ catalyst exhibited a CO yield of 7.5×10^5 Lkg⁻¹h⁻¹ and a hydrogen yield of 1.4×10^6 Lkg⁻¹h⁻¹, which are about 10 times higher than that of the developed Ni-based catalysts prepared by combustion or impregnation [29, 30]. Moreover, methane conversion over a NiCo_{0.2}Mg_{1.2}O_x/ZrO₂ catalyst decreased 20% (from 92% to 72%) when the GHSV was increased about 10 times (from 6.2×10^4 to 5×10^5 Lkg⁻¹h⁻¹), which is much higher than that (4%) over the fibrous Ni/Al₂O₃ catalyst mentioned above. The CO and/or hydrogen yields at 800 °C of the fibrous 13.7 wt% Ni/Al₂O₃ catalyst are 1-2 orders of magnitude higher than that of a commercial 25 wt% Ni/Al₂O₃ catalyst and a 9.2wt% Ni/Al₂O₃ catalyst prepared by impregnation [20, 31]. Furthermore, the fibrous catalyst produced similar syngas yield as noble metal catalysts [32, 33]. Compared with our previously reported Ni/CeO₂ (47.8 wt% NiO/CeO₂) fibrous catalyst templated by eggshell membrane [14], the fibrous 24.1 wt% Ni/Al₂O₃ catalyst produced 6 times more syngas. Moreover, the fibrous Ni/Al₂O₃ catalyst can be manufactured at a much lower cost

than the NiO/CeO₂ catalyst in terms of materials and preparation process. The electrospinning process is easier to be scaled up than the eggshell membrane-templating process.

Table 5-2. Comparison of syngas yield by the nanofibrous catalyst and conventional supported catalysts.

| Catalyst | Preparation method | Feed gas | Reforming temperature (Lkg ⁻¹ h ⁻¹) | GHSV | CH ₄ conversion | selectivity | | | Yield (L kg ⁻¹ h ⁻¹) | | Reference |
|---|---------------------------------|---|--|----------------------|----------------------------|-------------|----------------|---------------------|---|-------------------------|-----------|
| | | | | | | CO | H ₂ | CO | H ₂ | | |
| 24.1 wt% Ni/Al ₂ O ₃ | Electrospinning | 10CH ₄ :5O ₂ :85Ar | 850°C | 8×10 ⁵ | 95% | 98% | 93% | 7.5×10 ⁵ | 1.4×10 ⁶ | This study ^a | |
| 10 wt% NiO-1 wt% Li ₂ O-5 wt% La ₂ O ₃ /Al ₂ O ₃ | Combustion and pelletisation | 2CH ₄ :1O ₂ :3N ₂ | 850°C | 1.44×10 ⁵ | 92% | 99% | | 4.4×10 ⁴ | | 29 | |
| NiCo _{0.2} Me _{1.2} O ₄ /ZrO ₂ | Impregnation | 64CH ₄ :36O ₂ | 850°C | 6.2×10 ⁴ | 92% | 95% | 94% | 3.5×10 ⁴ | 6.9×10 ⁴ | 30 | |
| 13.7 wt% Ni/Al ₂ O ₃ | Electrospinning | 10CH ₄ :5O ₂ :85Ar | 800°C | 8×10 ⁵ | 85% | 94% | 89% | 6.4×10 ⁵ | 1.2×10 ⁶ | This study ^b | |
| 25 wt% Ni/Al ₂ O ₃ | Commercial granules | 1.78CH ₄ :1O ₂ :25He | 800°C | 6×10 ⁴ | 97% | 95% | | 2×10 ³ | | 20 | |
| 9.2 wt% Ni/Al ₂ O ₃ | Impregnation | 7CH ₄ :3.5O ₂ :14N ₂ | 800°C | 1.57×10 ⁵ | 95% | 98% | 97% | 4.3×10 ⁴ | 8.6×10 ⁴ | 31 | |
| 1wt%Rh/MgO | Impregnation and pelletisation | 2CH ₄ :1O ₂ | 836°C | 1.8×10 ⁶ | 78% | 91% | 93% | 8×10 ⁵ | 1.7×10 ⁶ | 32 | |
| 0.5wt%Rh/Al ₂ O ₃ | Precipitation and pelletisation | 63CH ₄ :37O ₂ | 920°C | 4.6×10 ⁵ | 90% | 90% | 99.7% | 2.4×10 ⁵ | 5.2×10 ⁵ | 33 | |
| 47.8wt%NiO/CeO ₂ (41.8wt%Ni/CeO ₂) | Eggshell membrane-templating | 10CH ₄ :5O ₂ :85Ar | 850°C | 1.3×10 ⁶ | 97% | 89% | 90% | 1.2×10 ⁵ | 2.3×10 ⁵ | 14 | |

^a Conversion and selectivity data from Fig. 9 and Fig. 10, respectively.

^b Conversion and selectivity data from Fig. 11.

CO yield = GHSV × CH₄ concentration × CH₄ conversion × CO selectivity

H₂ yield = GHSV × CH₄ concentration × CH₄ conversion × 2 × H₂ selectivity

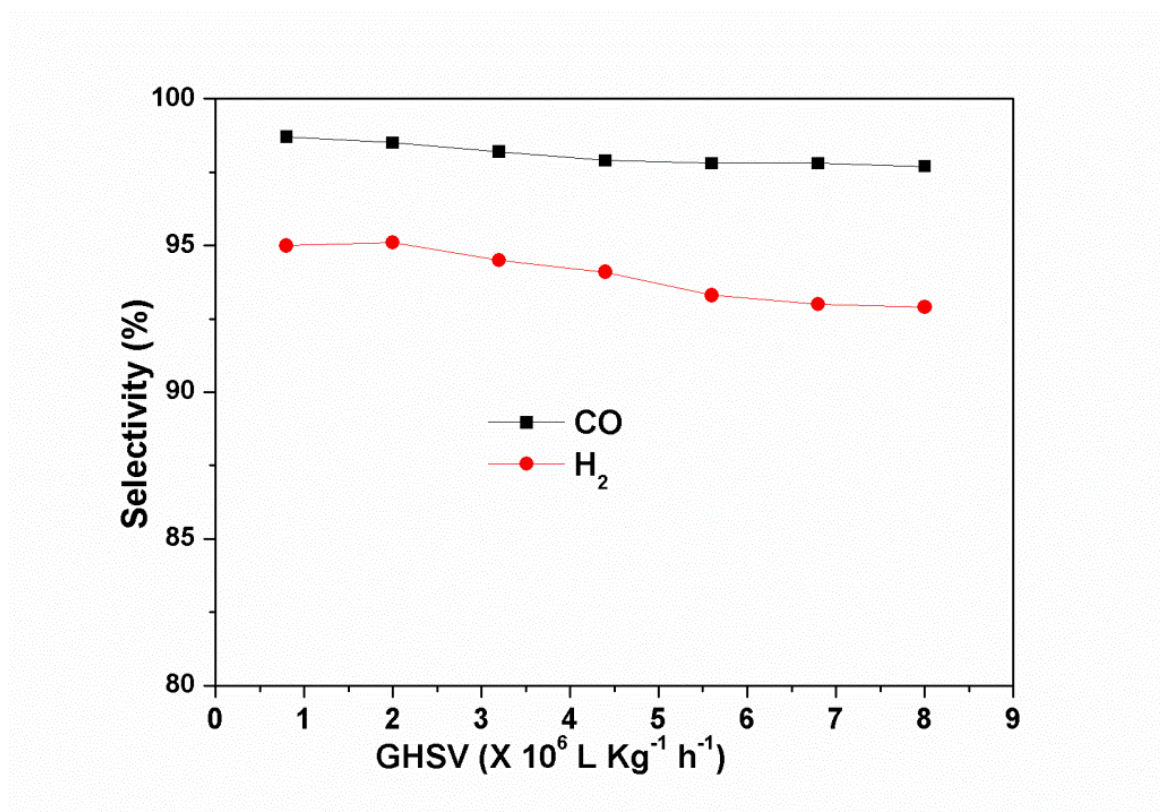


Figure 5-10. Selectivity of syngas produced by 24.1 wt% Ni/Al₂O₃ catalyst

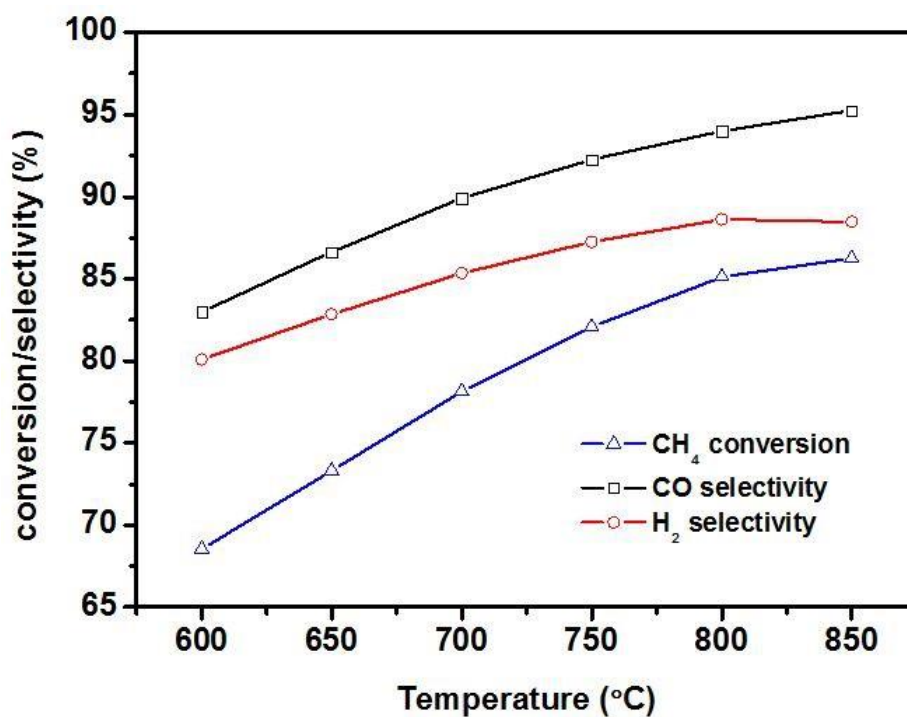


Figure 5-11. CH₄ conversion and syngas selectivity produced by the 13.7wt% Ni/Al₂O₃ catalyst at different operation temperatures.

5.3.2.3 Catalyst structural stability

To study catalyst structure stability during catalytic reaction, the 24.1 wt% Ni/Al₂O₃ catalyst was selected to test methane partial oxidation for 10 hours. As shown in Figure 5-12, methane conversion was maintained at about 98.5%. CO and hydrogen selectivities are 98.5% and 94.7%, respectively. It is because that both fibrous structure and nanocatalyst morphology are retained during reaction, and there is no Ni aggregation observed from the catalyst after test for 10 hours in SEM image (Figure 5-13) and TEM/EDS images (Figure 5-14). There was amorphous carbon formed around the catalyst fibres according to TEM/EDS results. In our previous study, carbon fibres formed over Ni/CeO₂ catalyst lifted Ni particles and destroyed the fibrous structure. Accordingly, the strong interaction between Ni and support in the Ni/Al₂O₃ catalyst prevented the formation of carbon fibres. Based on the stable performance within 10 hours, the amorphous carbon might form at the beginning of the reaction or they are C-containing radicals such as CH₃· absorbed on catalyst surface during reaction. The stable catalyst microstructure contributes to the stable reforming performance.

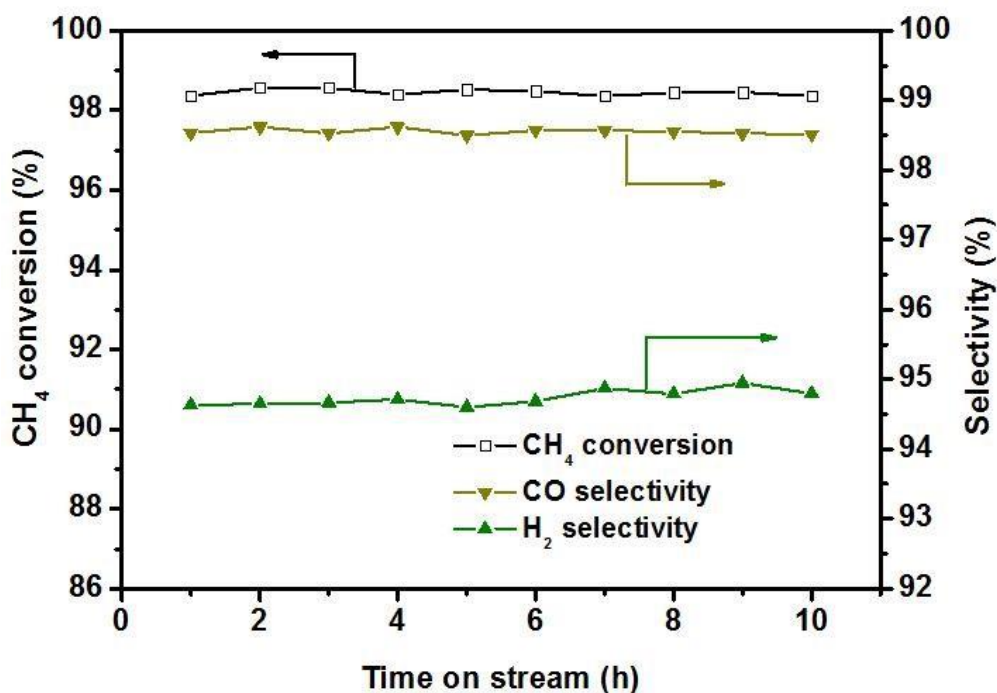


Figure 5-12. Stability test of 24.1 wt% Ni/Al₂O₃ catalyst during methane partial oxidation over 10 hours at a GHSV of 4×10^6 LKg⁻¹h⁻¹.

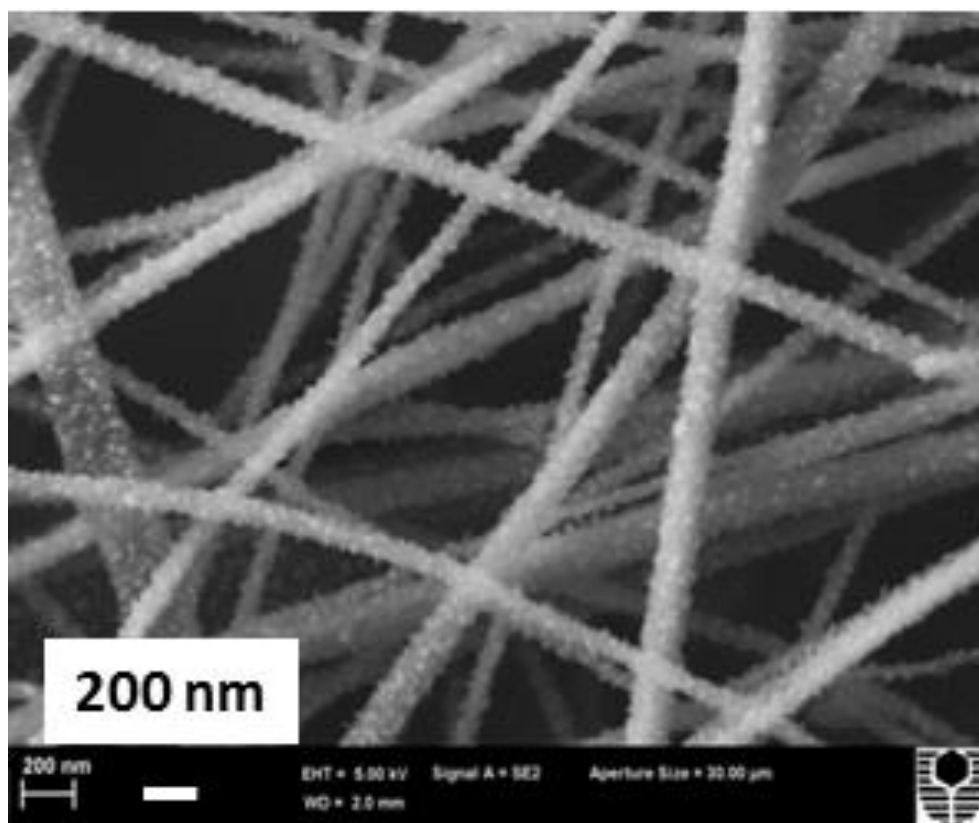


Figure 5-13. SEM image of the 24.1 wt% Ni/Al₂O₃ catalyst after methane partial oxidation for 10 hours.

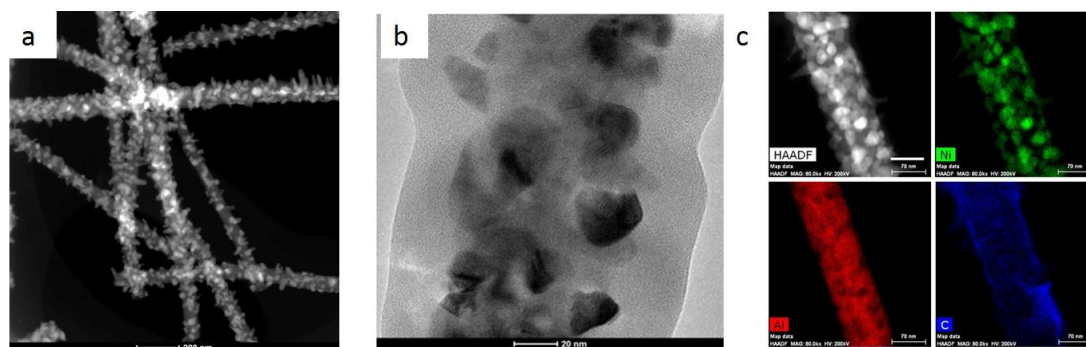


Figure 5-14. TEM image (a, b) and EDS elemental mapping (c) of the 24.1 wt% Ni/Al₂O₃ catalyst after methane partial oxidation for 10 hours.

5.4 Conclusions

Nanofibrous Ni/Al₂O₃ catalysts prepared by electrospinning have demonstrated high yields of syngas via methane partial oxidation, owing to the combined advantages of metal gauze catalysts and supported nanocatalysts. Like metal gauze catalysts, the

fibrous catalysts have fast mass transfer pathways and can be operated at high flow rates without producing a substantial pressure drop; the high conversion is attributed to the nanosized catalysts supported on nanofibers like conventional supported catalysts. Increasing Ni content up to 24.1 wt% produced the increased methane conversion, and further increasing Ni content caused NiO aggregation and therefore no performance increase. The fibrous catalysts demonstrated high structural stability during 10-hour operation with stable performance, which potentially contributes to the catalysts stability.

5.5 References

- [1] M. Fathi, K.H. Hofstad, T. Sperle, O.A. Rokstad, A. Holmen, Partial oxidation of methane to synthesis gas at very short contact times, *Catal. Today*, 42 (1998) 205-209.
- [2] D.A. Hickman, L.D. Schmidt, Production of syngas by direct catalytic oxidation of methane, *Science*, 259 (1993) 343-346.
- [3] E.B.H. Quah, C.Z. Li, Roles of desorbed radicals and reaction products during the oxidation of methane using a nickel mesh catalyst, *Applied Catalysis a-General*, 258 (2004) 63-71.
- [4] L. Coleman, E. Croiset, W. Epling, M. Fowler, R. Hudgins, Evaluation of Foam Nickel for the Catalytic Partial Oxidation of Methane, *Catal. Lett.*, 128 (2009) 144-153.
- [5] M. Maestri, A. Beretta, G. Groppi, E. Tronconi, P. Forzatti, Comparison among structured and packed-bed reactors for the catalytic partial oxidation of CH₄ at short contact times, *Catal. Today*, 105 (2005) 709-717.
- [6] K.L. Hohn, L.D. Schmidt, Partial oxidation of methane to syngas at high space velocities over Rh-coated spheres, *Appl. Catal. A-Gen.*, 211 (2001) 53-68.
- [7] P.M. Witt, L.D. Schmidt, Effect of flow rate on the partial oxidation of methane and ethane, *J. Catal.*, 163 (1996) 465-475.
- [8] A.S. Bodke, S.S. Bharadwaj, L.D. Schmidt, The effect of ceramic supports on partial oxidation of hydrocarbons over noble metal coated monoliths, *J. Catal.*, 179 (1998) 138-149.
- [9] A. Obradovic, B. Likozar, J. Levec, Steam Methane Reforming over Ni-based Pellet-type and Pt/Ni/Al₂O₃ Structured Plate-type Catalyst: Intrinsic Kinetics Study, *Ind. Eng. Chem. Res.*, 52 (2013) 13597-13606.

- [10] E. Reichelt, M.P. Heddrich, M. Jahn, A. Michaelis, Fiber based structured materials for catalytic applications, *Appl. Catal. A-Gen.*, 476 (2014) 78-90.
- [11] D.H. Dong, J.F. Yao, Y.Z. Wu, X.Y. Zhang, G.S. Xu, C.Z. Li, H.T. Wang, A 3D fibrous cathode with high interconnectivity for solid oxide fuel cells, *Electrochem. Commun.*, 13 (2011) 1038-1041.
- [12] D.H. Dong, Y. Wu, Z. X.Y. Zhang, J. Yao, F., Y. Huang, D. Li, C.Z. Li, H.T. Wang, Eggshell membrane-templated synthesis of highly crystalline perovskite ceramics for solid oxide fuel cell, *J. Mater. Chem.*, 21 (2011) 5.
- [13] B. Wang, Y. Wang, Y. Lei, N. Wu, Y. Gou, C. Han, D. Fang, Hierarchically porous SiC ultrathin fibers mat with enhanced mass transport, amphipathic property and high-temperature erosion resistance, *Journal of Materials Chemistry A*, 2 (2014) 20873-20881.
- [14] D.H. Dong, X. Shao, Z.T. Wang, C. Lievens, J.F. Yao, H.T. Wang, C.Z. Li, Fibrous NiO/CeO₂ nanocatalysts for the partial oxidation of methane at microsecond contact times, *RSC Adv.*, 3 (2013) 1341-1345.
- [15] Z. Wang, X. Shao, X. Hu, G. Parkinson, K. Xie, D. Dong, C.-Z. Li, Hierarchically structured NiO/CeO₂ nanocatalysts templated by eggshell membranes for methane steam reforming, *Catal. Today*, 228 (2014) 199-205.
- [16] Y.Q. Dai, W.Y. Liu, E. Formo, Y.M. Sun, Y.N. Xia, Ceramic nanofibers fabricated by electrospinning and their applications in catalysis, environmental science, and energy technology, *Polym. Adv. Technol.*, 22 326-338.
- [17] D. Noon, A. Seubsai, S. Senkan, Oxidative Coupling of Methane by Nanofiber Catalysts, *ChemCatChem*, 5 (2013) 146-149.
- [18] H. Qu, S. Wei, Z. Guo, Coaxial electrospun nanostructures and their applications, *Journal of Materials Chemistry A*, 1 (2013) 11513-11528.

- [19] T.V. Choudhary, V.R. Choudhary, Energy-efficient syngas production through, catalytic oxy-methane reforming reactions, *Angew. Chem. Int. Ed.*, 47 (2008) 1828-1847.
- [20] D. Dissanayake, M.P. Rosynek, K.C.C. Kharas, J.H. Lunsford, Partial oxidation of methane to carbon monoxide and hydrogen over a Ni/Al₂O₃ catalyst, *J. Catal.*, 132 (1991) 117-127.
- [21] Y.-S. Seo, Y.-S. Jung, W.-L. Yoon, I.-G. Jang, T.-W. Lee, The effect of Ni content on a highly active Ni-Al₂O₃ catalyst prepared by the homogeneous precipitation method, *International Journal of Hydrogen Energy*, 36 (2011) 94-102.
- [22] N. Salhi, A. Boulahouache, C. Petit, A. Kiennemann, C. Rabia, Steam reforming of methane to syngas over NiAl₂O₄ spinel catalysts, *International Journal of Hydrogen Energy*, 36 (2011) 11433-11439.
- [23] G.H. Li, L.J. Hu, J.M. Hill, Comparison of reducibility and stability of alumina-supported Ni catalysts prepared by impregnation and co-precipitation, *Appl. Catal. A-Gen.*, 301 (2006) 16-24.
- [24] Y. Cesteros, P. Salagre, F. Medina, J.E. Sueiras, Preparation and characterization of several high-area NiAl₂O₄ spinels. Study of their reducibility, *Chemistry of Materials*, 12 (2000) 331-335.
- [25] C.P. Li, Y.W. Chen, Temperature-programmed-reduction studies of nickel oxide alumina catalysts - effects of the preparation method, *Thermochimica Acta*, 256 (1995) 457-465.
- [26] J. Zielinski, morphology of nickel alumina catalysts, *J. Catal.*, 76 (1982) 157-163.
- [27] J.G. Seo, M.H. Youn, H.-I. Lee, J.J. Kim, E. Yang, J.S. Chung, P. Kim, I.K. Song, Hydrogen production by steam reforming of liquefied natural gas (LNG)

over mesoporous nickel-alumina xerogel catalysts: Effect of nickel content, Chem. Eng. J., 141 (2008) 298-304.

[28] A. Kadkhodayan, A. Brenner, TEMPERATURE-PROGRAMMED REDUCTION AND OXIDATION OF METALS SUPPORTED ON GAMMA-ALUMINA, J. Catal., 117 (1989) 311-321.

[29] Y. Chen, W. Zhou, Z. Shao, N. Xu, Nickel catalyst prepared via glycine nitrate process for partial oxidation of methane to syngas, Catalysis Communications, 9 (2008) 1418-1425.

[30] V.R. Choudhary, K.C. Mondal, T.V. Choudhary, Methane reforming over a high temperature stable-NiCoMgO_x supported on zirconia-hafnia catalyst, Chem. Eng. J., 121 (2006) 73-77.

[31] H. Ozdemir, M. A. F. Oksuzomer and M. A. Gurkaynak, Int. J. Hydrog. Energy, 2010, 35, 12147-12160.

[32] H. Tanaka, R. Kaino, K. Okumura, T. Kizuka, K. Tomishige, Catalytic performance and characterization of Rh-CeO₂/MgO catalysts for the catalytic partial oxidation of methane at short contact time, J. Catal., 268 (2009) 1-8.

[33] S. Specchia, L.D. Vella, B. Lorenzut, T. Montini, V. Specchia, P. Fornasiero, Effect of the Catalyst Load on Syngas Production in Short Contact Time Catalytic Partial Oxidation Reactors, Industrial & Engineering Chemistry Research, 49 (2010) 1010-1017.

Every reasonable effort has been made to acknowledge the owners of the copyright materials. I would be pleased to hear from any copyright owner who has been omitted or incorrectly acknowledged.

Chapter 6

Effects of calcination temperature of electrospun fibrous Ni/Al₂O₃ catalysts on the dry reforming of methane

6.1 Introduction

Calcination is an important step of catalyst preparation to turn catalyst precursors into catalysts or metal oxides (e.g. NiO), which can be reduced *in situ* to metal catalysts to perform catalytic reactions. The calcination temperature greatly determines the catalyst properties and subsequent catalytic performance.

A high calcination temperature can cause catalyst particles to sinter and therefore to loss catalytic activity [1, 2]. However, the high calcination temperature increases the interaction between catalyst particles and support [3]. A strong interaction can be beneficial for achieving high coking-resistance and catalytic activity owing to high catalyst dispersion [4, 5]. Moreover, the high calcination temperature is required to form some catalysts with special characteristics. For example, Ni nanocatalyst is exsolved from $\text{La}_{0.8}\text{Sr}_{0.2}\text{Cr}_{0.82}\text{Ni}_{0.18}\text{O}_{3-\delta}$ perovskite ceramic during reduction [6]; Ni nanocatalyst is formed *in situ* during the reduction of NiAl_2O_4 spinel ceramic [7]. These nanocatalysts exhibit high dispersion and the strong interaction with the support while the spinel and perovskite phases are only formed at high calcination temperatures (e.g. 700 - 900 °C) [8, 9]. Accordingly, it is necessary to study the effects of calcination temperature on catalyst properties to optimize preparation process.

NiAl_2O_4 catalyst precursors can be prepared by either an impregnation process or a wet-chemical synthesis process. There is a limited amount of NiAl_2O_4 formed on Al_2O_3 support surface during the impregnation process [10]. The catalysts prepared by the wet-chemical synthesis process readily aggregate during the calcination at high temperatures [11, 12]. The catalyst aggregation can increase mass transfer resistance and even make some catalyst particles inaccessible for catalytic reactions, which results in the complication of catalyst calcination temperature effect on catalytic performance. Furthermore, if catalysts are calcined at a lower temperature than the reaction temperature [13], the subsequent sintering of the catalysts during the reaction will mask the effects of calcination temperature. Therefore, a catalyst with a stable structure is highly desired to study the effects of calcination temperature on catalyst dispersion, the catalyst/support interaction and catalytic performance.

Our previous study found that fibrous Ni/Al₂O₃ catalysts prepared by an electrospinning process retained the fibrous structure at a calcination temperature of 1000 °C because the fibrous structure has high resistance to sintering [14]. Utilizing the structure-stable fibrous catalysts, this study will investigate the effects of calcination temperature on the properties of electrospun fibrous Ni/Al₂O₃ catalysts, including crystallinity, microstructure, particle size, reducibility and finally catalytic performance during the dry reforming of methane. The effect of reduction temperature on catalyst properties will also be studied. To our knowledge, it has not been reported previously.

6.2 Experimental

6.2.1 Catalyst preparation

Fibrous catalysts were prepared by an electrospinning process. A mixture of H₂O/C₂H₅OH with a weight ratio of 4:1 was used as a solvent. Polyvinylpyrrolidone (PVP, molecular weight 1.3×10⁶ by Light scattering) was added to the solvent to adjust solution viscosity and form a spinnable solution. The PVP weight ratio in the solution was 15%. Ni(NO₃)₂·6H₂O (> 99%) and Al(NO₃)₃·9H₂O (≥ 98%) were dissolved in the solution to form a catalyst precursor solution. Our previous study found only NiAl₂O₄ presented when Ni content equaled to or was below 19.2 wt%, and NiO would appear when the Ni content was higher than 19.2 wt% [14]. To study the effects of calcination temperature on Ni catalyst from the reduction of NiAl₂O₄, the catalyst with a Ni content of 19.2 wt% in the final Ni/Al₂O₃ catalyst was chosen in this study. 5.622 g of Ni(NO₃)₂·6H₂O and 17.707 g of Al(NO₃)₃·9H₂O (≥ 98%) were added into 40 g of the PVP solution. All chemicals were purchased from Sigma Aldrich Australia.

Electrospinning was conducted using an electrospinning device (NABOND-NEU) with an electric field of 2.4 kV/cm between a syringe tip and an aluminum foil collector. The feeding rate of the solution was 0.5 ml/min. The as-spun fiber mat was collected from the collector and then dried at 55 °C. The fiber composite was calcined in air at 700, 800, 900 and 1000 °C, respectively, to be turned into ceramic fibers.

6.2.2 Catalyst characterisation

The crystallinities of the ceramic fibers before and after reduction by 20 vol% H₂ in Ar for 1 hour were identified using CuK α radiation with a Bruker D8 Advance diffractometer equipped with a LynxEye detector (Bruker-AXS, Karlsruhe, Germany) at a scan rate of 2°/min and a step size of 0.02°. The microstructure of fibrous catalysts was observed via a scanning electron microscopy (SEM, Zeiss Neon 40EsB FIBSEM). The catalyst reducibility was tested by the temperature-programmed reduction (TPR), which was carried out on a ChemBET3000 system (Quantachrome Instruments). 0.03g of the Ni/Al₂O₃ catalyst was put into a U-tube sample cell and held by quartz wool. Before the test, the catalyst surface was cleaned by nitrogen at 250 °C. The sample cell was then cooled to room temperature for the test using 5% H₂ in N₂. The test was operated from room temperature to 1000 °C at a ramp rate of 10°C /min.

6.2.3 Catalytic reforming test

The catalytic performance of the fibrous catalysts was tested for the dry reforming of methane. Firstly, the calcined ceramic fiber mat was crushed into flakes with sizes of about 500 μ m and then loaded into a quartz tube reactor with an inner diameter of 10 mm, in which a quartz frit was set in the middle of the tube to hold the catalyst bed. The quartz reactor was vertically held in a furnace to be heated up to desired temperatures. After the reduction by 20 vol% H₂ in Ar, the furnace temperature was set at the reaction temperature of 500 °C. The reactant gas of 10% CH₄ and 10% CO₂ balanced with Ar was introduced into the reactor to conduct reforming. Gas flow rates were controlled by mass flow controllers (Alicat Scientific). Gas chromatography (GC, Agilent 6890) was used to quantify product gas composition. After the reactions, the reactor was cooled down with a flow of Ar to avoid the oxidation of catalyst including carbon.

6.3 Results and discussions

6.3.1 Catalyst crystallinity

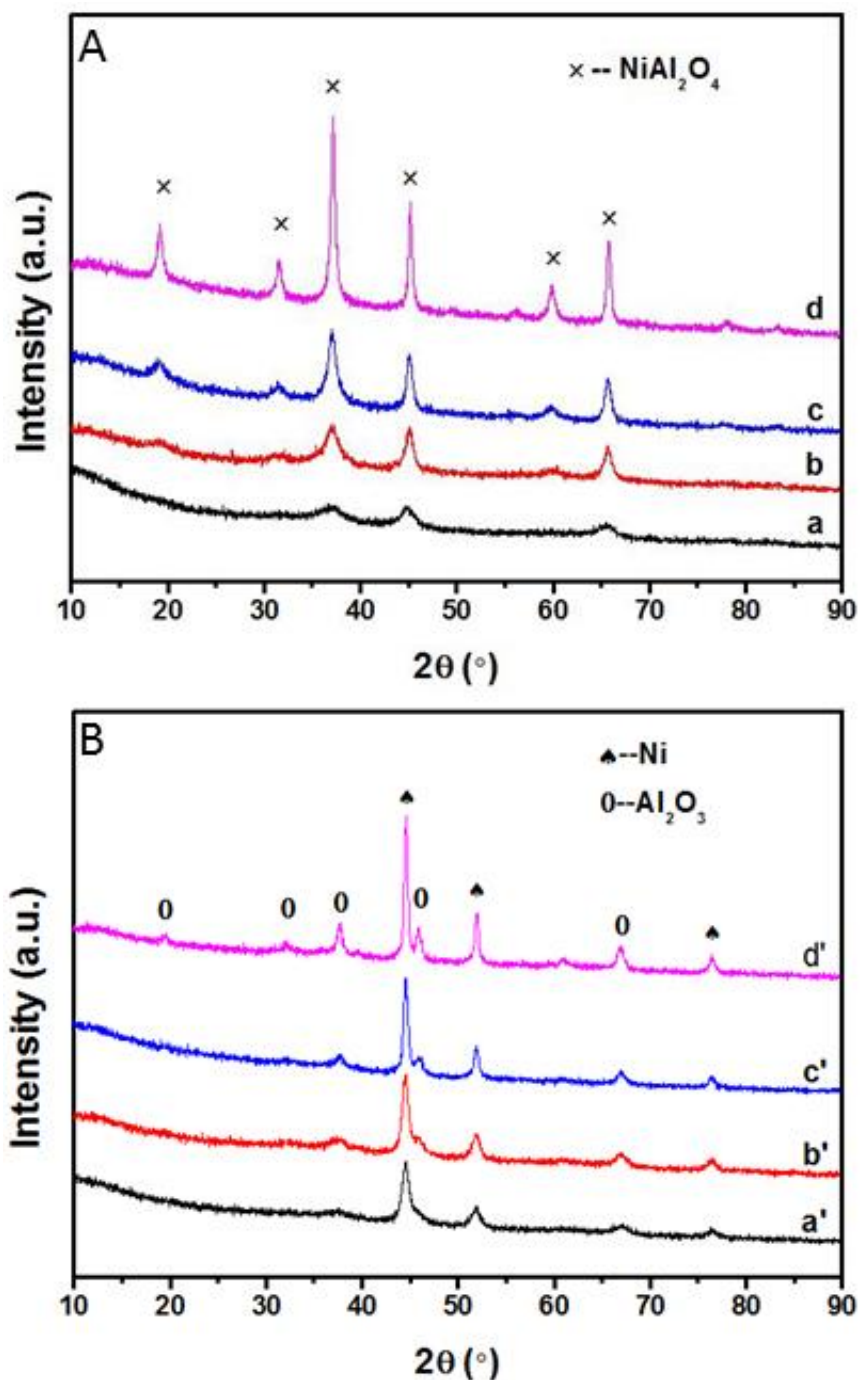


Figure 6-1. XRD patterns of the Ni/Al₂O₃ catalysts before (A) and after (B) reduction at 750 °C for 1 hour at different calcination temperatures: a, a' - 700 °C; b, b' - 800 °C; c, c' - 900 °C; d, d' - 1000 °C.

To investigate the effects of catalyst calcination temperature on catalyst properties, the electrospun fiber composites were calcined at different temperatures ranging from 700 to 1000 °C because NiAl₂O₄ formation normally starts at around 700 °C [8]. As shown in the XRD patterns in Figure 6-1A, at the calcination temperature of 700 °C, the crystallinity of NiAl₂O₄ spinel is very low, which confirms that a high temperature is required to form NiAl₂O₄ spinel. The crystallinity was improved as the calcination temperature increased. Correspondingly, the reduced catalysts showed the increased Ni crystal size with calcination temperature according to diffraction intensities in Figure 6-1B. Calculated using the Scherrer Equation, the Ni crystal sizes after reduction at 750 °C are 8.8, 11.1, 17.8 and 18.1nm, at the calcination temperatures of 700, 800, 900 and 1000 °C, respectively. According to the desired catalyst composition of 19.2 wt% Ni/Al₂O₃, NiAl₂O₄ and Al₂O₃ existed in the calcined catalysts. There is no clear diffraction peak referring to Al₂O₃ in Figure 6-1A. It is because that the intensities of Al₂O₃ peaks (see in Figure 6-1B) are much lower than that of NiAl₂O₄ peaks and Al₂O₃ peaks are also very close to NiAl₂O₄ peaks [15].

6.3.2 Catalyst reducibility

The calcination temperature is believed to affect the interaction between Ni catalyst and support and therefore catalyst reducibility [16]. A stronger interaction results in a lower reducibility. The TPR was run to test catalyst reducibility, and the results are shown in Figure 6-2. To compare the catalyst reducibility, the TPR tests were operated at the same conditions, including temperature ramp rate and gas flow rate. For the catalysts calcined at 700 and 800 °C, reduction started from ~420 °C, which is close to the NiO reduction temperatures [10]. It is attributed to the low crystallinities of NiAl₂O₄ spinel ceramics according to the XRD results. As the calcination temperature increased, the crystallinity of the NiAl₂O₄ spinel ceramics was improved, resulting in high on-set reduction temperatures of 600 and 700 °C for the catalysts calcined at 900 and 1000 °C, respectively. Hence, the catalyst reducibility decreased as calcination temperature increased because of the strong catalyst/support interaction formed at high calcination temperatures. The interaction originates from the formation of NiAl₂O₄ spinel ceramic [17], and becomes strong as the ceramic crystallinity is improved.

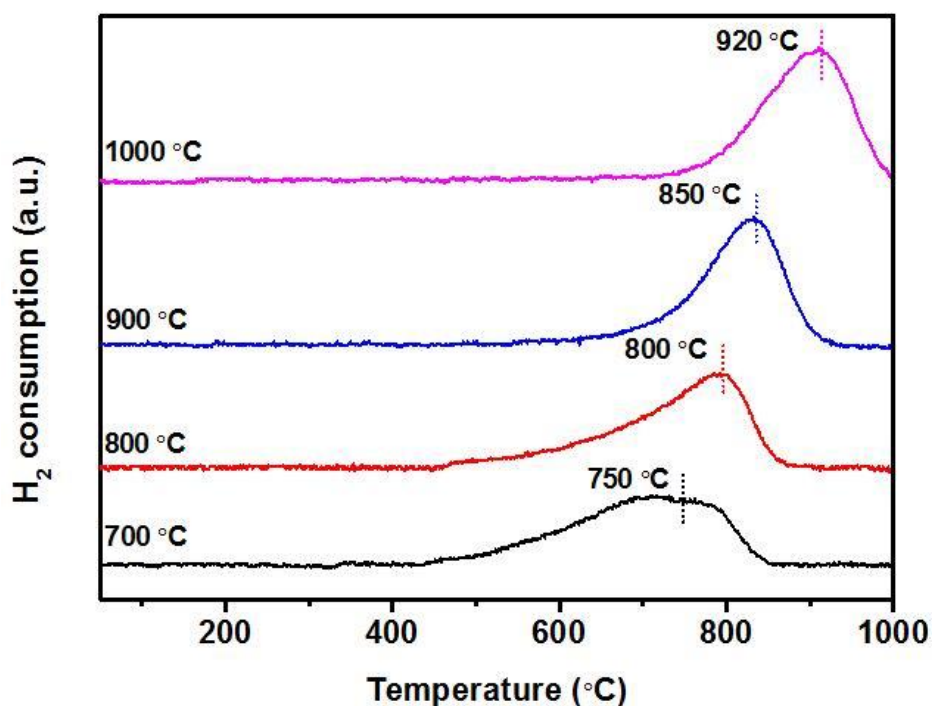


Figure 6-2. TPR profiles of the catalysts calcined at different calcination temperatures.

The H₂ uptake indicates the amount of accessible Ni for reduction, and there is no H₂ uptake decrease according to the peak areas in the TPR profiles, which are 2212, 2341, 2422 and 2536 for the catalysts calcined at 700, 800, 900 and 1000 °C, respectively. It confirms that there is no catalyst aggregation that makes catalyst inaccessible for the reduction as calcination temperature increased owing to the thermally stable structure.

6.3.3 Catalyst microstructure

The fibrous structure of the NiAl₂O₄/Al₂O₃ catalyst calcined at 900 °C is shown in Figure 6-3, and the diameters of the ceramic fibers are less than 150 nm. The fibrous structure possesses high void volume, and fast mass transfer can be achieved over the catalyst surface [18]. Nanofiber support provides a large surface to support nanocatalysts. As shown in Figure 6-4a-4d, the diameter of the reduced Ni/Al₂O₃ catalyst fiber decreased as the calcination temperature increased due to the crystallization of the crystals while the fibrous structure was retained.

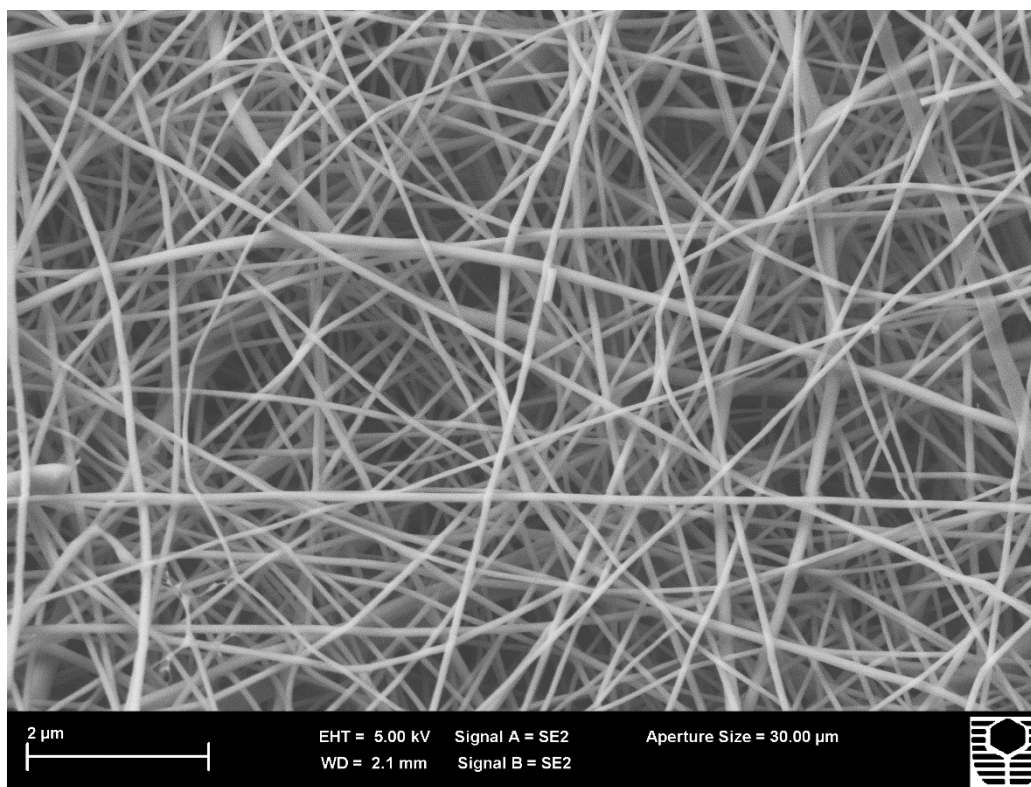


Figure 6-3. A SEM image of the $\text{NiAl}_2\text{O}_4/\text{Al}_2\text{O}_3$ ceramic fibres calcined at $900\text{ }^\circ\text{C}$. The scale bar is $2\text{ }\mu\text{m}$.

After the reduction of the $\text{NiAl}_2\text{O}_4/\text{Al}_2\text{O}_3$ ceramics at $750\text{ }^\circ\text{C}$, nanoparticles appeared on the surface of Al_2O_3 fibers, which should be Ni particles according to our previous study [14]. The Ni particle size increased with the calcination temperature up to about 30 nm at the calcination temperature of $1000\text{ }^\circ\text{C}$. The increase of Ni particle size is attributed to the increased NiAl_2O_4 crystal size. During the reduction of NiAl_2O_4 , Ni particles precipitated on the surface after Ni atoms move through spinel crystals. As the spinel crystal becomes bigger at a higher calcination temperature, more Ni atoms within the big crystals are available to accumulate at Ni nucleation points on the surface, forming Ni agglomerates.

According to TPR results, the catalyst calcined at a higher temperature showed a reduction peak at a higher temperature. Consequently, reduction temperature will affect catalyst properties, which has not been reported in the literature. The catalysts were reduced at 850 and $920\text{ }^\circ\text{C}$, respectively.

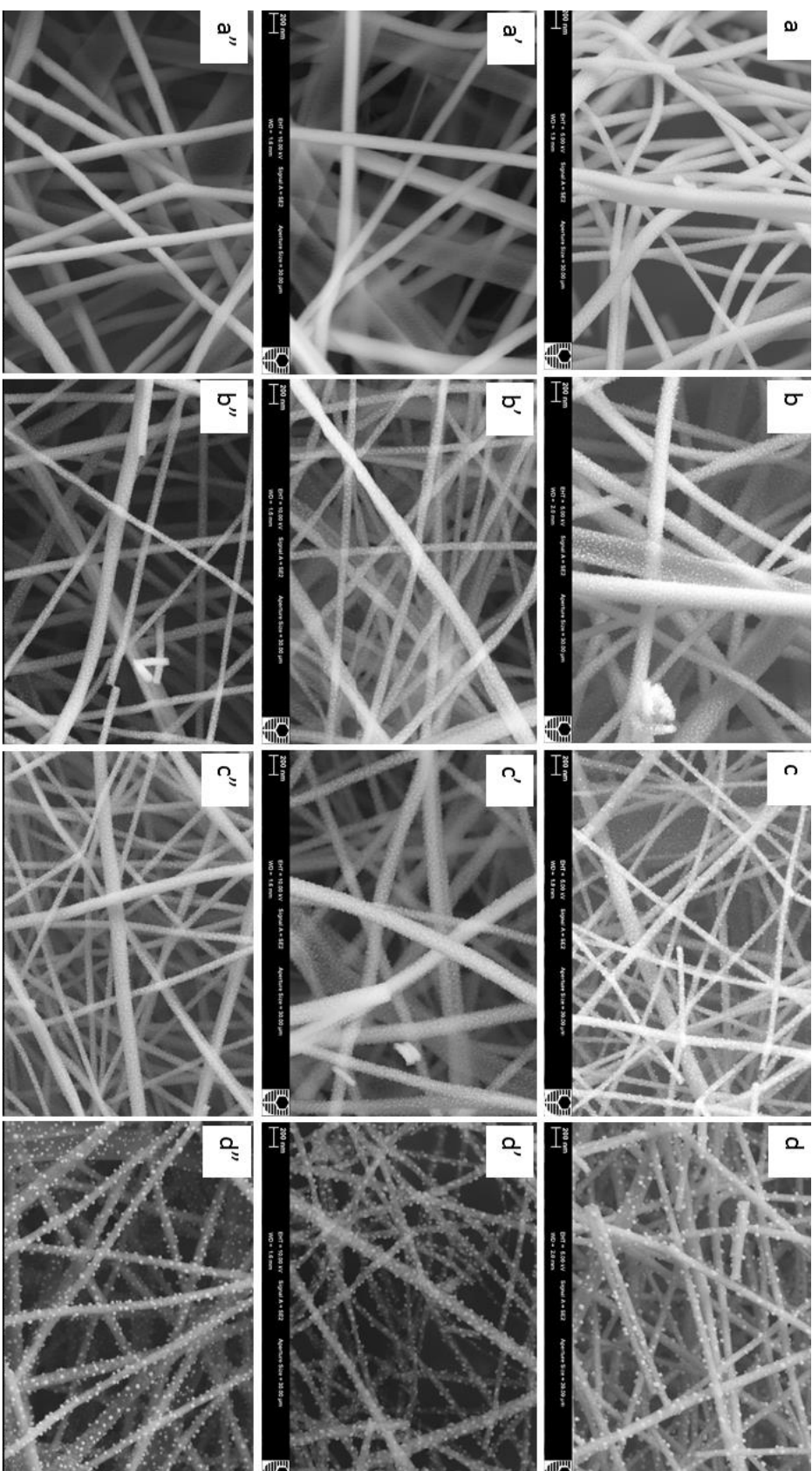


Figure 6-4. SEM images of the catalysts at different calcination/reduction temperatures: a, 700 °C/750 °C; b, 800 °C/750 °C; c, 900 °C/750 °C; d, 1000 °C/750 °C; a', 700 °C/850 °C; b', 800 °C/850 °C; c', 900 °C/850 °C; d', 1000 °C/850 °C; a'', 700 °C/920 °C; b'', 800 °C/920 °C; c'', 900 °C/920 °C; d'', 1000 °C/920 °C. Scale bars are 200 nm.

The SEM images of the reduced catalysts are shown in Figure 6-4a'-d' and Figure 6-4a''-d'', respectively. It is interesting that the high reduction temperatures did not increase Ni particle size while Ni particles became smaller and more compared with that of the catalysts reduced at 750 °C. It has been reported that Ni nucleation is important for Ni reduction from NiAl₂O₄ ceramic [10]. High reduction temperatures thermodynamically promoted Ni nucleation on the NiAl₂O₄ surface, producing more Ni nucleuses to initiate Ni precipitation from ceramic bulk and therefore small and more Ni particles. Accordingly, high reduction temperature increased Ni dispersion via promoting Ni nucleation. Furthermore, there was no Ni aggregation due to Ni particle sintering at high reduction temperatures, even the catalyst calcined at 900 °C and reduced 920 °C in Figure 6-4c''. It confirms the high dispersion of Ni catalyst from the reduction of NiAl₂O₄ and ensures the high thermal stability of the Ni nanocatalyst at high reaction temperatures [15].

6.3.4 Catalytic performances

To investigate the effect of calcination temperature on catalyst reactivity, the dry reforming of methane over the catalysts was tested at 500 °C. According to the TPR profiles, the catalysts calcined at 700, 800, 900 and 1000 °C were reduced at the reduction peak temperatures of 750, 800, 850 and 920 °C, respectively. The reaction rates of CH₄ conversion over the catalysts are shown in Figure 6-5. As gas flow rate increased, the reaction rates became stable, indicating that the reactions were controlled by catalyst surface reaction. The catalyst calcined at a higher temperature showed a lower reactivity owing to a lower catalyst dispersion. To confirm the effect of reduction temperature, the catalyst calcined at 1000 °C was also reduced at 750 °C for the dry reforming, and it exhibited a much lower reactivity compared to the catalyst reduced at a higher temperature of 920 °C. It is due to the low catalyst dispersion and the less amount of catalyst reduced from NiAl₂O₄ according to SEM images. Figure 6-6 shows SEM images of the catalyst calcined at 1000 °C and reduced at 920 °C before and after the reaction. During the reaction, the fibrous structure of the catalyst was retained, and there is no Ni particle aggregation although the morphology of Ni particles was changed during the redox process.

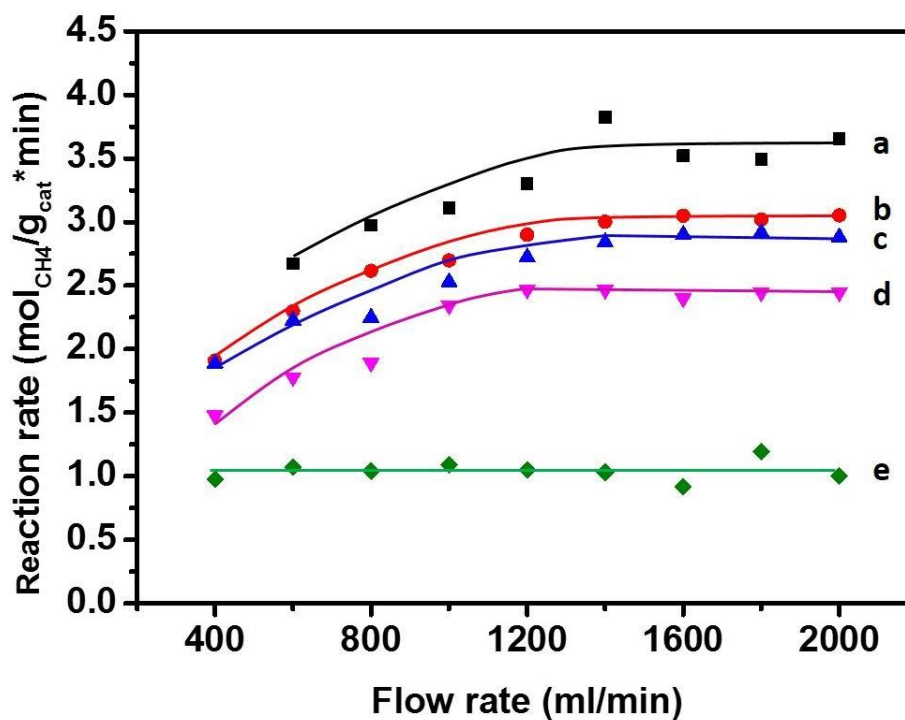


Figure 6-5. Catalytic performances of the dry reforming of methane at 500 °C over the catalysts at different calcination temperature/reduction temperatures: a, 700 °C/750 °C; b, 800 °C/800 °C; c, 900 °C/850 °C; d, 1000 °C/920 °C; e, 1000 °C/750 °C.

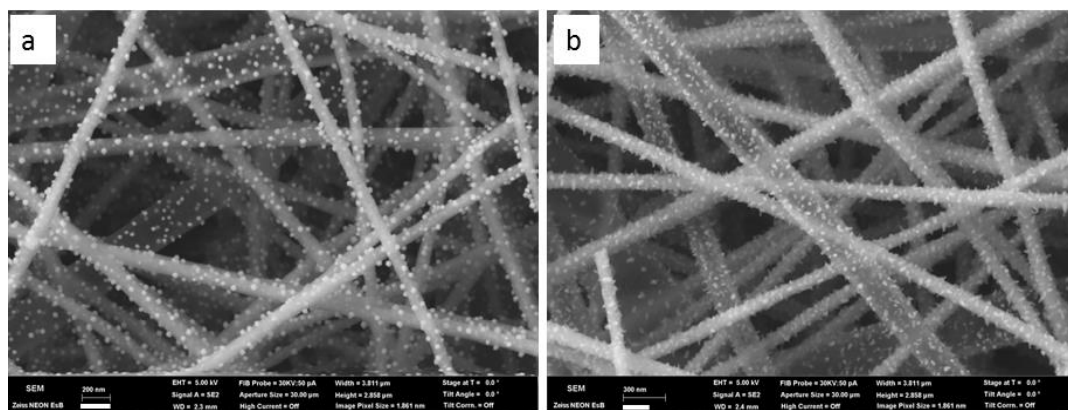


Figure 6-6. SEM images of the catalyst calcined at 1000 °C and reduced at 920 °C before (a) and after (b) reaction.

6.4 Conclusions

Fibrous Ni/Al₂O₃ catalysts show high structural stability because the fibrous structure has a higher resistance to sintering compared with conventional supported catalysts. A higher calcination temperature produces a larger Ni catalyst particle due to the large NiAl₂O₄ crystal, which requires a higher reduction temperature. As a result, the catalyst reactivity in the dry reforming of methane decreased with calcination temperature. High reduction temperatures increased Ni catalyst dispersion via promoting Ni nucleation, while the high temperatures did not cause Ni particle sintering, which confirm the high dispersion of Ni particles reduced from NiAl₂O₄. The reduction temperature effect was confirmed by the reactivity during the dry reforming of methane.

6.5 References

- [1] J.G. Seo, M.H. Youn, J.S. Chung, I.K. Song, Effect of calcination temperature of mesoporous nickel-alumina catalysts on their catalytic performance in hydrogen production by steam reforming of liquefied natural gas (LNG), *Journal of Industrial and Engineering Chemistry*, 16 (2010) 795-799.
- [2] B.S. Liu, C.T. Au, Carbon deposition and catalyst stability over $\text{La}_2\text{NiO}_4/\gamma\text{-Al}_2\text{O}_3$ during CO_2 reforming of methane to syngas, *Applied Catalysis a-General*, 244 (2003) 181-195.
- [3] Z. Wang, X. Shao, A. Larcher, K. Xie, D. Dong, C.-Z. Li, A study on carbon formation over fibrous NiO/CeO_2 nanocatalysts during dry reforming of methane, *Catal. Today*, 216 (2013) 44-49.
- [4] J. Feng, Y. Ding, Y. Guo, X. Li, W. Li, Calcination temperature effect on the adsorption and hydrogenated dissociation of CO_2 over the NiO/MgO catalyst, *Fuel*, 109 (2013) 110-115.
- [5] H. Ozdemir, M.A.F. Oksuzomer, M.A. Gurkaynak, Effect of the calcination temperature on $\text{Ni/MgAl}_2\text{O}_4$ catalyst structure and catalytic properties for partial oxidation of methane, *Fuel*, 116 (2014) 63-70.
- [6] W. Kobsiriphat, B.D. Madsen, Y. Wang, M. Shah, L.D. Marks, S.A. Barnett, Nickel- and Ruthenium-Doped Lanthanum Chromite Anodes: Effects of Nanoscale Metal Precipitation on Solid Oxide Fuel Cell Performance, *J. Electrochem. Soc.*, 157 (2010) B279-B284.
- [7] R. Lopez-Fonseca, C. Jimenez-Gonzalez, B. de Rivas, J.I. Gutierrez-Ortiz, Partial oxidation of methane to syngas on bulk NiAl_2O_4 catalyst. Comparison with alumina supported nickel, platinum and rhodium catalysts, *Applied Catalysis a-General*, 437 (2012) 53-62.

- [8] N. Salhi, A. Boulahouache, C. Petit, A. Kiennemann, C. Rabia, Steam reforming of methane to syngas over NiAl₂O₄ spinel catalysts, *Int. J. Hydrog. Energy*, 36 (2011) 11433-11439.
- [9] T. Jardiel, M.T. Caldes, F. Moser, J. Hamon, G. Gauthier, O. Joubert, New SOFC electrode materials: The Ni-substituted LSCM-based compounds (La_{0.75}Sr_{0.25})(Cr_{0.5}Mn_{0.5-x}Ni_{1-x})O_{3-δ} and (La_{0.75}Sr_{0.25})(Cr_{0.5-x}Ni_xMn_{0.5})O_{3-δ}, *Solid State Ionics*, 181 (2010) 894-901.
- [10] C.P. Li, Y.W. Chen, Temperature-programmed-reduction studies of nickel oxide alumina catalysts-effects of the preparation method, *Thermochimica Acta*, 256 (1995) 457-465.
- [11] A.S.A. Al-Fatish, A.A. Ibrahim, A.H. Fakeeha, M.A. Soliman, M.R.H. Siddiqui, A.E. Abasaheed, Coke formation during CO₂ reforming of CH₄ over alumina-supported nickel catalysts, *Applied Catalysis a-General*, 364 (2009) 150-155.
- [12] Z. Boukha, C. Jimenez-Gonzalez, B. de Rivas, J. Ramon Gonzalez-Velasco, J. Ignacio Gutierrez-Ortiz, R. Lopez-Fonseca, Synthesis, characterisation and performance evaluation of spinel-derived Ni/Al₂O₃ catalysts for various methane reforming reactions, *Appl. Catal. B-Environ.*, 158 (2014) 190-201.
- [13] N. Rahemi, M. Haghghi, A.A. Babaluo, M.F. Jafari, S. Allahyari, The effect of the calcination temperature on the physicochemical properties and catalytic activity in the dry reforming of methane over a Ni-Co/Al₂O₃-ZrO₂ nanocatalyst prepared by a hybrid impregnation-plasma method, *Catalysis Science & Technology*, 3 (2013) 3183-3191.
- [14] Z. Wang, X. Shao, Y. Chen, K. Xie, X. Hu, D. Dong, G. Parkinson, C.-Z. Li, Nanofibrous Ni/Al₂O₃ catalysts for high yield of syngas production *J. Mater. Chem. A*, under review (2015).
- [15] C. Jimenez-Gonzalez, Z. Boukha, B. de Rivas, J. Jose Delgado, M. Angel Cauqui, J. Ramon Gonzalez-Velasco, J. Ignacio Gutierrez-Ortiz, R. Lopez-

Fonseca, Structural characterisation of Ni/alumina reforming catalysts activated at high temperatures, *Applied Catalysis a-General*, 466 (2013) 9-20.

[16] J. Zielinski, Morphology of nickel alumina catalysts, *Journal of Catalysis*, 76 (1982) 157-163.

[17] J. Chen, Y. Qiao, Y. Li, Promoting effects of doping ZnO into coprecipitated Ni-Al₂O₃ catalyst on methane decomposition to hydrogen and carbon nanofibers, *Applied Catalysis a-General*, 337 (2008) 148-154.

[18] E. Reichelt, M.P. Heddrich, M. Jahn, A. Michaelis, Fiber based structured materials for catalytic applications, *Applied Catalysis a-General*, 476 (2014) 78-90.

Every reasonable effort has been made to acknowledge the owners of the copyright materials. I would be pleased to hear from any copyright owner who has been omitted or incorrectly acknowledged.

Chapter 7

Conclusions and recommendations

7.1 Conclusions

The purpose of this study was to investigate the merits of fibrous catalysts during the catalytic methane reforming. The fibrous catalysts were prepared by templating synthesis and electrospinning process, respectively. The preparation parameters that affect the catalyst structure were studied. The catalysts properties were characterized before and after catalytic methane reforming. The effects of catalysts properties on the catalytic performance during different reforming reactions were investigated. Several advantages of the newly developed fibrous catalysts in methane reforming have been demonstrated.

The fast mass transfer can be achieved over the fibrous catalysts. Like metal gauze/mesh/foam catalysts, fibrous catalysts provide fast mass transfer paths from bulk gas flow to catalyst sites. Compared with powder supported catalysts, fibrous structure diminishes or even eliminates the internal gas diffusion in the traditional porous supports. As a result, low pressure drops through the catalyst bed packed with the catalyst flakes enable the operation at high gas flow rates, which can be normally achieved partially by pelletizing powder catalysts with greatly increased internal gas diffusion resistance. The highest syngas yield by the 24.1 wt% Ni/Al₂O₃ fibrous catalyst has been achieved at the highest-recorded gas hour space velocity of $8 \times 10^6 \text{ L Kg}^{-1} \text{ h}^{-1}$ in the partial oxidation of methane. In addition, the fast mass transfer reduced carbon formation during the dry reforming of methane by quickly desorbing radicals from catalyst surface where high gas flow rates were used.

The second advantage of the fibrous catalysts is high catalytic activity, which is achieved by the high dispersion of catalysts at high contents/loadings. Like powder-supported catalysts, high catalyst contents/loadings can be readily achieved by the one-step preparation processes. Moreover, high catalyst dispersions were maintained at high catalyst contents. In the templating synthesis, a hierarchical structure of catalysts was formed. For individual fibers, Ni nanoparticles were supported on CeO₂ scaffold, which enables small Ni particle sizes even at the NiO content of 47.8 wt%. Ni/Al₂O₃ fibrous catalysts were prepared by electrospinning, where Ni particles were formed by reducing NiAl₂O₄, which improved Ni dispersion. Furthermore, the nanosized fibre support provide a large surface to support the Ni nanoparticles.

Another advantage of the fibrous catalyst is high thermal stability. Compared with powder catalysts, the fibrous catalysts demonstrated high resistance to sintering owing to one dimensional structure. The fibrous structure can be retained at calcination temperatures up to 1000 °C, which is higher than methane reforming temperatures. Hence, there is no further catalyst sintering in the reactions, which would otherwise cause catalyst degradation. Moreover, the high calcination temperature increased the interaction between catalyst and support, which improved coking-resistance and catalytic activity during the dry and steam reforming of methane.

For the preparation of catalysts, technically speaking, the templating synthesis using eggshell membrane as the template, which is currently a kind of home waste, is economically advantageous and green. However, the property of templated catalysts, in terms of fibre diameter, is restrained by the organic fibre of eggshell membrane itself. In addition, as the synthesis process involves the free adsorption of metal ions onto the organic fibre surface as well as the competition between different metal ions (Ni^{2+} and Ce^{4+}), the control of catalysts loading and reproducibility might be problematic in theory. Electrospinning is a promising technology in fabricating hierarchically structured materials with the diameters of each fibre down to 20 nm. The properties of these electrospun catalysts are effected by groups of easily controlled parameters, such as solution properties (e.g. viscosity), electric field force and humidity. Electrospinning could fabricate fibrous catalysts with optimized fibre diameter and catalyst loading, compared with the eggshell membrane templated catalyst. Overall, electrospinning is better in catalyst preparation and property control, and therefore have better performance in methane reforming, compared with the template synthesis. Although electrospinning might be problematic in fabricating fibrous catalysts to certain thickness (above 20 micrometres after heat treatment), it has the potential to be scaled up for applications requiring catalysts of large surface area.

In summary, the fibrous catalysts are a good candidate for the catalytic methane reforming, as it combines the advantages of the non-porous metal catalysts (fast mass transfer) and the traditional porous catalysts (high catalytic activity). High stability of the fibrous catalysts is attributed to its thermally stable structure. These advantages

indicate that the fibrous catalysts are of great potential for the industrial applications in methane reforming as well as other catalytic reactions.

7.2 Recommendations

Several parameters in catalyst preparation and reaction operation were studied, and some conclusions have been drawn above. Being a new type of catalysts, nevertheless, more work need to be done not only to further optimise catalyst structure for achieving high catalytic performance, but also for acquiring a better fundamental understanding of the fibrous catalysts.

1. The performance of catalysts is largely determined by the preparative methods. This study mainly studied the effects of catalyst content and calcination temperature on the catalytic performance of the fibrous catalysts. Other parameters that could affect the performance of the fibrous catalysts via affecting the mass transfer over catalyst surface such as the dimension of fibres and thickness of the catalysts flakes are also worth studying to achieve high catalytic performance in methane reforming. Another importance parameter affecting the performance of the catalysts is the materials/composition. A detailed screening of materials and composition such as the application of noble metal catalysts in perovskite structure is valuable to expand the application of the fibrous catalyst for the reactions that require fast mass transfer and well-dispersed catalyst particles.
2. As a new type of catalyst that combines the advantages of metal gauze catalysts and porous supported catalysts, better fundamental understanding of the fibrous catalyst is required to promote its applications. The mass transfer in traditional catalysts and gauze catalysts has been well studied and the effects of mass transfer on the selectivity of the desired products were investigated as well. To promote the application of fibrous catalysts, several aspects should be investigated, examples include: how does mass transfer occur around and in the fibrous catalysts and what are the effects of mass transfer on syngas selectivity. Furthermore, the fibrous catalyst shows high performance in methane reforming with high throughput without substantial

pressure drop. It is also worth trying by combining the fibrous catalysts with the current industrial catalysts to achieve high throughput and longevity.

Appendix I

**Permission of Reproduction from the
Copyright Owner**

RightsLink



Thank You For Your Order!

Dear Mr. zhitao wang,

Thank you for placing your order through Copyright Clearance Center's RightsLink service. Elsevier has partnered with RightsLink to license its content. This notice is a confirmation that your order was successful.

Your order details and publisher terms and conditions are available by clicking the link below:

<http://s100.copyright.com/CustomerAdmin/PLF.jsp?ref=3dfbe97d-622f-46b4-9529-5fd080edef1a>

Order Details

Licensee: zhitao wang

License Date: May 17, 2015

License Number: 3631420393869

Publication: Fuel Processing Technology

Title: Oxidative processes in natural gas conversion

Type Of Use: reuse in a thesis/dissertation

Total: 0.00 USD

To access your account, please visit <https://myaccount.copyright.com>.

Please note: Online payments are charged immediately after order confirmation; invoices are issued daily and are payable immediately upon receipt.

To ensure that we are continuously improving our services, please take a moment to complete our [customer satisfaction survey](#).

B.1:v4.2

+1-855-239-3415 / Tel: +1-978-646-2777
customercare@copyright.com
<http://www.copyright.com>



Thank You For Your Order!

Dear Mr. zhitao wang,

Thank you for placing your order through Copyright Clearance Center's RightsLink service. John Wiley and Sons has partnered with RightsLink to license its content. This notice is a confirmation that your order was successful.

Your order details and publisher terms and conditions are available by clicking the link below:

<http://s100.copyright.com/CustomerAdmin/PLF.jsp?ref=181f5120-b50f-4473-9ac3-e45e1bd08e59>

Order Details

Licensee: zhitao wang

License Date: May 17, 2015

License Number: 3631241285700

Publication: Advanced Materials

Title: Electrospinning of Nanofibers: Reinventing the Wheel?

Type Of Use: Dissertation/Thesis

Total: 0.00 USD

To access your account, please visit <https://myaccount.copyright.com>.

Please note: Online payments are charged immediately after order confirmation; invoices are issued daily and are payable immediately upon receipt.

To ensure that we are continuously improving our services, please take a moment to complete our [customer satisfaction survey](#).

B.1:v4.2

+1-855-239-3415 / Tel: +1-978-646-2777

customercare@copyright.com

<http://www.copyright.com>



Thank You For Your Order!

Dear Mr. zhitao wang,

Thank you for placing your order through Copyright Clearance Center's RightsLink service. Elsevier has partnered with RightsLink to license its content. This notice is a confirmation that your order was successful.

Your order details and publisher terms and conditions are available by clicking the link below:

<http://s100.copyright.com/CustomerAdmin/PLF.jsp?ref=84904290-331f-44a4-8b8a-7dc7a47b6c24>

Order Details

Licensee: zhitao wang

License Date: May 25, 2015

License Number: 3636260886338

Publication: Catalysis Today

Title: A study on carbon formation over fibrous NiO/CeO₂ nanocatalysts during dry reforming of methane

Type Of Use: reuse in a thesis/dissertation

Total: 0.00 USD

To access your account, please visit <https://myaccount.copyright.com>.

Please note: Online payments are charged immediately after order confirmation; invoices are issued daily and are payable immediately upon receipt.

To ensure that we are continuously improving our services, please take a moment to complete our [customer satisfaction survey](#).

B.1:v4.2

+1-855-239-3415 / Tel: +1-978-646-2777

customercare@copyright.com

<http://www.copyright.com>



Thank You For Your Order!

Dear Mr. zhitao wang,

Thank you for placing your order through Copyright Clearance Center's RightsLink service. Elsevier has partnered with RightsLink to license its content. This notice is a confirmation that your order was successful.

Your order details and publisher terms and conditions are available by clicking the link below:

<http://s100.copyright.com/CustomerAdmin/PLF.jsp?ref=fa003ba5-ac5d-4cab-a9e0-999557a34a5d>

Order Details

Licensee: zhitao wang

License Date: May 25, 2015

License Number: 3636280164150

Publication: Catalysis Today

Title: Hierarchically structured NiO/CeO₂ nanocatalysts templated by eggshell membranes for methane steam reforming

Type Of Use: reuse in a thesis/dissertation

Total: 0.00 USD

To access your account, please visit <https://myaccount.copyright.com>.

Please note: Online payments are charged immediately after order confirmation; invoices are issued daily and are payable immediately upon receipt.

To ensure that we are continuously improving our services, please take a moment to complete our [customer satisfaction survey](#).

B.1:v4.2

+1-855-239-3415 / Tel: +1-978-646-2777
customercare@copyright.com
<http://www.copyright.com>

